BIPED LOCOMOTION: STABILITY ANALYSIS, GAIT GENERATION AND CONTROL

By

Dip Goswami

SUBMITTED IN PARTIAL FULFILLMENT OF THE
REQUIREMENTS FOR THE DEGREE OF
DOCTOR OF PHILOSOPHY
AT
DEPARTMENT OF ELECTRICAL AND COMPUTER ENGINEERING,
NATIONAL UNIVERSITY OF SINGAPORE
4 ENGINEERING DRIVE 3, SINGAPORE 117576
AUGUST 2009

Table of Contents

Table of Contents ii

List of Tables vi

List of Figures vii

Acknowledgements xii

Abstract xiii

1 Introduction 1
- 1.1 The Biped Locomotion . . . 2
- 1.2 Postural Stability . . . 8
  - 1.2.1 Zero-Moment-Point . . . 9
  - 1.2.2 Foot-Rotation-Indicator Point . . . 13
  - 1.2.3 Biped Model With Point-Foot . . . 15
- 1.3 Actuator-level Control . . . 16
  - 1.3.1 Internal dynamics and Zero-dynamics . . . 20
- 1.4 Gait Generation . . . 21
- 1.5 Dissertation Outline . . . 23

2 Biped Walking Gait Optimization considering Tradeoff between Stability Margin and Speed 26
- 2.1 Biped Model, Actuators and Mechanical Design . . . 28
- 2.2 Biped Inverse Kinematics . . . 30
  - 2.2.1 Generalized Coordinates . . . 30
  - 2.2.2 Inverse Kinematics . . . 31
- 2.3 Biped Walking Gait . . . 35
  - 2.3.1 Choice of Walking Parameters . . . 38

2.4 Genetic Algorithm . . . 39
2.5 GA Based Parameter Optimization . . . 40
2.5.1 Constrains on Walking Parameters . . . 40
2.5.2 Postural Stability Considering ZMP . . . 40
2.5.3 Cost Function . . . 42
2.6 Computation of ZMP . . . 44
2.6.1 ZMP Expression . . . 46
2.7 Simulations and Experiments . . . 48
2.7.1 Effect of λ on walking performance . . . 51
2.7.2 Effect of step-time (T) on walking performance . . . 58
2.8 Conclusions . . . 59

3 Disturbance Rejection by Online ZMP Compensation 60
3.1 ZMP Measurement . . . 62
3.1.1 Biped Model . . . 62
3.1.2 Force Sensors . . . 63
3.1.3 Measurement of ZMP . . . 64
3.2 Online ZMP Compensation . . . 69
3.3 Applications, Experiments and Results . . . 74
3.3.1 Improvement of Walking on Flat Surface . . . 75
3.3.2 Rejecting Disturbance due to Sudden Push . . . 75
3.3.3 Walking Up and Down a Slope . . . 77
3.3.4 Carrying Weight during Walking . . . 78
3.4 Conclusions . . . 80

4 Jumping Gaits of Planar Bipedal Robot with Stable Landing 85
4.1 The Biped Jumper . . . 88
4.1.1 Biped Jumper: BRAIL 2.0 . . . 88
4.1.2 Foot Compliance Model and Foot Design . . . 92
4.1.3 Jumping Sequences . . . 93
4.1.4 The Lagrangian Dynamics of the Biped in Take-off and Touch-down Phases . . . 96
4.1.5 Lagrangian Dynamics Computation of the at the Take-off and Touch-down phases . . . 98
4.1.6 The Lagrangian Dynamics of the Biped in Flight Phase . . . 101
4.1.7 Impact Model and Angular Momentums . . . 103
4.1.8 Jumping Motion and Angular Momentum relations . . . 104
4.2 Control Law Development . . . 106
4.3 Selection of Desired Gait . . . 106

4.3.1 Take-off phase Gait . . . 109
4.3.2 Flight phase Gait . . . 109
4.3.3 Touch-down phase Gait . . . 111
4.4 Landing Stability Analysis . . . 111
4.4.1 Switched Zero-Dynamics (SZD): Touch-down phase . . . 112
4.4.2 Stability of SZD . . . 115
4.4.3 Closed-loop Dynamics: Touch-down phase . . . 121
4.5 Simulations and Experiments . . . 129
4.5.1 Jumping Gait Simulations . . . 129
4.5.2 Jumping Experiment on BRAIL 2.0 . . . 134
4.5.3 Comments on Simulations and Experimental Results . . . 141
4.6 Conclusions . . . 142
4.6.1 Future Directions . . . 143

5 Rotational Stability Index (RSI) Point: Postural Stability in Bipeds 144
5.1 Planar Biped: Two-link model . . . 147
5.1.1 Dynamics . . . 149
5.1.2 Internal Dynamics . . . 150
5.1.3 Postural Stability . . . 150
5.2 Rotational Stability and Rotational Stability Index (RSI) Point . . . 154
5.2.1 Planar Bipeds and Rotational Stability . . . 155
5.2.2 CM criteria for Rotational Stability . . . 159
5.2.3 Discussions on the RSI Point . . . 161
5.3 RSI Point Based Stability Criteria . . . 163
5.3.1 Gaits with $\dot{\theta}_2 \neq 0$ . . . 164
5.3.2 Backward foot-rotation . . . 164
5.3.3 Stability Criterion . . . 166
5.3.4 Comparison with other Ground Reference Points . . . 166
5.4 Simulations and Experiments . . . 168
5.4.1 Simulations . . . 170
5.4.2 Experiments . . . 177
5.5 Conclusions . . . 179

6 Conclusions and Future Directions 180
6.1 Conclusions . . . 180
6.2 Future Directions . . . 182

7 Author's Publications **184**
7.1 International Journal 184
7.2 International Conference 185

Bibliography **186**

List of Tables

2.1 Parameters of the BRAIL 1.0. 29
2.2 Parameters of GA. 39
2.3 Optimum Walking Parameters obtained through GA optimization. . . 49
2.4 Walking Parameters for different step-time (T) with $\lambda = 0.1$. 59
2.5 Walking Parameters for different step-time (T) with $\lambda = 0.15$. 59

3.1 Parameters of the Biped-Model (MaNUS-I) 64

4.1 Parameters of the BRAIL 2.0 biped 90
4.2 DH Parameters of the Robot 99
4.3 Robot's Jumping Gait 130
4.4 Different Parameters Values at Jumping Phases. 131
4.5 V_{xcm}^{max} and V_{ID}^{max}. 133

List of Figures

1.1 Sagittal, Frontal and Transverse planes. 3
1.2 Planar Robot. 3
1.3 Single-support and double-support phases. 4
1.4 Biped Locomotion. 4
1.5 Support Polygon. 8
1.6 Zero-Moment-Point. M: Total Mass of the system, $\vec{a}$ is the linear acceleration, $\vec{F}_{GRF}$ is the ground-reaction force, ZMP (x_{zmp}, y_{zmp}) is where $\vec{F}_{GRF}$ acts. 10
1.7 Inverted Pendulum Model. 12
1.8 FRI Point. M: Total mass, M_{foot}: Foot mass, a_{foot}: Foot acceleration, τ_{ankle}: Torque input at the ankle joint, CM_{foot} : CM of the foot. . . . 14
1.9 Periodic Motion. 16

2.1 Generalized Coordinates. 30
2.2 Biped model: Mass Distribution. 31
2.3 The Biped. 32
2.4 Biped Reference Points for Inverse Kinematics. 33
2.5 Biped: Inverse Kinematic Parameters. 33
2.6 Gait Generation Parameters. 36
2.7 The GA algorithm for obtaining optimal walking parameters for a specific value of λ. 41
2.8 Fitness trend with $\lambda = 0.15$. 50

2.9 The walking gait with $\lambda = 0.15 : \theta_1, \theta_{12}, \theta_2, \theta_{11}, \theta_3, \theta_{10}$ (time in Second vs. angle in degree). 52
2.10 The walking gait with $\lambda = 0.15 : \theta_4, \theta_9, \theta_5, \theta_8, \theta_6, \theta_7$ (time in Second vs. angle in degree). 53
2.11 Biped walking for one step-time with $\lambda = 0.15$. 54
2.12 y_{zmp} vs. x_{zmp} for one step-time with $\lambda = 0.15, s = 0.13, n = 0.109, H = 0.014, h = 0.020$. 55
2.13 y_{zmp} and x_{zmp} vs. time for one step-time with $\lambda = 0.15, s = 0.13, n = 0.109, H = 0.014, h = 0.020$ (dotted line is x_{zmp} and solid line is y_{zmp}). 55
2.14 y_{zmp} vs. x_{zmp} for one step-time with $\lambda = 1.0, s = 0.055, n = 0.12, H = 0.026, h = 0.010$. 56
2.15 y_{zmp} and x_{zmp} vs. time for one step-time with $\lambda = 1.0, s = 0.055, n = 0.12, H = 0.026, h = 0.010$ (dotted line is x_{zmp} and solid line is y_{zmp}). 56
2.16 y_{zmp} vs. x_{zmp} for one step-time with $\lambda = 1.0, s = 0.125, n = 0.128, H = 0.01, h = 0.022$. 57
2.17 y_{zmp} and x_{zmp} vs. time for one step-time with $\lambda = 1.0, s = 0.125, n = 0.128, H = 0.01, h = 0.022$ (dotted line is x_{zmp} and solid line is y_{zmp}). 57

3.1 Biped Model in the frontal and sagittal plane. 63
3.2 Biped Model of MaNUS-I in visualNastran 4D environment. 65
3.3 MaNUS-I. 66
3.4 Mechanical Installation of Force Sensors. 67
3.5 Force-to-Voltage Converter Circuit. 67
3.6 Positions of the foot sensors at the bottom of the feet. 67
3.7 Reading of the Force Sensors. 67
3.8 Simplified model of the Biped in Sagittal and Frontal Planes. 68
3.9 The block diagram for online ZMP compensation. 74
3.10 Normalized x-ZMP Position of Uncompensated Walking Gait. 76
3.11 Normalized x-ZMP Position of Compensated Walking Gait. 77
3.12 Compensation at the ankle-joint during walking on a flat surface. . . 78

3.13 Measurement of Disturbance Force. 79
3.14 Oscilloscope display of the applied force. 80
3.15 Normalized x-ZMP Position of MaNUS-I when it experience a sudden push of intensity around 3 N from behind. 81
3.16 Compensation at the ankle-joint of MaNUS-I to compensate a sudden push of intensity around 3 N from behind. 81
3.17 Robot walking sequence when pushed from behind. 82
3.18 Robot walking sequence when pushed from the front. 82
3.19 Walking up a 10^o slope. 82
3.20 Walking down a 3^o slope. 82
3.21 Manus-I carrying Additional Weight. 83
3.22 Normalized x-ZMP Position of Compensated Walking Gait while carrying 300 gm weight. 84
3.23 Compensation at the ankle-joint while carrying 300 gm weight. 84

4.1 BRAIL 2.0 and Autodesk design 89
4.2 The Biped Model 91
4.3 Foot compliance model. 92
4.4 Foot plate of BRAIL 2.0 93
4.5 Phases of Jumping Motion. 95
4.6 Coordinate System Assignment for Lagrangian formulation. 98
4.7 Two-link equivalent model of the biped with foot. 107
4.8 Flight-phase Gait Design Parameters. 110
4.9 Phase Portrait of SZD (4.54). Trajectory I: Member of the set of trajectories going out with increasing θ_1. Trajectory II: Member of the set of trajectories reaching the $\theta_1 = 0$ plane. 114
4.10 Stability of internal dynamics for $x_{cm}(\theta_{a0}) > 0$. 126
4.11 ζ vs. η. 132
4.12 τ_1 at Touch-down phase. 133
4.13 θ_1 vs. σ (dotted) and κ_3 vs. σ (solid). 134

4.14 Variations of the joint torques in experimental and simulation studies: (a) τ_2, (b) τ_3 and (c) τ_4. 137
4.15 Variations of the joint angular positions in experimental and simulation studies: (a) θ_2, (b) θ_3 and (c) θ_4. 138
4.16 Variations of the joint angular velocities in experimental and simulation studies: (a) $\dot{\theta}_2$, (b) $\dot{\theta}_3$ and (c) $\dot{\theta}_4$. 139
4.17 Jump Sequence with control input (4.43) and desired gait as per Table 4.5.1. 140

5.1 (a) Foot-Rotation in frontal plane (b) Foot-rotation in double-support phase (sagittal plane) (c) Foot-rotation in single-support phase (sagittal plane) (d) Foot-rotation in swinging leg (sagittal plane). 145
5.2 Tiptoe Model. 147
5.3 Tiptoe Configuration: Two-link model. 148
5.4 Phase Portrait of (5.10). Trajectory I: Member of the set of trajectories going out with increasing θ_1. Trajectory II: Member of the set of trajectories reaching the $\theta_1 = 0$ plane. 153
5.5 *Rotational Stability*. 155
5.6 RSI point and Phase Portrait. 161
5.7 *Rotational Stability* for stationary biped. 162
5.8 RSI point $x_{RSI} > 0$. Biped is *rotational stable* even if $x_{cm}(\theta) < 0$. . . 162
5.9 Forward and backward foot-rotation. 165
5.10 ZMP/FRI/CP/FZMP and RSI: (a) Foot is not going to rotate. (b) Foot is about to rotate. (c) Foot is rotated, and bipedal posture is *rotational stable*. 167
5.11 ZMP/FRI/CP and RSI: ZMP/CP/FRI indicate whether the foot is about to rotate or not, RSI point indicates whether the bipedal posture will lead to a flat-foot posture or not. 167
5.12 Parameters of BRAIL 2.0 169
5.13 θ_1 Vs. x_{RSI} θ_1 Vs. x_{cm} and : $\theta_{10} = 0.6$ rad and $\sigma_0 = -0.0289\ kgm^2s^{-1}$. 171

5.14 θ_1 Vs. σ: $\theta_{10} = 0.6$ rad and $\sigma_0 = -0.0289\ kgm^2s^{-1}$. 172
5.15 θ_1 Vs. x_{RSI} and θ_1 Vs. x_{cm}: $\theta_{10} = 0.3$ rad and $\sigma_0 = 0.0542\ kgm^2s^{-1}$. 173
5.16 θ_1 Vs. σ: $\theta_{10} = 0.3$ rad and $\sigma_0 = 0.0542\ kgm^2s^{-1}$. 173
5.17 θ_1 Vs. x_{RSI} and θ_1 Vs. x_{cm}: Pushed from the backside and *rotational stable*. 174
5.18 θ_1 Vs. σ: Pushed from the backside and *rotational stable*. 175
5.19 θ_1 Vs. σ: Pushed from the backside and 'rotational unstable'. 176
5.20 θ_1 Vs. σ: Pushed from the backside and 'rotational unstable'. 176
5.21 BRAIL 2.0: Push from back. 178

Acknowledgements

With immense pleasure I express my sincere gratitude, regards and thanks to my supervisors A/Prof. Prahlad Vadakkepat for his excellent guidance, invaluable suggestions and continuous encouragement at all the stages of my research work. His interest and confidence in me was the reason for all the success I have made. I have been fortunate to have him as my advisor as he has been a great influence on me, both as a person and as a professional.

Many thanks goes to Prof. QG Wong, Prof. Tong Heng Lee, A/Prof. Loh Ai Poh and Dr. Tang for their kind help and suggestions. I would like to express my appreciation to Mr. Burra Pavan Kumar, Mr. Jin Yongying and Mr. Phoon Duc Kien for their support. Moreover, I would like to thank my colleagues Mr. Jim Tan, Mr. Daniel Hong, Mr. Ng Buck Sin and Mr. Pramod Kumar for various constructive discussions and suggestions. Finally, I show my appreciation to the lab officer Mr. Tan Chee Siong for his support and friendly behavior.

I acknowledge the chance provided to me to pursuit doctoral study in National University of Singapore. I express my deepest appreciation to all the member of Electrical And Computer Engineering for the wonderful research environment and immense support. I do love to remember the time I spend with them.

I am deeply indebted to my beloved wife for her support, understanding and encouragement in every aspects of life. Without her, I would not possibly have achieved whatever I have. Finally, I am grateful to my parents for their support.

Abstract

Locomotion is an important domain of research in Bipedal Robots. Dynamics of the foot-link plays a key role in the stability of biped locomotion. Biped locomotion can be either with flat-foot (foot-link does not loose contact with ground surface) or with foot-rotation (foot-link rotates about toe). The initial part of this dissertation presents a flat-foot optimal walking gait generation method. The optimality in gait is achieved by utilizing Genetic Algorithm considering a tradeoff between walking speed and stability. The optimal flat-foot walking gaits are implemented on a biped robot - BRAIL 1.0. The robustness of such gaits in presence of disturbances is enhanced by applying zero-moment-point (ZMP) compensation into the robot's ankle-joint. Effectiveness of the ZMP compensation technique is validated by utilizing the technique to maintain postural stability when a humanoid robot, MaNUS-I, is subjected to disturbances (in the form of push from front or back, carrying weight in the back and climbing up/down slopes). Such flat-foot gaits are suitable when the biped is moving slowly. However, the foot-link can rotate during relatively faster bipedal activities.

The bipeds, with foot-rotation, have an additional passive degree-of-freedom at the joint between toe and ground. Such bipeds are underactuated as they have one degree-of-freedom greater than the number of available actuators during the single-support phase. Underactuated biped dynamics (with foot-rotation) has two-dimensional zero-dynamics submanifold of the full-order bipedal model. Stability of the associated zero-dynamics is essential for the stability of the biped locomotion with foot-rotation. The nature of zero-dynamics is governed by the structure of the biped, foot/ground

contact surface and certain control parameters.

Landing stability of bipedal jumping gaits is studied considering the stability of the associated zero-dynamics. In the landing phase of jumping gaits, switching occurs between configurations with flat-foot and with foot-rotation. The associated bipedal zero-dynamics in jumping gait is modeled as a switching system. Stability of the switching zero-dynamics is investigated by two novel concepts - critical potential index and critical kinetic index. Utilizing the stability concepts, stable landing is achieved while implementing the jumping gait on a biped robot - BRAIL 2.0.

A novel concept of rotational stability is introduced for the stability analysis of biped locomotion with foot-rotation. The rotational stability of underactuated biped is measured by introducing a ground-reference-point Rotational Stability Index (RSI) point. The concepts of rotational stability and Rotational Stability Index point investigates the stability of associated zero-dynamics. A stability criterion, based on Rotational Stability Index point, is established for the stability in biped locomotion with foot-rotation.

Chapter 1

Introduction

Locomotion is the ability of animal life to move from one place to another. The diversity of animal locomotion is astounding and surprisingly complex. The means of biological locomotion depends on the morphology, scale, and environment of the organism. Similar argument is applicable for the man-made machines. Airplanes use wings, army tanks use tracks for traversing uneven terrain and automobiles use wheels. In case of environments with discontinuous ground support such as rocky slope or stairs, it is arguable that the most appropriate and versatile means of locomotion is legs. Legs enable the avoidance of support discontinuities in the environment by stepping over them. Moreover, legs are the obvious choice for locomotion in environments designed for humans.

Robots are machines which perform complicated often repetitive tasks autonomously. Depending on the application, there are various types of robots such as industrial robots, domestic robots or hobbyist's robots. The robots which look like human being are generally referred as humanoid robots. There are several humanoid robots reported in the literature. Waseda University is a leading research group in humanoid

robot since they started the WABOT project in 1970. They have developed a variety of humanoid robots including WABOT-1 (1973), the musician robot WABOT-2 (1984), and a walking biped robot WABIAN (WAseda BIpedal humANoid) (1997) [1]. The biped robot model called HOAP [2] is commercially marketed by Fujitsu. In 2000, Honda released a humanoid robot- ASIMO which has twelve degree-of-freedom (DOF) in two legs and fourteen DOF in each arm.

Humanoid robots use two legs for accomplishing locomotion which is called biped locomotion. The motivation for the research on bipedal locomotion is its much-needed mobility required for maneuvering in environments meant for humans. Wheeled vehicles can only move efficiently on relatively flat terrains whereas a legged robot can make use of suitable footholds to traverse in rugged terrains. Bipedal locomotion is a lesser stable activity than say four-legged locomotion, as multi-legged robots have more footholds for support. Bipedal locomotion allows, instead, greater maneuverability especially in constraint spaces.

1.1 The Biped Locomotion

Robots with two legs are biped robots or bipeds. Bipeds accomplish locomotion by specific motion in various planes: sagittal, frontal and transverse planes (Fig. 1.1). The sagittal plane is the longitudinal plane that divides the body into right and left sections. The frontal plane is the plane parallel to the long axis of the body and perpendicular to the sagittal plane that separates the body into front and back portions. A transverse plane is a plane perpendicular to sagittal and frontal planes which divides the body into top and bottom portions.

Sometimes, the motion is restricted to one plane and such robots are planar robots.

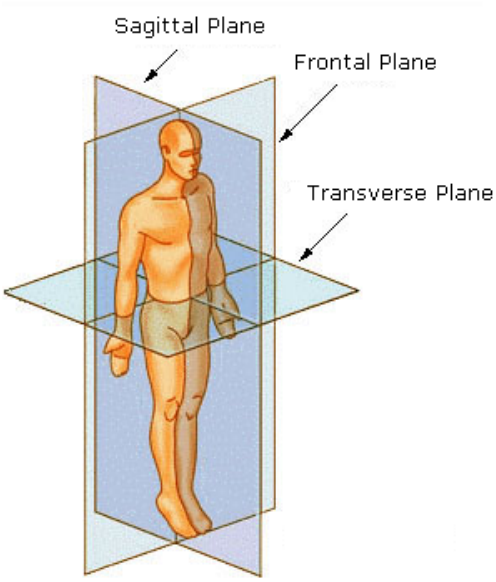

Figure 1.1: Sagittal, Frontal and Transverse planes.

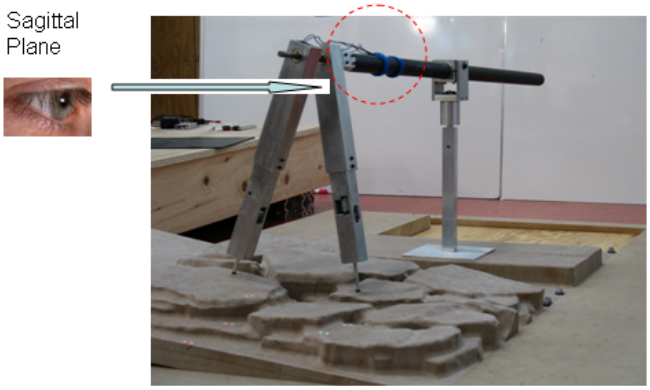

Figure 1.2: Planar Robot.

Figure 1.3: Single-support and double-support phases.

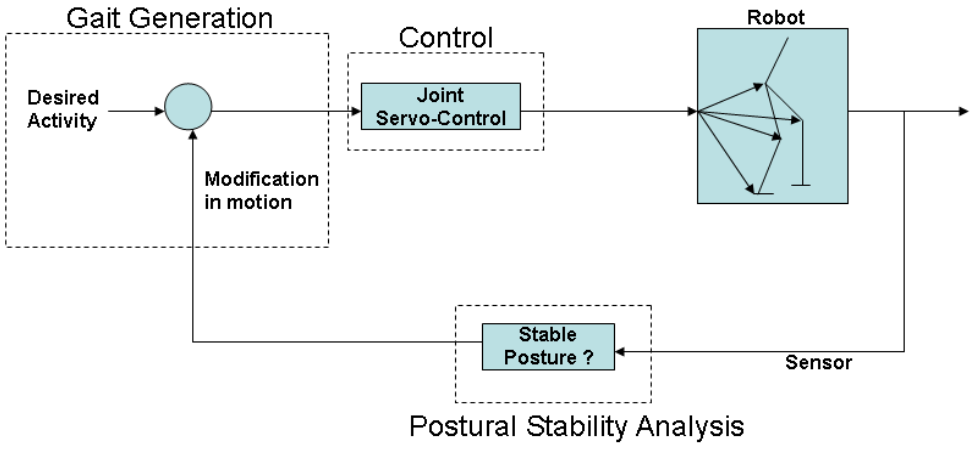

Figure 1.4: Biped Locomotion.

An examples of planar robot is RABBIT (Fig. 1.2) [3]. Typically, motion in a particular plane is realized by a combination of DOFs in that plane. An actuator or a servo motor is used to implement one DOF. Actuators are placed at the joints. During biped locomotion either single or double feet are in contact with the ground. Biped Locomotion with single foot-ground contact is single-support phase while that with double foot-ground contact is double-support phase (Fig. 1.3). When only one leg is in contact with the ground, the contacting leg is the stance leg and the other is the swing leg.

Research on biped locomotion can be classified into three major directions: postural stability analysis, control and gait generation (Fig. 1.4). Biped is posturally stable if it is able to keep itself upright and maintain the posture. Stability of a bipedal activity such as walking, hopping and jumping is analyzed by looking into its postural stability while performing those activities. Several techniques are reported for postural stability analysis which is discussed subsequently in this dissertation.

Biped locomotion is realized by combination of time-functions of angular positions and velocities of its joint actuators. Such time-functions are called trajectories. The combination of joint trajectories is known as gait. Computing gaits for ceratin activity is known as gait generation. Gait generation essentially brings in issues associated with biped's postural stability. Gaits are modified based on the postural stability of the biped (Fig. 1.4). Reported gait generation techniques are discussed in section 1.4. Gaits are implemented into the biped's joint actuators by providing appropriate control inputs. Proper choice of control inputs at the actuators achieve specific joint positions and velocity profiles. Actuator-level control design is a key aspect to look into because of its importance in proper realization of gaits. Relevant literature on

control system design is explored in section 1.3.

In this dissertation, various aspects of postural stability analysis, gait generation and control design are looked into for biped locomotion. Bipedal robots are modeled by a set of higher-order nonlinear differential equations. Such equations are known as biped dynamics. Knowledge of biped dynamics depends on the knowledge of certain mechanical parameters of the biped.

Biped robots are often considered as open kinematic chain during single-support phase. The dynamical equations of such open kinematic chains are as per (1.1).

$$M(\theta)\ddot{\theta} + V(\theta, \dot{\theta}) + G(\theta) = \tau, \tag{1.1}$$

where M is the $n \times n$ inertial matrix about toe (of the supporting leg) with n being the number of DOF of the biped, V is $n \times 1$ vector containing Coriolis, centrifugal terms, and G is the $n \times 1$ gravity vector, τ is the external force/torque vector and θ is the joint angular position vector. The computations of M, V and G are usually performed using Newton-Euler dynamics formulation or Lagrangian dynamics formulation [4, 5].

With biped being modeled as Lagrangian dynamics (1.1), an appropriate control design computes the external input τ to realize "stable" biped gaits. The word - "stability" - can be defined and analyzed in various perspectives. In biped locomotion, "stability" can be in two perspectives. The first notion is of "stability" in bipedal gaits - normally referring to the postural stability of the biped while executing the gaits. Postural stability can be either static stability, dynamic stability [6] or orbital stability/periodicity [7]. A statically stable gait is one where the bipeds Center of Mass (CM) does not leave the support polygon[1]. The "statically stable" biped gaits are posturally stable in every posture associated with the gait. Biped is able to

[1]The convex hull of the foot-support area is the support polygon (Fig. 1.5).

keep itself upright during the entire statically stable gait. In statically stable gaits, the biped is posturally stable even if it become stationary. On the other hand, in "dynamically stable" gait the biped is able to keep itself upright even if the gaits have certain posturally unstable phases. Loosely, a dynamically stable gait is a periodic gait where the bipeds center of pressure (CP) leaves the support polygon and yet the biped does not overturn. The "orbital stability" is a special case of dynamic stability. In orbital stability, ceratin postures are attained periodically. Such postures might be posturally unstable i.e., the biped is upright but would not be able to maintain the posture for long time.

The second notion is of "stability" in biped dynamics - normally refers to the stability issues associated with the biped dynamics. Such notion of stability is used in actuator-level control design. Stability of biped dynamics can be either in the sense of Lyapunov or Bounded Input Bounded Output (BIBO). "Stability in the sense of Lyapunov" is based on the Lyapunov's work, *The General Problem of Motion Stability*, which was publishes in 1892. Lypunov's work includes two methods - so-called linearization method and direct method. The linearization method draws conclusions about the nonlinear system's local stability around an equilibrium point from the stability properties of its linear approximation [8]. The direct method is not restricted to local motion, and determines the stability properties of a nonlinear system by constructing a scalar "energy-like" function for the system and examining the function's variations [8]. On the other hand, BIBO stability mainly addresses boundedness properties of the system input, output and intermediate states.

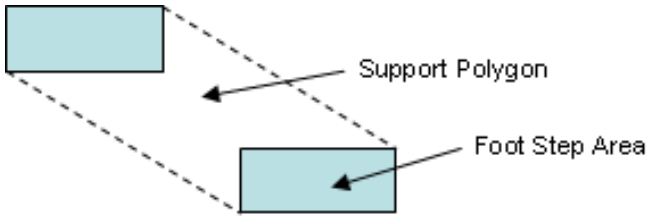

Figure 1.5: Support Polygon.

1.2 Postural Stability

The postural stability of bipedal systems depends on the presence, shape and size of the feet. The convex hull of the foot-support area is the support polygon (Fig. 1.5). Postural stability of bipeds is often analyzed by the locations of the certain reference points on the surface on which the biped is located. Such ground reference points depend on various dynamical parameters and mechanical structure of the biped. A number of ground reference points are reported in the literature to investigate the postural stability of the biped locomotion. Zero-Moment-Point (ZMP) [9] and Foot-Rotation-Indicator (FRI) Point [10] are the most useful ground reference points for bipedal postural stability analysis. While utilizing such concepts, the possibility of support foot rotation is often considered as lose of postural balance. Stability concepts like ZMP or FRI point investigate the possibility of such foot-rotation during locomotion. Such rotational stabilities of the foot link is termed as "rotational equilibrium"[2] of the foot. In some of the reported research, point-foot bipeds are used for anthropomorphic gait analysis [7,11,12]. The motivation of such biped models comes from the fact that an anthropomorphic walking gait should have a fully actuated phase where the stance foot is flat on the ground, followed by an *underactuated* phase

[2]The term "rotational equilibrium" is used in [10] to refer to the rotational properties of the foot.

where the stance foot heel lifts from the ground and the stance foot rotates about toe. The point-foot biped model is simpler than a more complete anthropomorphic gait model.

1.2.1 Zero-Moment-Point

Postural stability of legged systems is analyzed by the concept of ZMP introduced by Vukobratović in early nineties [6]. For systems with non-trivial support polygon area, the postural stability is commonly analyzed by Zero-Moment-Point (ZMP). ZMP is defined as the point on the ground where the net moment of the inertial forces and the gravity forces has no component along the horizontal axes. For stable (static) locomotion, the necessary and sufficient condition is to have the ZMP within the support polygon at all stages of the locomotion gait [6]. In Fig 1.6, (x_{zmp}, y_{zmp}) is the location of ZMP.

$$\begin{aligned} \vec{\tau}_{zmp} &= (\vec{r}_{cm} - \vec{r}_{zmp}) \times (M\vec{g} + M\vec{a}) = 0, \\ x_{zmp} &= x_{cm} - \frac{a_x}{a_z + g} Z_{cm} - \frac{\tau_y \vec{r}_{cm}}{Ma_z + Mg}, \\ y_{zmp} &= y_{cm} - \frac{a_y}{a_z + g} Z_{cm} + \frac{\tau_x \vec{r}_{cm}}{Ma_z + Mg}, \end{aligned} \tag{1.2}$$

where $\vec{r}_{cm}$ and $\vec{r}_{zmp}$ are the Cartesian position vectors of the CM and ZMP respectively, $\vec{\tau}_{zmp}$ is the moment at the ZMP.

Another well-known concept for analyzing postural stability of biped systems with non-trivial support polygon area is the center-of-pressure (CP). CP is defined as the point on the ground where the resultant of the ground-reaction-force acts. When ZMP

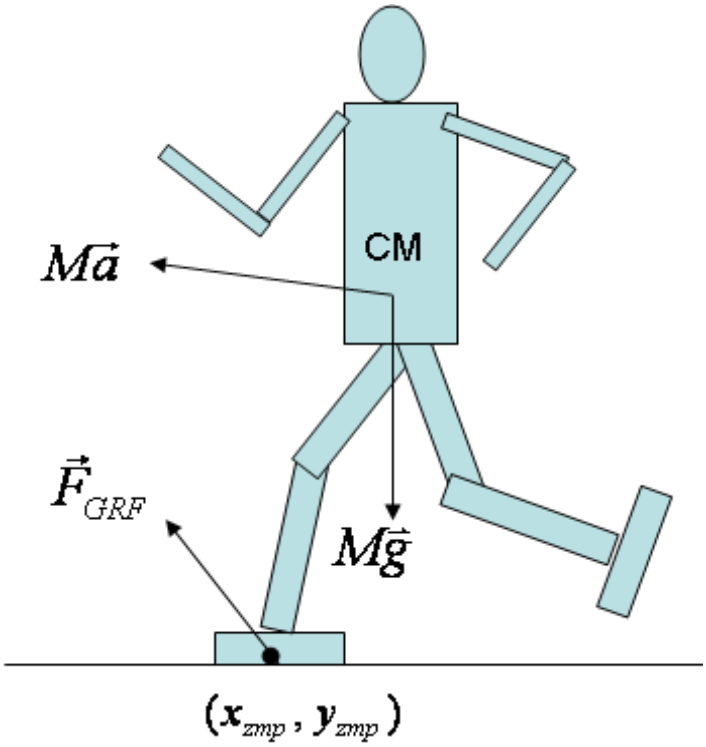

Figure 1.6: Zero-Moment-Point. M: Total Mass of the system, $\vec{a}$ is the linear acceleration, $\vec{F}_{GRF}$ is the ground-reaction force, ZMP (x_{zmp}, y_{zmp}) is where $\vec{F}_{GRF}$ acts.

is within the support polygon created by the robot feet, CP coincides with ZMP [10]. CP is not defined outside the foot support polygon. Therefore, if ZMP falls outside the foot support polygon, that point is termed as Fictitious ZMP (FZMP) [9] or Foot-Rotation-Indicator (FRI) Point [10]. If ZMP falls outside the support polygon, the biped becomes unstable. The degree of instability is indicated by its distance from the foot boundary. The stability concepts such as FZMP or FRI is addressed in detail in the subsequent chapters of the dissertation.

While using the concept of ZMP for postural stability analysis, the biped dynamics is very often replaced by a simplified model which approximately reflects the dynamic behavior of the original system to minimize the difficulty in computing and analyzing full system dynamics. The idea of replacing the whole biped with a concentrated mass at the CM, is widely used for the simplification of ZMP-based stability analysis. Such simplified models are commonly referred as inverted pendulum models (IPM) [13,14].

In Fig. 1.7, the entire biped model is replaced by one mass placed at the location of the CM (x_{cm}, y_{cm}, h). If the vertical height of the CM is kept constant during locomotion, the dynamic behavior of the system is expressed by (1.3).

$$\begin{aligned} \ddot{x}_{cm} &= \frac{g}{h} x_{cm} + \frac{1}{mh} \tau_y, \\ \ddot{y}_{cm} &= \frac{g}{h} y_{cm} - \frac{1}{mh} \tau_x, \end{aligned} \tag{1.3}$$

where g is the gravitational acceleration, (τ_x, τ_y) are the torques applied about the x and y-axes respectively. Let (x_{zmp}, y_{zmp}) be the position of the ZMP.

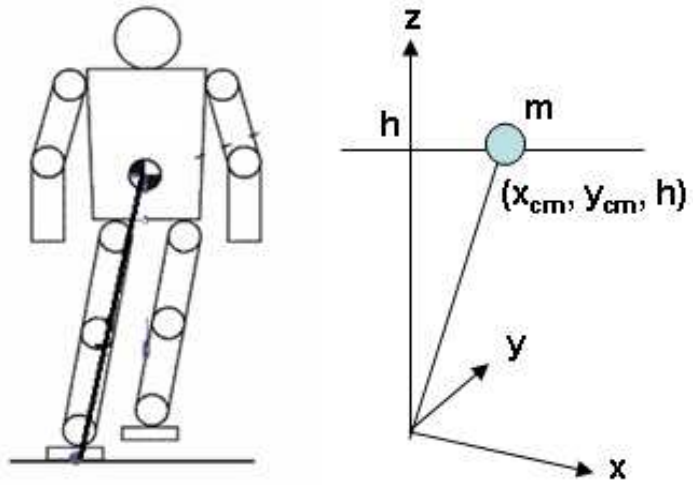

Figure 1.7: Inverted Pendulum Model.

$$\begin{aligned} x_{zmp} &= -\frac{\tau_y}{mg}, \\ y_{zmp} &= \frac{\tau_x}{mg}. \end{aligned} \tag{1.4}$$

Using (1.4) in (1.3) the ZMP expressions become,

$$\begin{aligned} x_{zmp} &= x_{cm} - \frac{h}{g}\ddot{y}, \\ y_{zmp} &= y_{cm} - \frac{h}{g}\ddot{x}. \end{aligned} \tag{1.5}$$

(1.3), (1.4) and (1.5) provide a linear model to manipulate the position of the CM. Such a linear model is well-known as the Linear Inverted Pendulum Model (LIPM) for its linearity [13, 14]. In [13, 14], the LIPM is used for checking and maintaining ZMP criterion in real-time. The CM is manipulated according to the reference ZMP. In [14],

the ZMP tracking problem is formulated as a servo problem. The ZMP reference is tracked using LIMP by a method called preview control which uses future inputs to compute the present output. In [16], two-mass inverted pendulum model is used for designing linear optimal control, which uses ZMP as a feedback, to track the ZMP trajectory.

Another approach for simplifying biped dynamics is to identify the loosely coupled components and decouple the original dynamics into a number of linear and lesser complex dynamics. In [17], the reference ZMP positions are tracked by a decoupled and linearized version of the complete biped dynamics.

1.2.2 Foot-Rotation-Indicator Point

During biped locomotion, "rotational equilibrium" of the foot is an important criterion for the evaluation and control of bipedal gaits. FRI is defined as the point on the foot-ground contact surface, within or outside the support polygon, at which the resultant moment of the force/torque impressed on the foot is normal to the surface. Alternatively, FRI point is the point on the foot-ground contact surface where the net ground-reaction-force would have to act to prevent foot-rotation. The location of the FRI point indicates the existence of unbalanced torque on the foot i.e., possibility of foot-rotation. The further away the FRI point from the support polygon boundary is, the more the possibility of foot-rotation and greater the instability. In Fig 1.8, X_{FRI} is the location of the FRI point. The expression of the FRI point is given by,

$$X_{FRI} = X_{Ankle} + \frac{-MZ_{Ankle}\ddot{X}_{CM} + M_{foot}g(CM^{x}_{foot} - X_{Ankle}) + \tau_{Ankle}}{Mg + M\ddot{Z}_{CM}}. \qquad (1.6)$$

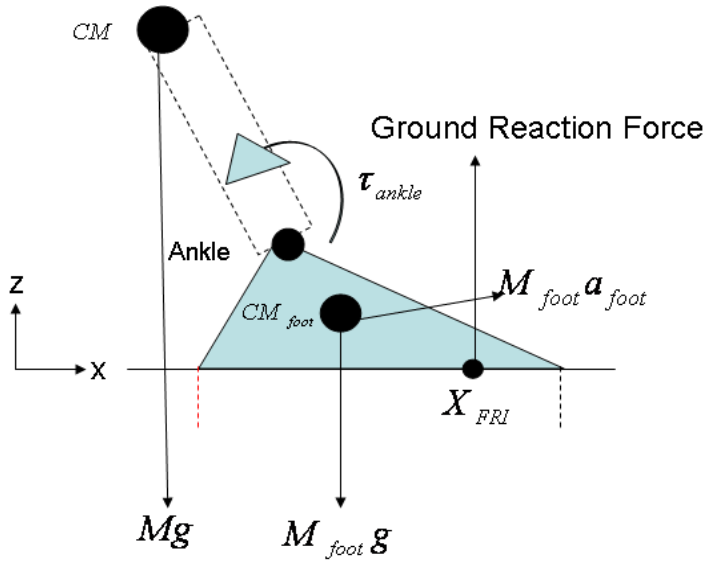

Figure 1.8: FRI Point. M: Total mass, M_{foot}: Foot mass, a_{foot}: Foot acceleration, τ_{ankle}: Torque input at the ankle joint, CM_{foot} : CM of the foot.

For a stationary robot, the rotational equilibrium of the feet is determined by the location of the ground projection of the center-of-mass (GCM). However, when the robot is in motion, the rotational properties of the foot are decided by the position of the Foot-Rotation-Indicator (FRI) point [10]. FRI point coincides with ZMP/CP when it is located within the support polygon. If it falls outside the support polygon, that indicates postural instability. The FRI point explains similar scenarios as FZMP[3].

The FRI point is utilized by a number of researchers for analyzing stability in biped locomotion [3,18,19]. In [3,18], the FRI concept is used for generating periodic anthropomorphic biped locomotion. The walking process is divided into two phases: fully-actuated phase during flat-foot stance phase and *underactuated* phase while the

[3] [9] describes FRI point to be same as FZMP or ZMP when located outside the support polygon.

heel lifts off the walking surface. Conditions are established using FRI to ensure periodic occurrence of the two phases. In [3], a method is described for directly controlling the position of the FRI point using ankle torque.

1.2.3 Biped Model With Point-Foot

From recent literature [7,11,12] it is noticed that several researchers are investigating the stability of biped systems with point foot i.e., biped without foot-link. Due to the absence of foot-link (and support polygon), stability concepts such as ZMP and FRI are not applicable to such systems. The concepts like orbital stability and periodicity are useful for analyzing the stability of such bipedal systems.

The success of Raibert's control law for a one-legged hopper [11] motivated others to analytically characterize the stability of the point-foot biped systems. Due to the absence of statically stable posture in single-support phase (except when CM coincides with the point-foot), the locomotion studies of point-foot biped systems are mainly performed for periodic activities such as walking, running, hopping or jogging (not standing or jumping) (Fig. 1.9). Absence of active actuation at the joint between point-foot and the ground makes these systems *underactuated*. The stability of the underactuated systems is essentially governed by its non-trivial *zero-dynamic*[4] [77]. The *zero-dynamics* of such bipeds does not have any stable equilibrium or posturally stable posture [7]. However, the zero-dynamics can move from one bounded unstable solution to another periodically, leading to bounded zero-dynamics. The concepts of orbital stability and periodicity are applied to establish the periodicity of zero-dynamics by Raibert [11] and Koditchek [12]. In [12], Poincare return map is used

[4]The concepts of zero-dynamics is discussed in detail in section 1.3.

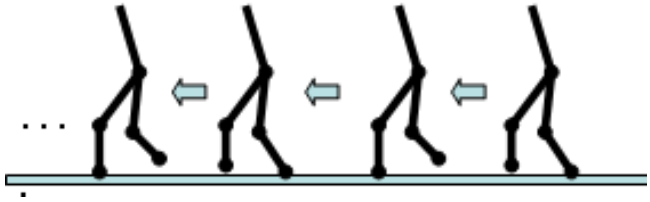

Figure 1.9: Periodic Motion.

to show periodicity of motion of a simplified spring-damped hopping robot. Similar concept is used by Grizzle et al. [7] to establish the conditions of periodicity for stable walking/running of a planar point-foot biped.

1.3 Actuator-level Control

Bipedal gaits are implemented by designing appropriate control inputs for the actuators. Several control approaches for gait generation are reported in the literature.

The traditional control approach [20–22, 59] is to generate the gaits by means of generating joint-trajectories and controlling each joint for trajectory-tracking so as to mimic the human locomotion. The trajectory-based control is either performed by decoupled control-techniques or simplification of robot dynamics. While using decoupled control-techniques to each joint actuators, the effects of the other dynamical components are treated as disturbances [16, 24]. The complexity of the robot dynamics necessitate significant simplification of the dynamic equations to generate the actuator-level control input and the control is designed based on the simplified dynamical equations [13, 14, 53]. The trajectory-based control is inefficient in energy usage [25, 26]. The joints are encumbered by motors and high-reduction gearing, making joint movements inefficient when the actuators are switched on to control.

Nevertheless, trajectory-based control techniques are still versatile and successful in biped locomotion.

In direct contrast to trajectory-based control, passive dynamic walking pioneered by Ted McGeer [44, 82] is another approach towards bipedal walking. Passive dynamic walkers make use of inherent dynamics of the mechanism to generate stable periodic walking motions [25, 61]. Collins [83] successfully built the world's first 3D passive-dynamic walker that can walk down a 3^o slope without any actuation. Subsequently, the group developed a minimally powered version of the passive-dynamic walker (Cornell biped) [26].

Biologically-inspired bipedal locomotion control is yet another popular area currently under research. There exist intra-spinal neural circuits capable of producing syncopated oscillatory outputs controlling the walking pattern in vertebrates [85]. These neural circuits are often termed neural oscillators or Central Pattern Generator (CPG). Complete quadrupedal stepping [64], for example, in a cat can be generated on a flat, horizontal surface, when a section of its midbrain is electrically stimulated. Nakanishi [65] used learning for bipedal locomotion. Morimoto [66] used reinforcement learning adaptation for walking down the slope which was implemented on a 5-link biped model. In some reported works, the dynamical effects of robotic systems are taken care of by learning techniques such as neural network or cerebellar-model articulation computer (CMAC) . In [54–56], the neural network is used to predict the dynamical effect of the robot to design actuator-level control inputs.

Non-linear control-techniques are often used to achieve accurate lower level control goal in robotic applications [4, 50, 52]. Such techniques are especially utilized when the biped dynamics is known with sufficient accuracy. In this dissertation, mainly

non-linear control techniques are used for actuator-level control. Most commonly used control techniques are *input-output linearization* [8] and *output-zeroing* [77]. In the following discussions various non-linear control techniques and terminologies are explained. Consider the non-linear system and output function as (1.7).

$$\begin{aligned} \dot{x} &= f(x) + g(x)u, \\ y &= h(x). \end{aligned} \tag{1.7}$$

where x is the state vector, u is the input vector and $f(.)$, $h(.)$, $g(.)$ are vectors of non-linear functions. A specific example of (1.7) system is given by (1.8).

The *input-output linearization* [8] and *output-zeroing* are explained based on the example equations given in (1.8).

$$\begin{aligned} \dot{x_1} &= sin(x_1) + x_2, \\ \dot{x_2} &= x_2^2 + u, \\ y &= x_1. \end{aligned} \tag{1.8}$$

The objective is to design the input u such that the state x_1 tracks a desired trajectory $x_1^d(t)$. The desired $x_1^d(t)$ is such that its time derivatives, up to a sufficiently high order, are assumed to be known and bounded.

Input-output linearization [5] The key aspect of the method is to find a direct relation between the system output y(t) and input u(t). Consider (1.8) for example,

[5]Refer to Chapter 6 in [8] for more details.

$$\begin{aligned} \dot{y} &= \dot{x_1} = sin(x_1) + x_2, \\ \ddot{y} &= cos(x_1)(sin(x_1) + x_2) + x_2^2 + u = N(x) + u. \end{aligned} \tag{1.9}$$

Choice of input $u = -N(x) + v$ results in a simple linear double-integrator relationship (1.10) between the output y and the new input v.

$$\ddot{y} = v. \tag{1.10}$$

With v being as per (1.11), the closed-loop dynamics becomes $\ddot{e} + k_2\dot{e} + k_1 e = 0$.

$$\begin{aligned} v &= \ddot{x}_1^d(t) - k_1 e - k_2 \dot{e}, \\ e &= x_1(t) - x_1^d(t). \end{aligned} \tag{1.11}$$

The output function y is differentiated once or more to get an explicit relationship between output and input. If the output function is differentiated r times to generate as explicit relationship between the output (y) and input (u) functions, then the *relative degree* of the system is r. In this example, the relative degree of the system is two. For all controllable systems, $r \leq n$.

Output-zeroing [6] This method is similar to the input-output linearization method except that the output functions are chosen such that the system objectives are achieved when the output is zero. Hence, the objective reduces to achieving a zero output. Consider (1.8) as example. To convert the problem into the output-zeroing form, the output function can be chosen as $y(t) = x_1(t) - x_1^d(t)$. When y(t) = 0, $x_1(t) = x_1^d(t)$.

[6] Refer to Chapter 8 in [77] for more details.

1.3.1 Internal dynamics and Zero-dynamics

Input-output linearization and output-zeroing techniques are motivated in the context of output tracking. The output function can be one state or a combination of various states. However, such techniques do not essentially guarantee that all the system states are stable even in the sense of BIBO. For example, if $x_2 \rightarrow \infty$ in the example (1.8) with $u = -N(x)+v$, the input function also becomes unbounded i.e., $u \rightarrow -\infty$. Hence, even if the output y is tracked, the system is not BIBO stable. Such stability issues brings in the concepts such as *internal dynamics* and *zero-dynamics* [8, 77, 98].

In the system given by (1.8) with $u = -N(x) + v$, a part of the dynamics (1.10) has been rendered "unobservable"[7] in the input-output linearization/ output-zeroing techniques. This part of the dynamics is called *internal dynamics*, because it can not be seen from the external input-output relationship. In the example, the internal dynamics is represented by the equation,

$$\dot{x}_2 = x_2^2 - N(x) + v. \tag{1.12}$$

For stable tracking control design, the internal dynamics should be BIBO stable. Therefore, the effectiveness of the control techniques depends on the stability of the internal dynamics.

The *zero-dynamics* (ZD) is defined as the internal dynamics of the system when the system output is kept at zero by the input [8, 77]. ZD for the example (1.8) is given by (1.13).

$$\dot{x}_2 = x_2^2 - N(x) + v|_{x_1 = x_1^d}. \tag{1.13}$$

[7] Although observability is not defined for nonlinear systems, the word -"unobservable"- is used for better understanding as per [8].

If $x_1^d = 0$, (1.13) leads to $\dot{x}_2 = -x_2$. For the linear systems stability of internal or zero dynamics is determined by the locations of the system zeros and the stability of ZD implies global stability of the internal dynamics. The study of ZD is a simpler way of determining the stability of the internal dynamics. The local asymptotic stability of ZD guarantees the local stability of the internal dynamics.

In nonlinear systems only local stability is guaranteed for the internal dynamics even if the zero-dynamics is globally stable. For non-linear systems, further stability analysis is required to ensure stability of the associated internal dynamics.

In the presence of foot-rotation, the biped dynamics have an additional passive degree-of-freedom due to the joint between toe and ground. Such biped dynamics has nonlinear two-dimensional zero-dynamics, stability of which is essential for the stability of the biped locomotion with foot-rotation.

1.4 Gait Generation

The most strait-forward approach to generate the biped joint trajectories is by solving inverse kinematics [50]. With the increase in DOF of the robot, it becomes computationally impractical to compute inverse kinematics. However, such an approach is suitable for off-line generation of the joint trajectories. Gait generation further involves major research directions such as actuator-level trajectory generation using simplified bipedal models [15, 27–29], joint trajectory generation based on postural stability analysis [13,14,17,50], biologically inspired approaches to generate gaits and, learning and optimization of bipedal gaits [45–48].

Dynamics of biped systems is non-linear and difficult to analyze [6]. In certain studies simplified biped models are utilized. The most popular and widely used model

is the Inverted Pendulum Model [15, 27–29]. In this model the whole body is replaced with a concentrated mass located at the center-of-mass (CM). Bio-mechanical concepts and inverted pendulum models are often utilized to generate walking gaits for simplified two-legged mechanisms [26, 44]. Inverted pendulum model is useful for stability analysis of bipeds by computing the ZMP which is the point on the ground where the resultant of every moment is zero [29]. Combining one DOF inverted pendulum model for the stance leg and two DOF inverted pendulum model for the swing leg simplifies the walking gait generation [27]. Self-excitation control of inverted pendulum model leads to passive dynamic walking [28]. A running-cart-table model simplifies the estimation of variation in ZMP during bipedal activities [14]. Energy optimal gait is achieved in [51].

The postural stability of legged systems is ensured by keeping the ZMP within the area covered by foot, i.e. the support polygon. The most common approach for gait generation is to compute joint trajectories maintaining postural stability using system dynamics [13, 14, 17]. Decoupling the subsystems reduces the complexity in bipedal gait generation [30]. Decoupled and linearized dynamic equations simplify ZMP computation [17]. Injection of torque at the ankle provides ZMP compensation to maintain postural stability during various bipedal activities [99]. By maintaining the CM at a specific height, the linear inverted pendulum model generates stable walking gait [13]. ZMP based gait generation is utilized by the ASIMO humanoid [39].

Biologically inspired approaches generate natural walking gaits [45–48] for biped locomotion [31, 32, 40, 41]. Neural oscillators are suitable for learning stable walking patterns on unknown surface conditions [31]. Genetic Algorithm (GA) is an effective

tool to optimize neural oscillators generating natural walking patterns [32]. In biological systems, Central Pattern Generators (CPG) produce the basic rhythmic leg movements as well as leg coordination [42, 43]. Biological locomotion mostly relies on CPG and sensory feedback (reflexive mechanism) [42, 43]. The concept of CPG is realized using adaptive neural oscillators in [40]. Human-like reflexive-mechanisms are often used for learning walking gaits [41].

1.5 Dissertation Outline

The inverse kinematics of a twelve DOF biped robot is formulated in terms of certain parameters. The biped walking gaits are developed using the parameters. The walking gaits are optimized using Genetic Algorithm. The optimization is carried out considering relative importance of stability margin and walking speed. The stability margin depends on the position of Zero-Moment-Point (ZMP) while walking speed varies with step-size. ZMP is computed by an approximation-based method which does not require system dynamics. The optimal walking gaits are experimentally realized on a biped robot. The research on walking gait optimization is discussed in Chapter 2.

A novel method of ZMP compensation is proposed to improve the stability of locomotion of a biped which is subjected to disturbances. A compensating torque is injected into the ankle-joint of the foot of the robot to improve stability. The value of the compensating torque is computed from the reading of the force sensors located at the four corners of each foot. The effectiveness of the method is verified on a humanoid robot, MANUS-I. With the compensation technique, the robot successfully rejected disturbances in different forms. It carried an additional weight of 390 gm (17% of

body weight) while walking. Also, it walked up a 10^o slope and walked down a 3^o slope. Chapter 3 discusses the ZMP compensation method and various applications.

Landing stability of jumping gaits for a four-link planar two-legged robot is studied. Rotation of the foot during jumping leads to underactuation due to the passive degree-of-freedom at toe resulting in non-trivial *zero-dynamics*. Compliance between the foot and ground is modeled as a spring-damper system. Foot rotation along with compliance model introduce switching in the *zero-dynamics*. The stability conditions for the "*switching zero-dynamics*" and closed-loop dynamics are established. The stability of the switching zero-dynamics is investigated using Multiple Lyapunov Function [93] approach. "*Critical potential index*" and "*critical kinetic index*" are introduced as measures of the stability of the closed-loop dynamics of the biped during landing. Landing stability is achieved utilizing the stability conditions. Stable jumping motion is experimentally realized on a biped robot. The research on jumping gait and landing stability analysis are discussed in Chapter 4.

The stability of a planar biped robot is investigated in perspective of foot rotation during locomotion. With foot already rotated, the biped leads to tip-toe configuration which is modeled as an underactuated planar two-link kinematics. The stability of the tip-toed biped robots is analyzed by introducing the concept of "rotational stability". The rotational stability investigates if the biped would lead to a flat-foot posture or topple forward from the particular tip-toe configuration. The rotational stability is quantified by the location of a ground reference point named as "rotational stability index (RSI)" point. The conditions are established to achieve rotational stability of a planar tip-toed biped using the concept of RSI point. The studies are validated in simulations and are experimented in a biped robot. The traditional stability criteria

such as ZMP [9] and FRI [10] are not applicable to analyze biped stability when foot is already rotated. The RSI point is established as a stability criteria for bipedal stability even in the presence of foot rotation. Chapter 5 discusses the RSI point and its applications.

Conclusions are drawn and future research scopes are discussed in section 6.

Chapter 2

Biped Walking Gait Optimization considering Tradeoff between Stability Margin and Speed

Several techniques exist to learn and optimize bipedal gaits based on objectives such as minimizing energy consumption, maximizing stability margin, speed and learning rate. Neural Network (NN) [15, 31, 32, 41, 42], reinforcement learning (RL, Geng) [31], imitation-based approaches [33] and GA [32, 38] are tools used for learning and optimization of bipedal gaits.

Neural Network (NN) is a tool for functional approximation. NN is a widely used technique for gait generation. Unsupervised and supervised learning methods are adopted in training NN. Reinforcement learning [32] (unsupervised) [31, 49] and, human motion capture data (supervised) are useful training tools for NN. Human motion capture data and GA are utilized to train NN for bipedal gait generation [33]. In the unsupervised approach, the learning process is dependent on the feedbacks from the training environment [41]. Supervised training of NN requires large number of training data for generalization.

Reinforcement Learning (RL) is yet another adaptive learning tool. RL relies

on sensory feedback from the environment [31, 49]. The associated learning process should utilize enough training data to enhance the generalization capabilities of the learned gaits, which is a tedious task. It is desirable to utilize the kinematic and dynamic models for faster dynamic walking.

Visual information of human locomotion or motion capture data are often used in biped locomotion to imitate human walking gait [33]. Performance of the imitation-based approaches depends on the vision systems used for capturing motion data. They are difficult to experimentally realize due to lack of dynamical analysis and hardware restrictions.

A genetic algorithm (GA) is a search technique used in computing to find exact or approximate solutions to optimization and search problems. GA is a powerful tool to resolve the issues related to the optimality of biped gaits [32,38]. GA is utilized for bipedal gait generation by minimizing a weighted cost function of the input energy and ZMP error, generating training data set for a three layer NN [38]. However, the effects of hardware and mechanical constraints are not clearly brought out due to lack of experimental validation. The impact of variations in parameters and walking speed on dynamic stability is also not addressed.

Apart from the optimal training of NN, GA is useful for other purposes in bipedal locomotion. Some researchers [34, 36] used GA to smoothen the path followed by a biped robot avoiding obstacles. GA optimized *computed-torque* control architecture improves actuator-level control [35]. GA optimized spline trajectories result in bipedal gaits with minimal energy consumption [37].

In this research[1], GA is utilized to optimize the gait parameters in solving the

[1]The work is published and details of the publication are "Goswami Dip, Vadakkepat Prahlad and Phung Duc Kien, *Genetic algorithm-based optimal bipedal walking gait synthesis considering*

inverse kinematics model. The walking gaits are generated based on the optimal walking parameters. The description of the biped, actuators and the mechanical design are provided in Section 2.1. Inverse Kinematics is formulated for a twelve DOF biped robot in terms of certain gait parameters. Inverse kinematic model and walking gait generation are described respectively in Sections 2.2 and 2.3. The walking gaits are optimized using GA considering the relative importance between stability margin and speed of walking. Section 2.5 discusses the GA based gait optimization. The ZMP computation method for gait optimization is outlined in Section 2.6. The optimized walking gait is experimentally realized on a biped robot. The tradeoff between walking speed and stability margin are brought out. With increase in speed, walking becomes dynamic (less stable) and vice versa. The experimental results are discussed in Section 2.7, while the chapter is concluded in Section 2.8.

2.1 Biped Model, Actuators and Mechanical Design

The biped robot, Bio Robotics Application in Locomotion (BRAIL 1.0), considered consists of two legs (Fig. 2.3). The waist-link connects the two legs. Each leg has three links: foot-link, shank-link and thigh-link. The joint between the foot-link and shank-link is the ankle, the joint between shank-link and thigh-link is the knee while the one between thigh-link and waist-link is the hip. The biped has twelve DOF. Two DOF at ankle, one DOF at knee and three DOF at hip, i.e., six DOF in each leg (Fig. 2.1). Each DOF corresponds to an independent actuator.

tradeoff between stability margin and speed, Robotica (2008)."

Table 2.1: Parameters of the BRAIL 1.0.

Parameters	Values
m_1	0.07 Kg
m_2	0.02 Kg
m_3	0.14 Kg
m_4	0.21 Kg
d_1	0.19 Meter
d_2	0.15 Meter
w	0.12 Meter
L	0.02 Meter
B_x	0.1 Meter
B_y	0.14 Meter
F_{x1}	0.03 Meter
F_{x2}	0.07 Meter
F_y	0.055 Meter

The links are made of light-weight aluminium which leads to their little contribution to the overall mass or inertia of the link. The overall mass or inertia of the links are computed based on the positions and weights of the actuators which are located at the joints between two links. The link masses are assumed concentrated at the joints located at the distal ends. The mass distribution of the biped is shown in Fig. 2.2. 'd_1' indicates the thigh-link length and 'd_2' the shank-link length. 'F_y' and 'F_x' are the foot width and length. 'F_{x1}' and 'F_{x2}' are the distances from the ankle to the rear and front edges of the foot. 'B_y' and 'B_x' are the hip-link width and length. The distance between two hip-joints is 'w' and the distance between the ankle-joint and CM of the foot is 'L'. Table 2.1 provides the biped parameter values.

Dynamixel motors ($DX-113$) from Robotis Inc. (*www.tribotix.com*) are used as actuators. The motors are compact and light-weight (58 grams) providing high-torque (a maximum holding torque of 1.02 Nm). The motors have a control-network

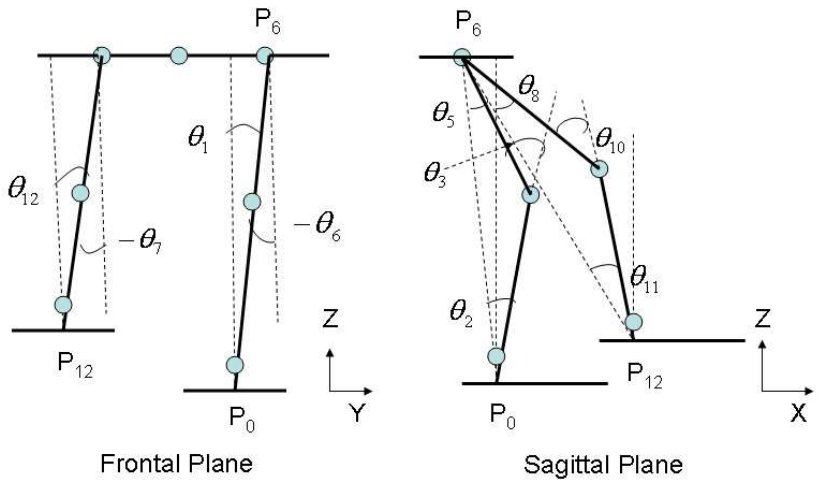

Figure 2.1: Generalized Coordinates.

with position and velocity feedbacks. Each motor along with associated mechanical components weighs around 70 grams which is reflected in Table 2.1. The control instructions are sent to the motors from MATLAB environment by RS-485 serial communication. The mechanical structure of the biped is shown in Fig. 2.3.

2.2 Biped Inverse Kinematics

2.2.1 Generalized Coordinates

The biped has twelve DOFs realized by twelve actuators placed at the joints. Any specific configuration of the biped is expressed by a 12×1 vector of generalized coordinates, $[\theta_1, \theta_2 \cdots \theta_{12}]^T$ as shown in Fig. 2.1.

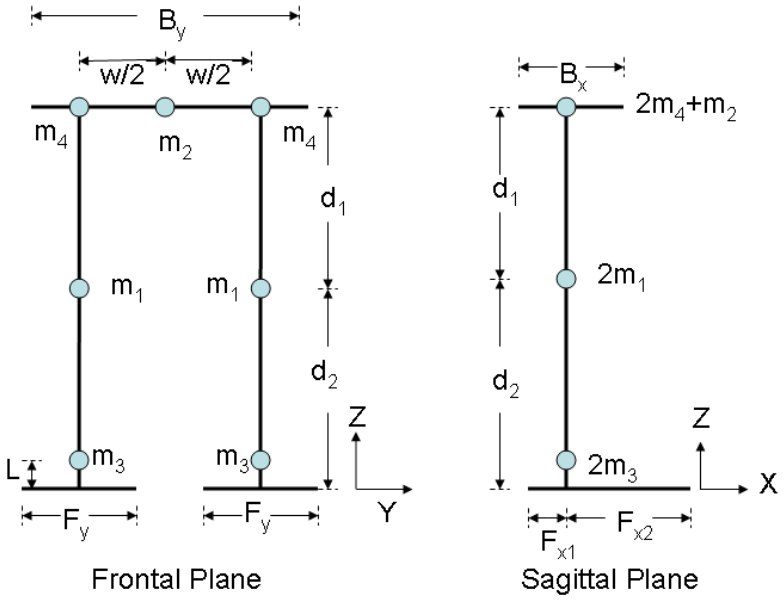

Figure 2.2: Biped model: Mass Distribution.

2.2.2 Inverse Kinematics

The Cartesian coordinates of the reference points $P_i(P_{ix}, P_{iy}, P_{iz})$ are shown in Fig. 2.4. $P_{0,12}$ are the ankle joints, $P_{3,10}$ are the knee joints, and P_6 is the hip joint. $P_{0,3,6}$ are joints of the stance leg and $P_{10,12}$ are the joints of the swing leg. Positions of the motors are such that the CM of the foot-links do not coincide with the ankle-joints. The point P_{0m} is the Cartesian coordinate of the CM of the stance leg foot-link while P_{12m} is that of the swing leg foot-link.

The inverse kinematic parameters are defined as (Fig. 2.5):

$$x_l = P_{0x} - P_{6x}, y_l = -P_{6y}, z_l = P_{0z} - P_{6z},$$
$$x_r = P_{12x} - P_{6x}, y_r = -P_{6y}, z_r = P_{12z} - P_{6z}. \quad (2.1)$$

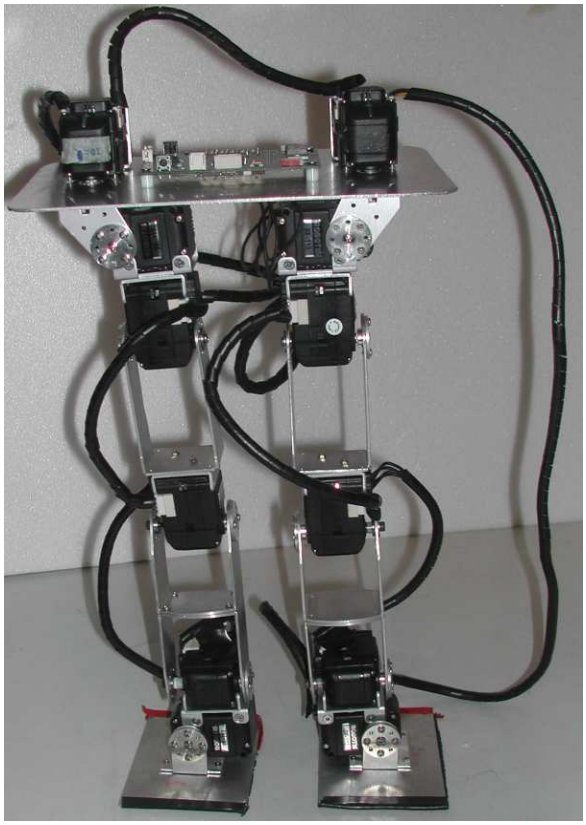

Figure 2.3: The Biped.

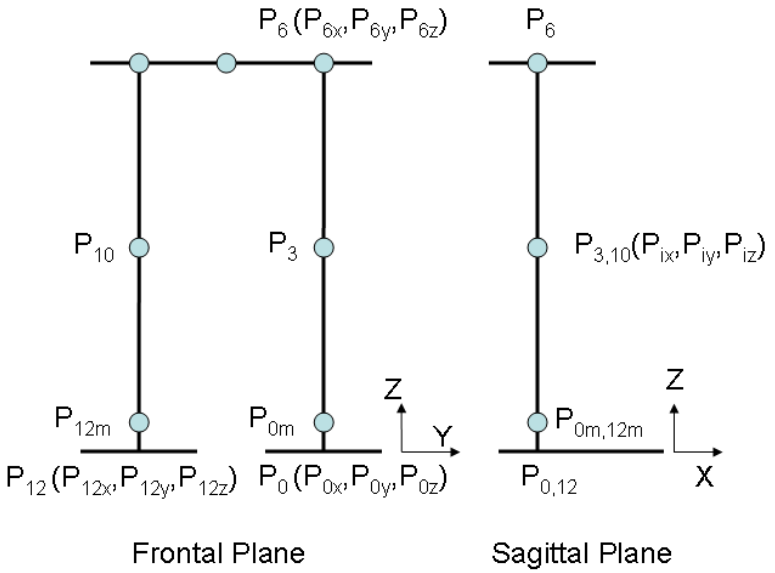

Figure 2.4: Biped Reference Points for Inverse Kinematics.

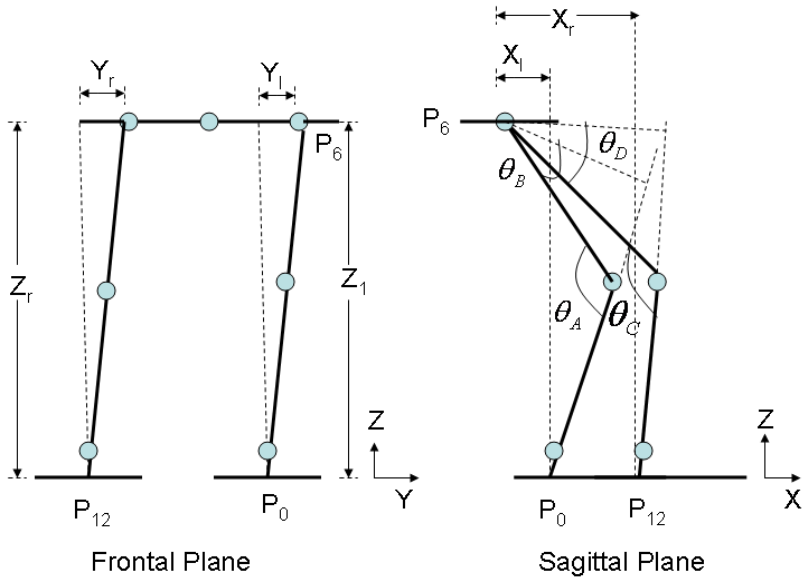

Figure 2.5: Biped: Inverse Kinematic Parameters.

x_l and x_r are the displacements of the hip along sagittal plane with respect to the corresponding ankle. y_l and y_r are the displacements of the hip along frontal plane with respect to the corresponding ankle. z_l and z_r are the heights of the hip from the ankle. Four angular quantities (Fig. 2.5) are defined as per (2.2).

$$\begin{aligned}
\theta_A &= cos^{-1}[\frac{d_1^2 + d_2^2 - x_l^2 - y_l^2 - z_l^2}{2d_1d_2}] \\
\theta_B &= cos^{-1}[\frac{d_1 sin(\theta_A)}{\sqrt{x_l^2 + y_l^2 + z_l^2}}] \\
\theta_C &= cos^{-1}[\frac{d_1^2 + d_2^2 - x_r^2 - y_r^2 - z_r^2}{2d_1d_2}] \\
\theta_D &= cos^{-1}[\frac{d_1 sin(\theta_C)}{\sqrt{x_r^2 + y_r^2 + z_r^2}}]
\end{aligned} \tag{2.2}$$

The expressions for the generalized coordinates in terms of the inverse kinematic parameters are provided in (2.3). For straight walking, $y_l = y_r$ and $\theta_4 = \theta_9 = 0$.

$$
\begin{aligned}
\theta_1 &= tan^{-1}(\frac{y_l}{z_l}), \\
\theta_{12} &= tan^{-1}(\frac{y_r}{z_r}), \\
\theta_6 &= -\theta_1, \\
\theta_7 &= -\theta_{12}, \\
\theta_3 &= \pi - \theta_A, \\
\theta_{10} &= \pi - \theta_C, \\
\theta_5 &= \frac{\pi}{2} - \theta_A + \theta_B + sin^{-1}(\frac{x_l}{\sqrt{x_l^2 + y_l^2 + z_l^2}}), \\
\theta_8 &= \frac{\pi}{2} - \theta_C + \theta_D + sin^{-1}(\frac{x_r}{\sqrt{x_r^2 + y_r^2 + z_r^2}}), \\
\theta_4 &= 0, \\
\theta_9 &= 0, \\
\theta_2 &= \theta_3 - \theta_5, \\
\theta_{11} &= \theta_{10} - \theta_8.
\end{aligned}
\tag{2.3}
$$

2.3 Biped Walking Gait

Walking gait is often defined as alternating phases of single and double support. The walking gait is expressed in terms of the following parameters (Fig. 2.6): step-length s, bending-height h, maximum lifting-height H, maximum frontal-shift n and step-time T. During walking, the height of the waist-link is kept constant.

The biped walking motion is generated by choosing an appropriate time function for the three reference points: the stance leg ankle-joint coordinate $P_0(P_{0x}, P_{0y}, P_{0z})$,

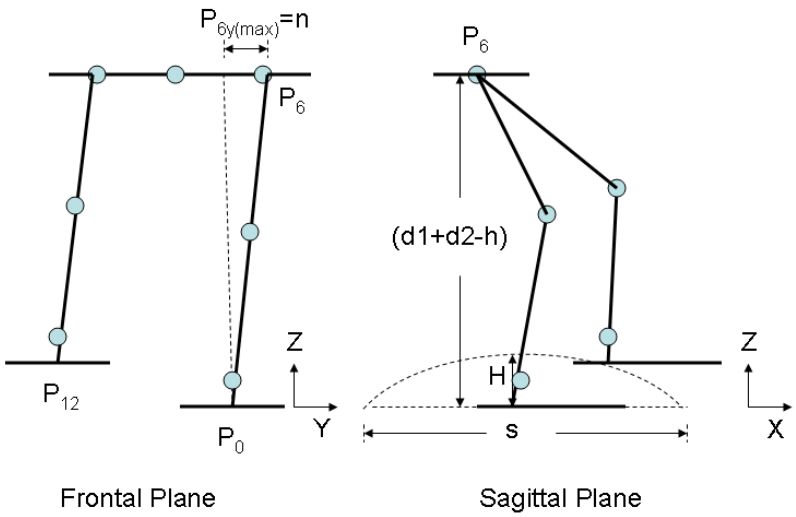

Figure 2.6: Gait Generation Parameters.

the stance leg hip-joint coordinate $P_6(P_{6x}, P_{6y}, P_{6z})$ and the swing leg ankle-joint coordinate $P_{12}(P_{12x}, P_{12y}, P_{12z})$. P_0 is stationary for $0 \leq t \leq T$ and acts as a reference for P_6 and P_{12}. For $T < t \leq 2T$, the positions of P_0 and P_{12} are interchanged. P_0, P_6 and P_{12} are chosen intuitively. P_0 and P_{12} are selected according to the desired leg movement for a specific activity. The choice of P_6 depends on the mechanical structure of the biped as it involves shifting of the ZMP from one foot to another.

In a walking cycle, $0 \leq t \leq 2T$, P_0 and P_{12} for straight walking are provided by (2.4).

$$
\begin{aligned}
P_{0x}(t) &= (\frac{s}{2})sin(\frac{\pi}{T}(t-\frac{T}{2}))(u(t-2T)-u(t-T)),\\
P_{0y}(t) &= -w(u(t-2T)-u(t-T)),\\
P_{0z}(t) &= Hsin(\pi(\frac{P_{0x}(t)}{s}+0.5))(u(t-2T)-u(t-T)),\\
P_{12x}(t) &= (\frac{s}{2})sin(\frac{\pi}{T}(t-\frac{T}{2}))(u(t)-u(t-T)),\\
P_{12y}(t) &= -w(u(t)-u(t-T)),\\
P_{12z}(t) &= Hsin(\pi(\frac{P_{12x}(t)}{s}+0.5))(u(t)-u(t-T)),
\end{aligned} \tag{2.4}
$$

where H, w, s, n are as shown in Fig. 2.6 and $u(.)$ is a unit step function given by (2.5).

$$
u(t) = \begin{cases} 1 & if\ t \geq 0, \\ 0 & otherwise. \end{cases} \tag{2.5}
$$

P_6 for straight walking is given by (2.6).

$$
\begin{aligned}
P_{6x}(t) &= (\frac{s}{4})sin(\frac{\pi}{T}(\tau-\frac{T}{2})),\\
P_{6y}(t) &= nsin(\frac{\pi}{2}(sin(\frac{\tau\pi}{2T})+1))sin(\pi\frac{t}{T}),\\
P_{6z}(t) &= (d_1+d_2-h),
\end{aligned} \tag{2.6}
$$

where for $0 \leq t \leq T$, $\tau = t$ and for $T \leq t \leq 2T$, $\tau = t - T$. When P_0, P_6 and P_{12} are as per (2.4) and (2.6), the biped robot walks straight. The walking gait is generated by sampling the functions (2.4) and (2.6) at certain intervals. In (2.4) and (2.6), t and T govern the sampling process which decides the walking speed and the smoothness of the walking gaits. With Δt as the sampling interval, $(\frac{T}{\Delta t})$ indicates the number of samples in T seconds or sampling frequency. A low sampling

rate ($\frac{T}{\Delta t}$) results in mechanical vibration during walking which can lead to erratic movement and instability. A high sampling rate ($\frac{T}{\Delta t}$) causes computational burden on the hardware making the walking process very slow. For a given system, the values of T and Δt should be chosen accordingly. There can be various combinations of walking parameters i.e. s, h, H and n that generate straight walking gaits. The details of the GA is discussed in Section 2.4 and the cost function to compute optimal walking parameters is illustrated in Section 2.5.

2.3.1 Choice of Walking Parameters

In single-support phase (of walking gaits), maximum frontal-shift n involves shifting of ZMP from one foot to another. For lower value of n, the biped might not be able to lift the foot from the ground. Therefore, the maximum frontal-shift n is an important parameter to choose walking gait. The bending-height h decides the height of the biped's CM. With higher CM, the stability margin during walking decreases. Moreover, torque/power requirement at ankle joint increase when CM is higher. It is desirable to keep the biped's CM at lower height to make it more stable. This leads to choice of the bending-height h as one of the walking parameters. The step-length s and maximum lifting-height H are different for various desired gaits. For example, H has to be at least higher than the height of the stair to climb the stair and step-length s will be half compared to s for the strait walking on flat surface. Therefore, the step-length s and the maximum lifting-height H are obvious choice for walking parameters.

The torque or power requirement at the biped's joints can be found out by computing exact biped dynamics. The computation of dynamics for twelve DOF structure

Table 2.2: Parameters of GA.

Parameters	Values
Chromosome Size	4
Population Size	30
No of Epoch	30
Mutation Rate	0.1
Crossover Rate	0.8

is both computationally expensive and impractical. In this research, we have not computed biped dynamics. However, it is possible to intuitively comment on the relations between torque/power requirements and the walking parameters. If we keep the step-length s and maximum lifting-height H low, the power consumption will lesser but speed of walking is dependent on s. Therefore, we need certain tradeoff between power requirement/speed. The more the value off the bending-height h, the more the torque/power requirement.

2.4 Genetic Algorithm

Genetic Algorithm (GA), with parameters in Table 2.4, is utilized to optimize the walking parameters by maximizing the cost function (2.11). The details of the cost function is discussed in section 2.5. The block diagram of the GA algorithm is shown in the Fig. 2.7. Floating point strings are used and the initial *population* is chosen randomly satisfying the constrains in (2.7). *Single-point crossover* is performed by swapping the values of two chromosomes after *tournament selection*. *Mutation* is carried out by flipping the values of *alleles*. For example,

$$\textit{Before Mutation:} \quad 0.05 \leq s = 0.07 \leq 0.13$$
$$\textit{After Mutation:} \quad s = (0.05 + 0.13) - 0.07.$$

2.5 GA Based Parameter Optimization

This section discusses the selection of the parameters s, h, H and n for straight walking, considering the step-time T as unity. The values of the parameters are computed considering a tradeoff between stability and speed of walking.

2.5.1 Constrains on Walking Parameters

Mechanical design of the biped robot brings constrains on the maximum and minimum ranges of feasible values of the walking parameters. Following are the constrains on the walking parameters which are arrived at experimentally with biped BRAIL 1.0 (Fig. 2.3).

$$\begin{aligned} 0.05 &\leq s \leq 0.13, \\ 0.001 &\leq n \leq 0.13, \\ 0.001 &\leq H \leq 0.13, \\ 0.001 &\leq h \leq 0.13. \end{aligned} \tag{2.7}$$

2.5.2 Postural Stability Considering ZMP

For legged systems with foot, the ZMP should fall inside the support polygon (Fig. 1.5) for postural stability. In double-support walking phase the both feet are in

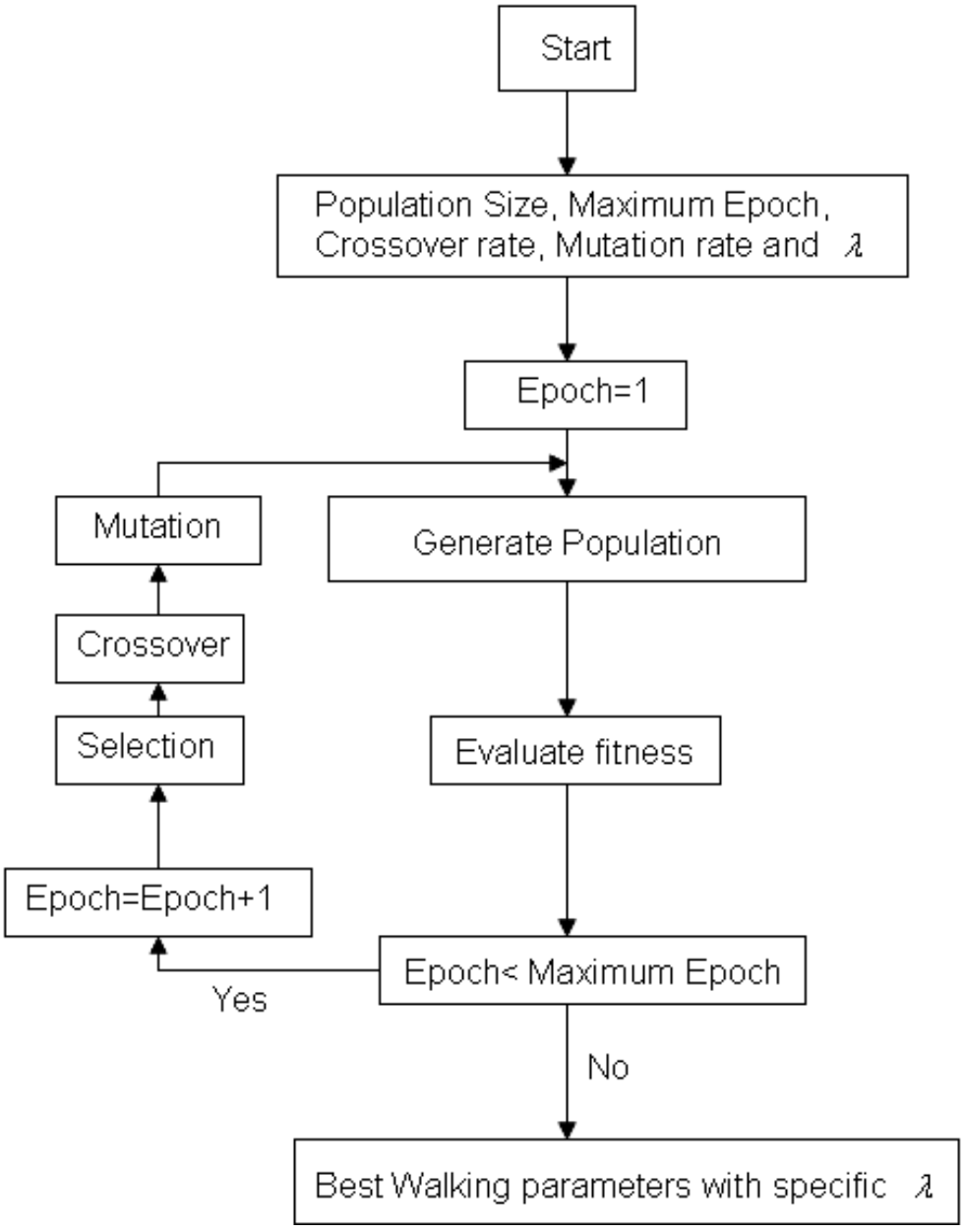

Figure 2.7: The GA algorithm for obtaining optimal walking parameters for a specific value of λ.

contact with the ground, while only the stance leg is in contact with the ground in single-support phase. During single-support phase, the area of the support polygon is same as the area covered by the stance leg foot. For postural stability in single-support phase, the ZMP must be located with the area covered by the foot.

For the biped model considered, let the Cartesian coordinate of the ZMP be $(x_{zmp}, y_{zmp}, 0)$. In single-support phase, the ZMP must be located in the area covered by the stance foot i.e., $F_x \times F_y$ (Fig. 2.2). According to the coordinate convention in the Fig. 2.2, foot link is located from $-F_{x1}$ to F_{x2} in sagittal plane and $-\frac{F_y}{2}$ to $\frac{F_y}{2}$ in frontal plane. The conditions for postural stability of the biped are (in single-support phase),

$$\begin{aligned} -F_{x1} \leq x_{zmp} \leq F_{x2}, \\ -\frac{F_y}{2} \leq y_{zmp} \leq \frac{F_y}{2}. \end{aligned} \tag{2.8}$$

Walking is static if the conditions in (2.8) are satisfied during the entire walking cycle. In dynamic walking, the conditions are not met for the entire walking cycle. In this work, the condition (2.8) is utilized to decide on the type of walking (static or dynamic) corresponding to a particular combination of walking parameters.

2.5.3 Cost Function

Stability of biped systems is quantified by the distance of its ZMP from the stance foot ankle-joint during single-support phase. Closer the ZMP $(x_{zmp}, y_{zmp}, 0)$ to the ankle-joint, greater the stability margin. Hence, the walking gait with maximum stability margin is obtained by minimizing (2.9).

$$Q = \int_0^T (x_{zmp}^2 + y_{zmp}^2)dt. \tag{2.9}$$

The walking parameters corresponding to the minimum value of Q generates gaits with maximum stability margin. When walking speed is factored in the optimization process, the step-length (*'s'*) appears in the cost function. Let us define functions,

$$\begin{aligned} f_1 &= \frac{1}{Q}, \\ f_2 &= s. \end{aligned} \tag{2.10}$$

Let the maximum numerical values of f_1 and f_2 are f_1^{max} and f_2^{max} respectively. The expression for the normalized cost function is given in (2.11).

$$f = \frac{\lambda f_1}{f_1^{max}} + \frac{(1-\lambda) f_2}{f_2^{max}}, \tag{2.11}$$

where $0 \leq \lambda \leq 1$. The cost function (2.11) has maximum value with either $\lambda = 1.0$ or $\lambda = 0$. λ is not used as a parameter in the GA-based optimization[2], rather it is left unchanged during the optimization process. The optimal walking gait parameters are obtained maximizing the cost function (2.11) for a specific value of λ. The walking parameters corresponding to $\lambda = 1$ generate the most stable gait[3]. Speed of walking is maximum when $\lambda = 0$. Intuitively, when the step-length *'s'* is smaller, stability margin is higher. Small step-length *'s'* produces slow walking. GA is utilized to obtain the optimal walking parameters by maximizing the cost function (2.11) after

[2] λ is kept constant during the optimization process. The effect of λ on walking performance is discussed in section 2.7.1.

[3] With the walking parameters corresponding to the maximum value of f_1.

selecting λ as a tradeoff between the walking speed and stability margin. Using GA, the optimal walking parameters are obtained for different λ values.

In the GA-based gait generation approach, the following points are noticeable:

- Bipedal gaits to follow curvilinear paths are generated by choosing appropriate expressions for the hip yaw angles θ_4 and θ_9 in (2.3). For example, $\theta_9 = K$, a positive constant for $0 \leq t \leq T$ and $\theta_4 = K$ for $T < t \leq 2T$ makes the robot move in a circular path. Due to mechanical constraints and walking stability, $K \leq 8^0$ and $\lambda \geq 0.7$ are maintained.

- Various kinds of bipedal locomotion (for example stair climbing, obstacle avoiding) can be generated using the inverse kinematics (2.3). However, the expressions for P_0, P_6 and P_{12} in (2.4) and (2.6) will change for different activities. Depending on the size (height) of the obstacle (stair), the optimal values of parameters s, h, H and n be different.

2.6 Computation of ZMP

To compute the cost function (2.11), the ZMP positions are required at every integration step. Conventional methods [6] of computing ZMP involve computation of system dynamics which is tedious and requires high computational effort. An approximation-based approach of ZMP computation is used in this work which does not require system dynamics.

CM, (x_{cm}, y_{cm}, z_{cm}), of the biped robot is given by,

$$\begin{aligned} x_{cm} &= \frac{\sum_i m_i P_{ix}}{\sum_i m_i}, \\ y_{cm} &= \frac{\sum_i m_i P_{iy}}{\sum_i m_i}, \\ z_{cm} &= \frac{\sum_i m_i P_{iz}}{\sum_i m_i}. \end{aligned} \tag{2.12}$$

The ZMP, $(x_{zmp}, y_{zmp}, 0)$, is related to CM by [10],

$$\begin{aligned} x_{zmp} &= x_{cm} + \frac{\sum_i m_i P_{ix} \ddot{P}_{iz} - \sum_i m_i P_{iz} \ddot{P}_{ix}}{g \sum_i m_i} + \frac{\sum_i M_{iy}}{g \sum_i m_i}, \\ y_{zmp} &= y_{cm} + \frac{\sum_i m_i P_{iy} \ddot{P}_{iz} - \sum_i m_i P_{iz} \ddot{P}_{iy}}{g \sum_i m_i} - \frac{\sum_i M_{ix}}{g \sum_i m_i}, \end{aligned} \tag{2.13}$$

where M_{ix} and M_{iy} are the moments of the links due to rotation about x and y axes respectively. The moments can be computed from the system dynamic equations using Newton-Euler dynamic formulation [4]. In the biped model described in Section 2.1, the masses are concentrated at the link ends making the inertia tensor of the links zero. Due to zero inertia tensor, the moments, M_{ix} and M_{iy}, are zero [4]. ZMP is computed by,

$$\begin{aligned} x_{zmp} &= x_{cm} + \frac{\sum_i m_i P_{ix} \ddot{P}_{iz} - \sum_i m_i P_{iz} \ddot{P}_{ix}}{g \sum_i m_i}, \\ y_{zmp} &= y_{cm} + \frac{\sum_i m_i P_{iy} \ddot{P}_{iz} - \sum_i m_i P_{iz} \ddot{P}_{iy}}{g \sum_i m_i}. \end{aligned} \tag{2.14}$$

Using (2.4), (2.6) and (2.14), it is possible to determine the closed-form expressions of ZMP which is provided in Section 2.6.1. Link masses are approximately 5% to 10% of the actuator masses. Height of hip-link being kept unchanged during walking, the robot has nominal rotational movements. Even when the links have distributed mass (which is not the case in this biped model), numerical values of M_{ix} and M_{iy} are

negligible. However, the third terms in (2.13) are not negligible for fast bipedal activities like running and jumping, or when the link masses and dimensions are comparable to those of the actuators leading to the necessity to compute system dynamics.

2.6.1 ZMP Expression

The following expressions are used in the computation of the biped CM (2.12) [99,101]. Considering the biped' mass distribution (Fig. 2.2) and the reference points (Fig. 2.4), the following expressions are derived.

$$
\begin{aligned}
\textstyle\sum_i \quad & m_i P_{ix} = -(m_2 + 2m_4)x_l + m_1 d_2 cos(\theta_1)cos(\theta_B) \\
+ \quad & m_3 L cos(\theta_1)cos(\theta_B) + m_1(x_r + d_2 cos(\theta_1)cos(\theta_B)) \\
+ \quad & m_3(x_r + L cos(\theta_1)cos(\theta_B)), \\
\textstyle\sum_i \quad & m_i P_{iy} = -m_4 y_l - m_2(\frac{w}{2} + y_l) - m_4(w + y_l) \\
+ \quad & m_1 d_2 sin(\theta_1)sin(\theta_B) + m_3 L sin(\theta_1)sin(\theta_B) \\
- \quad & m_1(d_2 sin(\theta_1)sin(\theta_B) + w) \\
- \quad & m_3(L sin(\theta_1)sin(\theta_B) + w), \\
\textstyle\sum_i \quad & m_i P_{iz} = m_3 L cos(\theta_1)cos(\theta_B) + m_1 d_2 cos(\theta_1)cos(\theta_B) \\
+ \quad & (m_2 + 2m_4)P_{6z} + m_1(z_r - z_l + d_2 cos(\theta_1)cos(\theta_B)) \\
+ \quad & m_3(z_r - z_l + L cos(\theta_1)cos(\theta_B)), \\
\textstyle\sum_i \quad & m_i = 2(m_1 + m_3 + m_4) + m_2.
\end{aligned}
\tag{2.15}
$$

For the computation of the biped's ZMP expression (2.14), the following expressions are used [101],

$$
\begin{aligned}
\textstyle\sum_i \quad & m_i P_{ix} \ddot{P}_{iz} = m_1 P_{3x} \ddot{P}_{3z} + (m_2 + 2m_4) P_{6x} \ddot{P}_{6z} \\
+ \quad & m_1 P_{10x} \ddot{P}_{10z} + m_3 P_{m12x} \ddot{P}_{m12z} + m_3 P_{m0x} \ddot{P}_{m0z}, \\
\textstyle\sum_i \quad & m_i P_{iz} \ddot{P}_{ix} = m_1 P_{3z} \ddot{P}_{3x} + (m_2 + 2m_4) P_{6z} \ddot{P}_{6x} \\
+ \quad & m_1 P_{10z} \ddot{P}_{10x} + m_3 P_{m12z} \ddot{P}_{m12x} + m_3 P_{m0z} \ddot{P}_{m0x}, \\
\textstyle\sum_i \quad & m_i P_{iy} \ddot{P}_{iz} = m_1 P_{3y} \ddot{P}_{3z} + m_4 P_{6y} \ddot{P}_{6z} \\
+ \quad & m_2 (P_{6y} - \frac{w}{2}) \ddot{P}_{6z} + m_4 (P_{6y} - w) \ddot{P}_{6z} \\
+ \quad & m_1 P_{10y} \ddot{P}_{10z} + m_3 P_{m12y} \ddot{P}_{m12z} + m_3 P_{m0y} \ddot{P}_{m0z}, \\
\textstyle\sum_i \quad & m_i P_{iz} \ddot{P}_{iy} = m_1 P_{3z} \ddot{P}_{3y} + (m_2 + 2m_4) P_{6z} \ddot{P}_{6y} \\
+ \quad & m_1 P_{10z} \ddot{P}_{10y} + m_3 P_{m12z} \ddot{P}_{m12y} + m_3 P_{m0z} \ddot{P}_{m0y}.
\end{aligned}
\tag{2.16}
$$

In (2.16), the expressions of $P_6(P_{6x}, P_{6y}, P_{6z})$ are given by (2.6). The expressions of $P_3(P_{3x}, P_{3y}, P_{3z})$, $P_{10}(P_{10x}, P_{10y}, P_{10z})$, $P_{0m}(P_{0mx}, P_{0my}, P_{0mz})$ and $P_{12m}(P_{12mx}, P_{12my}, P_{12mz})$ are computed using (2.4) and (2.6). The expressions of the above reference points are given by (Fig. 2.4),

$$
\begin{aligned}
P_{3x} &= d_2 cos(\theta_B) cos(\theta_1), \\
P_{3y} &= d_2 sin(\theta_B) sin(\theta_1), \\
P_{3z} &= d_2 cos(\theta_1) cos(\theta_2), \\
P_3 &= [P_{3x}, P_{3y}, P_{3z}]^T.
\end{aligned}
\tag{2.17}
$$

$$
\begin{aligned}
P_{10x} &= x_r - x_l + d_2 cos(\theta_D) cos(\theta_{12}), \\
P_{10y} &= d_2 sin(\theta_D) sin(\theta_{12}) - w, \\
P_{10z} &= z_r - z_l + d_2 cos(\theta_{11}) cos(\theta_{12}), \\
P_{10} &= [P_{10x}, P_{10y}, P_{10z}]^T. \qquad (2.18)
\end{aligned}
$$

$$
\begin{aligned}
P_{0mx} &= L cos(\theta_B) cos(\theta_1), \\
P_{0my} &= L sin(\theta_B) sin(\theta_1), \\
P_{0mz} &= L cos(\theta_1) cos(\theta_2), \\
P_{0m} &= [P_{0mx}, P_{0my}, P_{0mz}]^T. \qquad (2.19)
\end{aligned}
$$

$$
\begin{aligned}
P_{12mx} &= x_r - x_l + L cos(\theta_D) cos(\theta_{12}), \\
P_{12my} &= L sin(\theta_D) sin(\theta_{12}) - w, \\
P_{12mz} &= z_r - z_l + L cos(\theta_{11}) cos(\theta_{12}), \\
P_{12m} &= [P_{12mx}, P_{12my}, P_{12mz}]^T. \qquad (2.20)
\end{aligned}
$$

Using (2.15) to (2.20), the closed-form expressions of ZMP are computed with sufficient accuracy without computing system dynamics.

2.7 Simulations and Experiments

The ZMP expressions (2.14) are computed in MATLAB/Simulink environment. These expressions are converted into C language code by using 'ccode'[4] command for faster computation and simulation. Fourth order Runge-Kutta method of numerical integration, with fixed time step of 0.0001 second, is used for GA based optimization. The

[4]'ccode' command converts a MATLAB expression into C language expression.

Table 2.3: Optimum Walking Parameters obtained through GA optimization.

λ	step-length s	maximum frontal-shift n	maximum lifting-height H	bending-height h	f
0.10	0.125	0.128	0.010	0.022	0.944
0.15	0.130	0.109	0.014	0.020	0.965
0.20	0.124	0.130	0.006	0.017	0.926
0.40	0.119	0.108	0.018	0.016	0.903
0.60	0.104	0.112	0.013	0.016	0.857
0.90	0.057	0.127	0.017	0.018	0.939
1.0	0.055	0.120	0.026	0.010	1.000

optimal walking parameters are computed in Microsoft VC++ environment using the C code generated.

The optimal walking parameters are used in MATLAB environment to compute the inverse kinematic solutions for the biped to walk straight and to generate the control instructions for the motors. These instructions are sent to the motors using RS-485 serial communication protocol making the biped walk straight. As the DX-113 motors are capable of communicating with MATLAB, inverse kinematic is solved online and the instructions are sent to the motors.

For computing the cost function f in (2.11), f_1^{max} and f_2^{max} are required. f_1^{max} is found out using GA (discussed in section 2.4) with cost function f_1. f_1^{max} is 442.522 corresponding to the maximum value of cost function f_1. f_2^{max} is obtained biped's mechanical constraints (2.7) and is equal to 0.13.

Several simulations were run to compute the optimal walking parameters for different values of λ (Table 2.7). When the stability margin is less, the nature of walking is more static. Static gaits are slower compared to dynamics gaits. Hence, walking

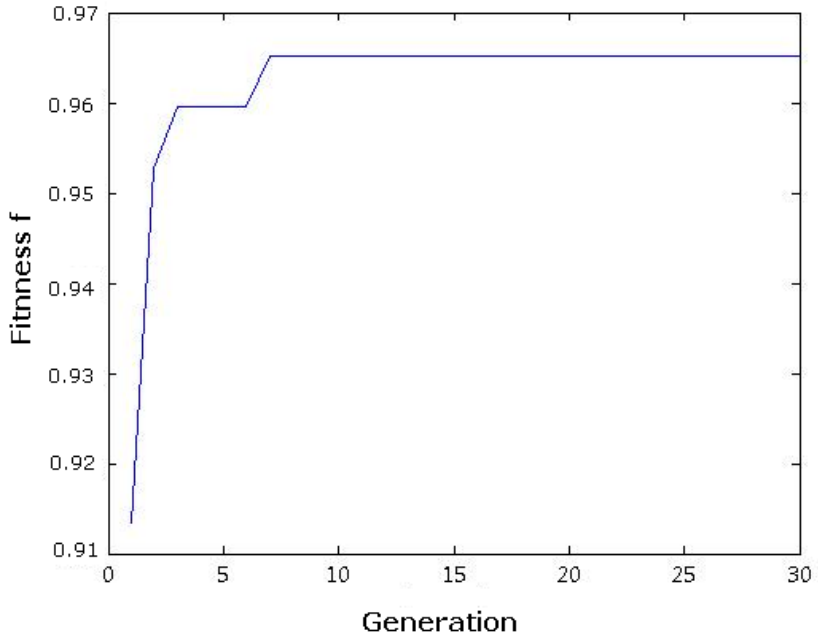

Figure 2.8: Fitness trend with $\lambda = 0.15$.

becomes slower with higher stability margin. Parameters corresponding to $\lambda = 1$ produce gaits with highest stability margin. Experimentally, it is seen that the biped falls down while trying to walk with parameters for $\lambda < 0.1$. Table 2.7 shows the optimum walking parameters for different λ varying from 0.1 to 1.0. Dynamics walking is observed for $\lambda < 0.2$. Walking gaits are realized for λ evenly varying from 0.1 to 0.2. $\lambda = 0.15$ provides satisfactory walking performance on tiled surface. Fig. 2.8 shows the fitness trend in GA based optimization which converges within 15 epoches. Integration time step for evaluating the cost function f in the optimization process is 0.0001 seconds and a single generation corresponds to 300000 time steps. Step-time T is 1 seconds and Δt is 0.1 seconds. In an Intel Pentium IV processor, the overall optimization process takes approximately 10 minutes.

As the inverse kinematic is solved at every sampling instant and the communication between MATLAB and the motors has some time delay, the time for one step of walking ($\sim 1.2 seconds$) is more than the step-time T. The biped's walking gait with $\lambda = 0.15$ is shown in Figs. 2.9 and 2.10 for 10 step-times. The screenshot of the biped walking experiment is shown in Fig 2.11. The walking speed is about 0.125 m/s.

The variation of ZMP for single step-time of walking cycle with $\lambda = 0.15$ is shown in Figs. 2.12 and 2.13. The shaded portions in the figures indicate the single-support phase. The single-support phase is sensed by the current-intake-feedback from the motors. For postural stability of the biped in single-support phase, the ZMP should be within the following ranges (from (2.8)): $-0.03 \leq x_{zmp} \leq 0.07$ and, $-0.0275 \leq y_{zmp} \leq 0.0275$. In Figs. 2.12 and 2.13, it is seen that the above conditions are not satisfied in certain phases of walking cycle. Therefore, the dynamic walking is generated with $\lambda = 0.15$.

2.7.1 Effect of λ on walking performance

During biped walking (static or dynamic) the duration when the biped is not statically stable decides the stability margin. Stability margin varies with λ. With increase in λ the stability margin increases and vice-versa[5]. Stable walking on different surface conditions requires different stability margins. For example, while walking on tiled surface $\lambda = 0.15$ provides satisfactory walking performance. $\lambda = 0.2$ is required for satisfactory walking performance on plywood surface. $\lambda = 0.9$ provides stable walking parameters when wires of thickness 3 $millimeters$ are placed on the walking surface. The value of λ can be adjusted for stable walking depending on the surface condition

[5]With increase in λ in (2.11), more weight is given on stability than speed.

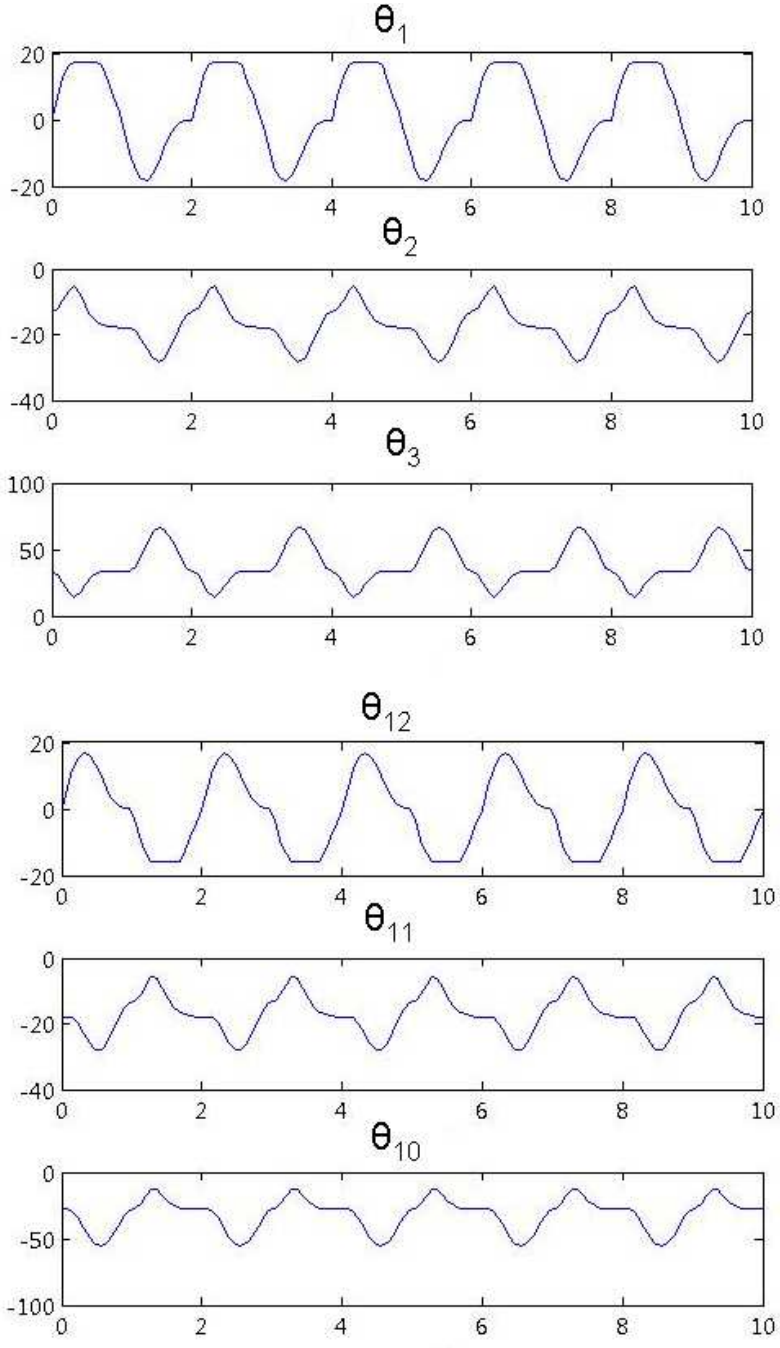

Figure 2.9: The walking gait with $\lambda = 0.15$: θ_1, θ_{12}, θ_2, θ_{11}, θ_3, θ_{10} (time in Second vs. angle in degree).

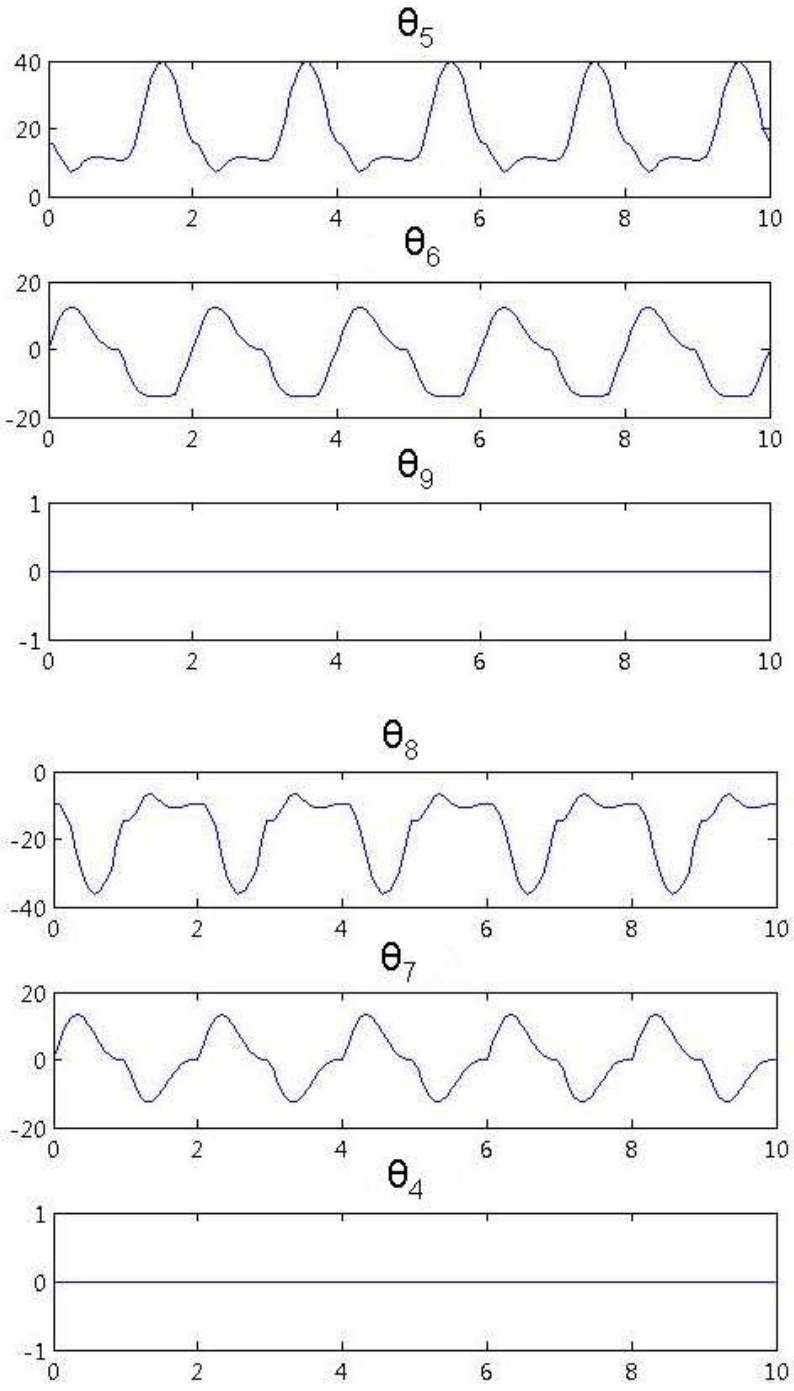

Figure 2.10: The walking gait with $\lambda = 0.15$: θ_4, θ_9, θ_5, θ_8, θ_6, θ_7 (time in Second vs. angle in degree).

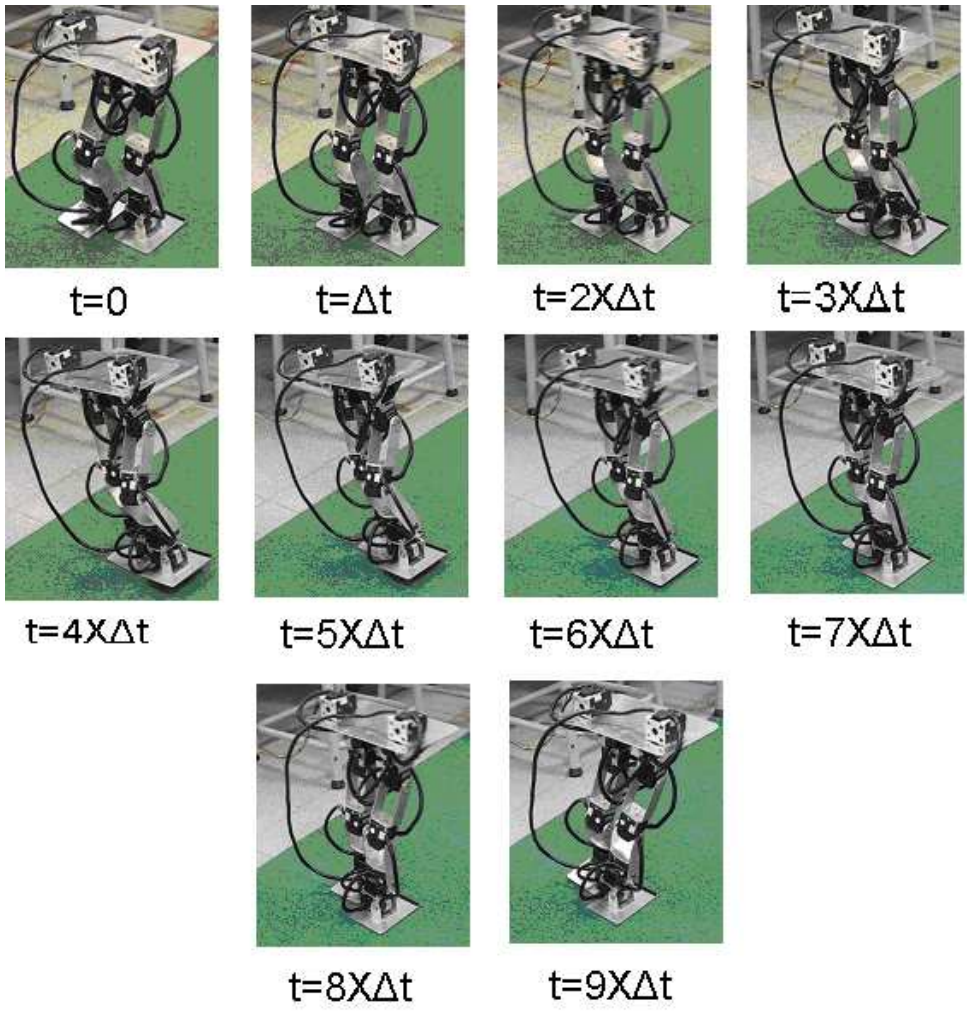

Figure 2.11: Biped walking for one step-time with $\lambda = 0.15$.

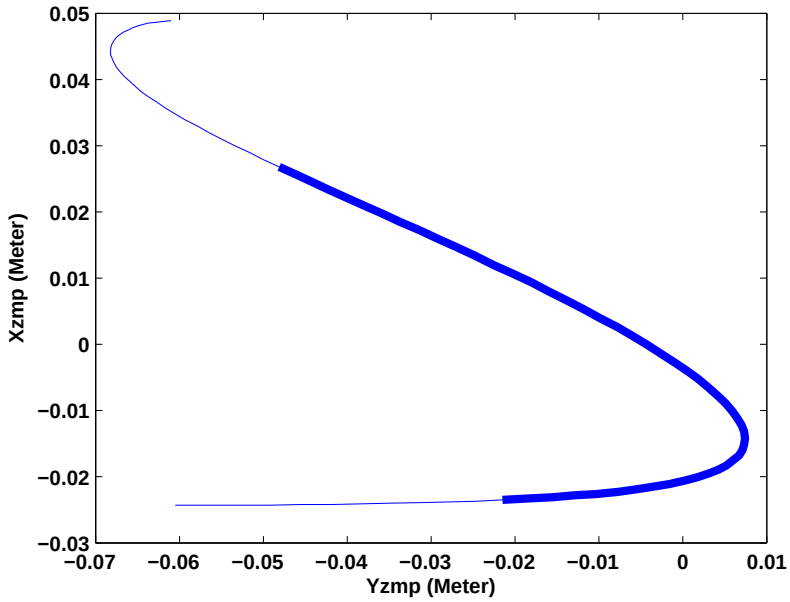

Figure 2.12: y_{zmp} vs. x_{zmp} for one step-time with $\lambda = 0.15, s = 0.13, n = 0.109, H = 0.014, h = 0.020$.

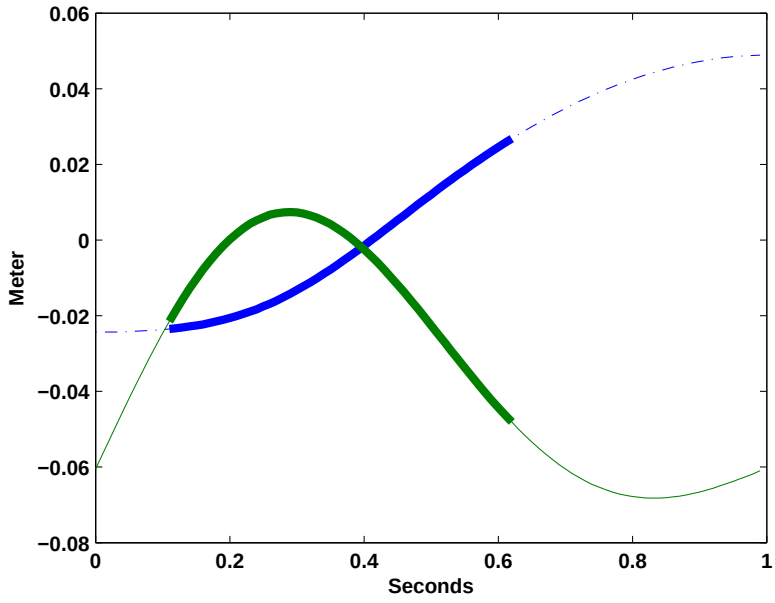

Figure 2.13: y_{zmp} and x_{zmp} vs. time for one step-time with $\lambda = 0.15, s = 0.13, n = 0.109, H = 0.014, h = 0.020$ (dotted line is x_{zmp} and solid line is y_{zmp}).

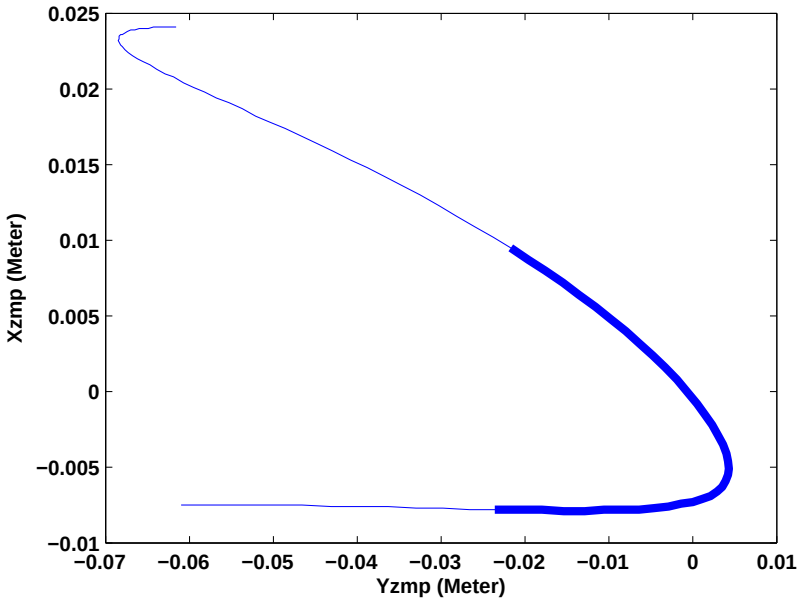

Figure 2.14: y_{zmp} vs. x_{zmp} for one step-time with $\lambda = 1.0, s = 0.055, n = 0.12, H = 0.026, h = 0.010$.

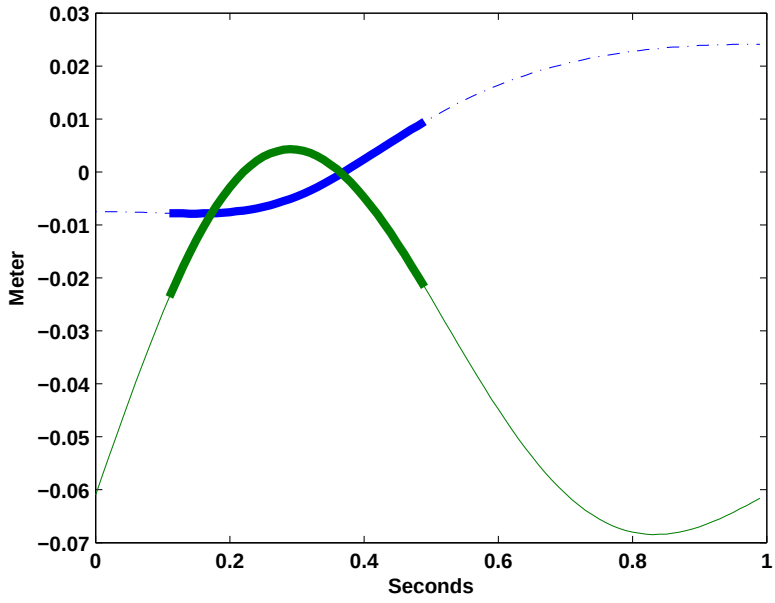

Figure 2.15: y_{zmp} and x_{zmp} vs. time for one step-time with $\lambda = 1.0, s = 0.055, n = 0.12, H = 0.026, h = 0.010$ (dotted line is x_{zmp} and solid line is y_{zmp}).

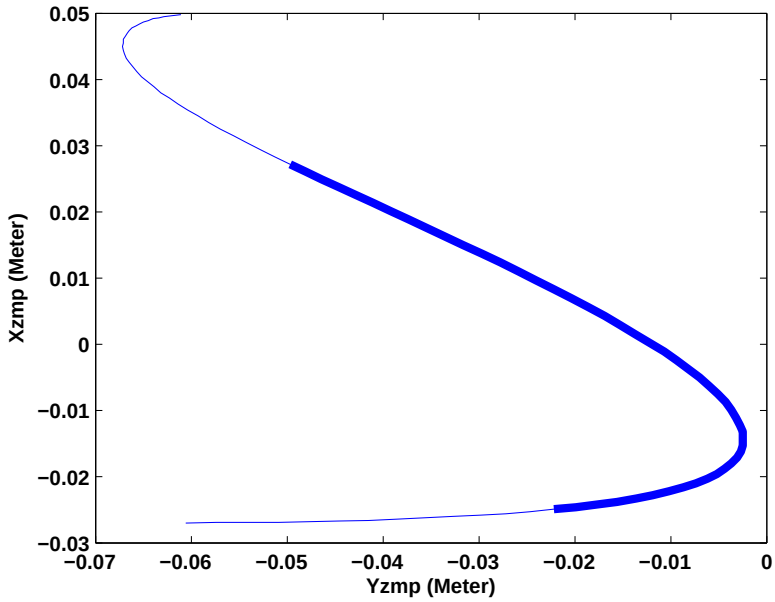

Figure 2.16: y_{zmp} vs. x_{zmp} for one step-time with $\lambda = 1.0, s = 0.125, n = 0.128, H = 0.01, h = 0.022$.

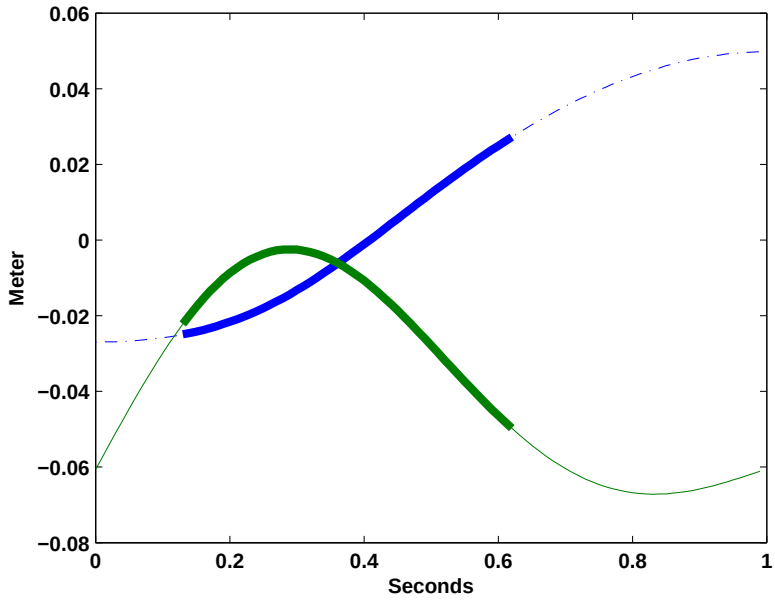

Figure 2.17: y_{zmp} and x_{zmp} vs. time for one step-time with $\lambda = 1.0, s = 0.125, n = 0.128, H = 0.01, h = 0.022$ (dotted line is x_{zmp} and solid line is y_{zmp}).

or disturbances.

The stability margin is maximum with parameters for $\lambda = 1.0$. Figs. 2.14 and 2.15 show the variation of ZMP for one step-time when walking on tiled surface. The ZMP positions meet the conditions for static stability (2.8) for the entire walking cycle. Parameters corresponding to $\lambda = 1$ produce static walking. The static walking speed is $\sim 0.05\ m/s$.

Figs. 2.16 and 2.17 show the variation of ZMP for one step-time when walking on tiled surface with $\lambda = 0.1$. In certain phases of the walking gait, the conditions in (2.8) are not satisfied leading to dynamic walking. With $\lambda = 0.1$, the stability margin is lesser and the walking speed is higher ($\sim 0.128\ m/s$) than those with $\lambda = 0.15$.

2.7.2 Effect of step-time (T) on walking performance

With increasing step-time T, the walking process slows down increasing the stability margin and, both f_1 and f_1^{max} increase. However, $\frac{f_1}{f_1^{max}}$ does not change, keeping the value of f almost unchanged. Table 2.7.2 and 2.7.2 show the optimal walking parameters for $\lambda = 0.1$ and $\lambda = 0.15$ respectively with different values of T. The parameters does not vary much with T. With increase in T and constant Δt, the sampling frequency ($\frac{T}{\Delta t}$) increases. Sampling frequency decreases when T decreases with constant Δt. If ($\frac{T}{\Delta t}$) is constant, the value of T does not have any effect on walking performance. Although, ($\frac{T}{\Delta t}$) can be changed to adjust the walking speed, it is recommended to vary λ or step-length 's' adjusted the walking speed.

Table 2.4: Walking Parameters for different step-time (T) with $\lambda = 0.1$.

T	s	n	H	h	f_1^{max}	f
2.0	0.119	0.12	0.01	0.0215	1258.90	0.9396
1.5	0.12	0.125	0.01	0.02120	979.51	0.9412
0.8	0.125	0.119	0.01	0.0210	382.66	0.9485
0.5	0.121	0.128	0.01	0.0220	202.87	0.9445

Table 2.5: Walking Parameters for different step-time (T) with $\lambda = 0.15$.

T	s	n	H	h	f_1^{max}	f
2.0	0.126	0.12	0.014	0.0215	1258.90	0.9596
1.5	0.130	0.11	0.014	0.0220	979.51	0.9612
0.8	0.130	0.12	0.014	0.0200	382.66	0.9585
0.5	0.129	0.11	0.014	0.0210	202.87	0.9645

2.8 Conclusions

In this work, the walking gait generation of a twelve DOF biped robot is considered. Closed-form solution of the inverse kinematics of the biped is computed. The inverse kinematics is expressed in terms of certain gait parameters. The walking gait is generated based on the parameters. The walking gait is parameterized in terms of four factors i.e. Step length, Bending-height, Maximum Lifting-height and Maximum Frontal-shifting. These walking parameters are then optimized using GA. The optimization is performed as a tradeoff between postural stability and walking speed. The optimal gaits are experimentally realized on a biped robot.

Chapter 3

Disturbance Rejection by Online ZMP Compensation

Humans have always been fascinated by humanoid robots - robots that look and function like humans. A particular area of research interest currently being pursued actively in humanoid robotics is the control of biped locomotion.

Based on the ZMP criterion, various algorithms of trajectory planning have been suggested. Most of these algorithms involve the calculation of the desired joint trajectories via inverse kinematics to satisfy the ZMP criterion and the calculation of various joint torques needed. One such approach is to specify a desired hip trajectory while satisfying the ZMP criterion [21, 67]. Successful examples of such techniques include Manus-I [68] and the Honda Asimo Robot [22].

ZMP compensation is an approach to alter joint trajectories or joint torques to enable the robot to react to the disturbances from the environment by keeping the ZMP within the support polygon. In Kim's [67] work, a constant compensation procedure is discussed. The reference angles to the ankle roll and pitch joints are changed by a constant amount when the ZMP moves out of an area in the support polygon. In Honda Robot [22], ZMP compensation is done by revising the prescribed ZMP

during walking when there is deviation from the desired ZMP. The problem of walking on uneven terrain is addressed in this work. In [59], a stable walking pattern generation problem is addressed by ZMP compensation. The ZMP compensation is done by the trunk motion while walking on a flat surface. In [20], ZMP compensation is done by whole-body-motion control for stable walking pattern generation. In Mitobe's [69] work, the ground reaction forces and cartesian coordinates of the robot is measured and fed back to control the position of the robot by manipulating the position of the ZMP. The control mechanism involves very precise control of the joint-angular position of the robot which needs high-gain-feedback. In this work, mainly the smoothness of the walking gait of the robot is considered. Kajita el al. [14] introduced preview control where ZMP compensation problem is addressed as a servo problem. The effectiveness of the method is verified in simulation while the robot is walking on a spiral path. In [70] simulation study of ZMP compensation by modifying the trajectories of the different joints is done for walking on a flat surface.

The physical implementation of a trajectory-based compensation technique is examined on Manus-I [68] in this work[1]. Manus-I has 12 degrees of freedom in the lower body and each joint is driven by an Radio-Controlled servo motor [74]. A Digital Signal Processor (DSP) (Motorola 56F807) controls walking motion of the robot by sending the desired joint trajectory signals to various leg joint motors. The ZMP at each instant is measured using force sensors located at the corners of each foot bottom. The DSP controller receives and processes the data from the force sensors. Compensation for the ankle reference angles is calculated according to the deviation

[1]The work is published and details of the publication are "Prahlad Vadakkepat, Dip Goswami and Chia Meng Hwee, *Disturbance Rejection by Online ZMP Compensation*, Robotica, vol. 26, pp. 9-17, 2007."

of the ZMP.

The biped model, the force sensors and the method to measure ZMP are discussed in section 3.1. The online ZMP compensation technique for disturbance rejection is discussed in section 3.2. The compensation technique is used for the stabilization of the biped locomotion while walking on a flat terrain, walking up/down the slope, carrying weight and experiencing sudden push from front or back. Section 3.3 discusses about the four different applications of the compensation method in biped locomotion. The chapter is concluded in section 3.4.

3.1 ZMP Measurement

3.1.1 Biped Model

The biped model, considered in this work, has six DOF in each leg: two DOF at the ankle, one at the knee and three at the hip. The biped model has the mass distribution as shown in Fig. 3.1. The masses of the links are considered as point-mass because the links are made of very light-weight material with motor-weight being the dominant part. The mass of the upper body is also considered as point-mass and taken into account by the mass m_2. The values of the parameters of the robot-model (Fig. 3.1) are shown in Table 3.1.1. The model of the bipedal lower part of the Humanoid MaNUS-I is developed in visualNastran 4D simulation environment (Fig. 3.2). The real robot is shown in Fig. 3.3.

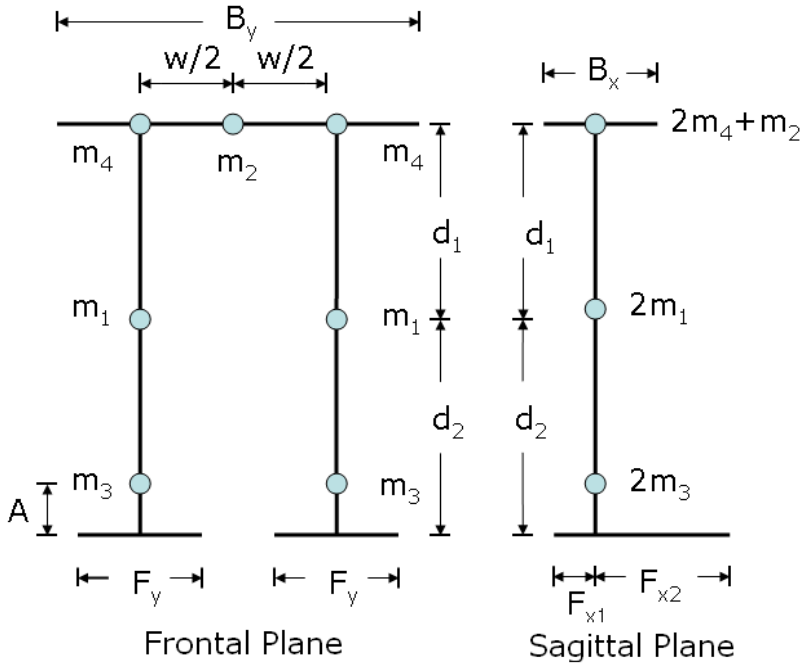

Figure 3.1: Biped Model in the frontal and sagittal plane.

3.1.2 Force Sensors

Tekscan FlexiForce force sensors are used to measure the forces acting on the feet of the robot. An illustration of the mechanical installation of the force sensors is provided in Fig. 3.4.

The electrical resistance of the force sensors (R_F) are inversely proportional to the magnitude of the normal force acting on the force sensors. A simple electrical circuit (Fig. 3.5) converts the force measured into voltage by (3.1) [73],

$$\begin{aligned} R_F &= \frac{\vartheta}{Force}, \\ V_{adc} &= (\frac{390K\Omega}{R_F + 390K\Omega}) \times V_{ref}, \end{aligned} \tag{3.1}$$

Table 3.1: Parameters of the Biped-Model (MaNUS-I)

Parameters	Values
m_1	0.07 Kg
m_2	1.52 Kg
m_3	0.14 Kg
m_4	0.21 Kg
d_1	0.15 meter
d_2	0.12 meter
w	0.06 meter
A	0.002 meter
B_x	0.1 meter
B_y	0.14 meter
F_{x1}	0.045 meter
F_{x2}	0.08 meter
F_y	0.055 meter

where ϑ is the calibration constant, $V_{ref} = 5$ V and V_{adc} is the voltage measured by the analog-to-digital converter of the DSP.

The positions of the force sensors at the bottom of the feet of the robot, are illustrated in Figs. 3.6 and 3.7. f_i's and P_i's represent respectively the readings and positions of the eight force sensors.

3.1.3 Measurement of ZMP

The center-of-pressure (CP) is defined as the point on the ground where the resultant of the ground-reaction force acts. When the ZMP is within the support polygon, the CP coincides with ZMP [6]. Therefore, the measurement of ZMP is dependent on how the foot contact points are modelled. The pressure, sensed by the ZMP sensor, is distributed over the contact points. In [71], a ZMP sensor is devised which models the contact between the biped's feet and the ground as a collection of infinite points.

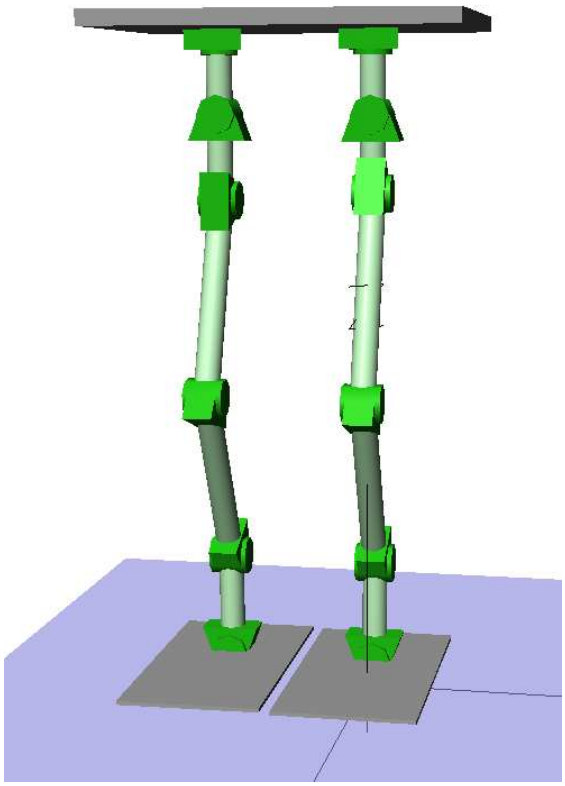

Figure 3.2: Biped Model of MaNUS-I in visualNastran 4D environment.

The force, sensed at each contact point, is measured by a voltage generated by an equivalent electrical circuit.

In our work, the contact points are four force sensors are placed at the four corner of the foot (Fig. 3.6). The principle of ZMP computation utilizes the method described in [71]. This makes the computational and implementation effort considerably less without compromising much in accuracy.

During walking, when one leg is swinging, the mass of the whole body can be replaced by the total mass of the robot located at the center of mass (CM) of the robot as point-mass and is connected to the stance foot like an inverted pendulum.

Figure 3.3: MaNUS-I.

The simplified model shown in Fig. 3.8 is used to approximate the biped model in the rest of the chapter. In Fig. 3.8, 'c' is the CM of the robot with one leg swinging and 'a' is the ankle-joint of the other leg which is on the ground. x_i and y_i $(i = 1, 2)$ are the positions of the force sensors in x and y directions, in sagittal and frontal plane respectively. 'l' is the distance of the CM from ankle-joint in sagittal plane. L is the distance of ZMP from the ankle joint. 'l' can be considered as a link with concentrated point-mass at the end. ϕ is the angle between the link and the z-axis. α is the angle between L and the z-axis. τ is the torque at the ankle-joint about y-axis.

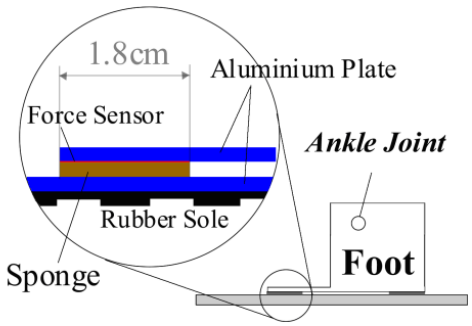

Figure 3.4: Mechanical Installation of Force Sensors.

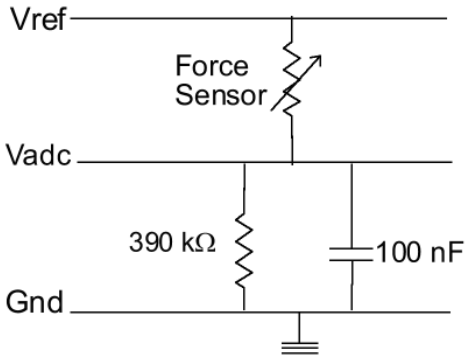

Figure 3.5: Force-to-Voltage Converter Circuit.

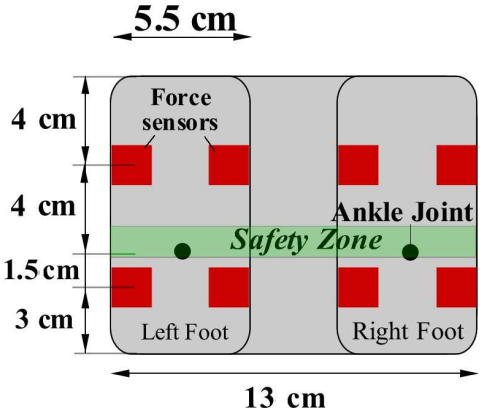

Figure 3.6: Positions of the foot sensors at the bottom of the feet.

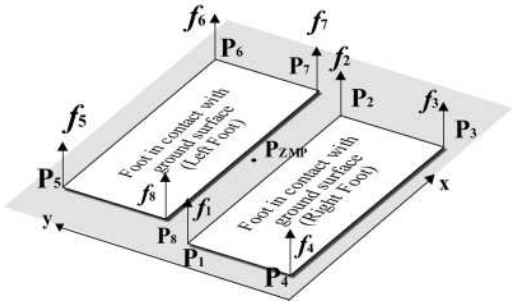

Figure 3.7: Reading of the Force Sensors.

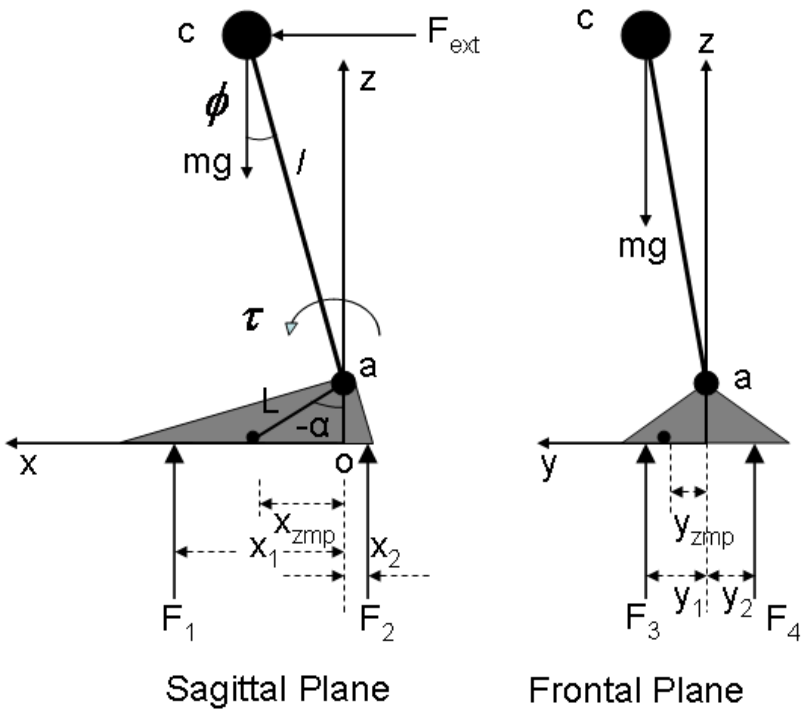

Figure 3.8: Simplified model of the Biped in Sagittal and Frontal Planes.

F_{ext} is the disturbance force applied to the robot as disturbance. 'm' is the total mass of the robot and 'g' is the gravitational acceleration.

The motions in the sagittal and frontal planes are considered separately because the motions in these two planes are weakly coupled [72]. The ZMP in x-direction is calculated from the motion in sagittal plane by (3.2),

$$\begin{aligned} F_1(x_1 - x_{zmp}) - F_2(x_2 + x_{zmp}) = 0 \\ \implies x_{zmp} = \frac{F_1 x_1 - F_2 x_2}{F_1 + F_2}, \end{aligned} \tag{3.2}$$

where $F_1 = f_2 + f_3$ or $F_1 = f_6 + f_7$ and $F_2 = f_1 + f_4$ or $F_2 = f_5 + f_8$, when the right

leg or the left leg is on the ground. $x_1 = 4$ cm, $x_2 = 1.5$ cm (Figs. 3.6 and 3.7). The ZMP in y-direction is calculated from the motion in frontal plane by (3.3),

$$\begin{aligned} F_3(y_1 - y_{zmp}) - F_4(y_2 + y_{zmp}) &= 0 \\ \implies y_{zmp} &= \frac{F_3 y_1 - F_4 y_2}{F_3 + F_4}, \end{aligned} \tag{3.3}$$

where $F_3 = f_1 + f_2$ or $F_3 = f_5 + f_6$ and $F_4 = f_3 + f_4$ or $F_4 = f_7 + f_8$, when the right leg or the left leg is on the ground. $y_1 = y_2 = 2.75$ cm (Figs. 3.6 and 3.7).

3.2 Online ZMP Compensation

The compensation technique proposed in this work mainly focuses on the sagittal plane motion. The method can also be extended for the frontal plane motion. Without loss of generality, the compensation is done based on the following assumptions:

A1 The motion of the biped is confined to the sagittal plane.

A2 It is assumed that the compensation torque $\Delta\tau$ causes change in acceleration of the compensating link, $\Delta\ddot{\phi}$, while link-velocities do not change due to the action of $\Delta\tau$, $\Delta\dot{\phi} \approx 0$. The physical significance of this assumption is that biped's movements are slow enough to neglect effects of the coriolis ($\dot{\phi}\Delta\dot{\phi}$) and the centrifugal ($(\Delta\dot{\phi})^2$) forces.

A3 It is assumed that when the biped is on the move, the ZMP is always within the support polygon. This assumption ensures that during walking, when one leg is swinging, the other foot is in contact with the ground without any foot

rotation[2].

A4 It is assumed that the value of 'l' is constant and almost equal to the height of the CM during walking, as x and y components of the CM are much less compared to the z-component of the CM which comes to $l \approx 0.1$ m for MaNUS-I.

A5 $\mid \frac{L}{l} cos(\phi+\alpha) \mid \ll 1$ in (3.10). As the height of the ankle-joint is smaller compared to the height of CM, $0 < \frac{L}{l} < 1$ and $\mid cos(\phi+\alpha) \mid < 1$. When $0 < \frac{L}{l} \ll 1$, i.e. x_{zmp} is close to the ankle-joint, $\mid \frac{L}{l} cos(\phi+\alpha) \mid \ll 1$. When the value of $\frac{L}{l}$ is relatively high i.e. x_{zmp} is far from the ankle-joint, α is larger which means $cos(\phi+\alpha)$ is small leading to $\mid \frac{L}{l} cos(\phi+\alpha) \mid \ll 1$.

A6 The amount of disturbance, which is rejected, is restricted by the torque rating of the motor. It is assumed that the disturbances vary gradually and that the torque requirement at the ankle actuator does not exceed the torque-rating of the ankle actuators.

A7 A 'safety zone', closer to the ankle-joint, is defined in a range of 0.25 to 0.5 of the normalized foot-length. If the x-ZMP is within the 'safety zone', it is assumed that no disturbance is acting on the robot.

A8 When the x-ZMP value is beyond the 'safety zone', it is assumed that disturbance is acting on the robot. The disturbance can be both due to the external forces and due to the shifting of robot's weight during walking.

When the x-ZMP is located within the 'safety zone', no compensation is provided. When the x-ZMP falls (due to external disturbance or robot's weight shifting) beyond

[2]The concepts such as ZMP and FRI are not applicable if the foot is rotated. Bipedal stability with foot rotation is discussed in chapter 5.

the 'safety zone' compensation is activated. Let, at the $(k-1)^{th}$ sampling interval, the x-ZMP position is x_{zmp}. The moment about x_{zmp} during $(k-1)^{th}$ sampling interval is given by,

$$M_{zmp}^{k-1} = F_1(x_1 - x_{zmp}) - F_2(x_2 + x_{zmp}) = 0. \tag{3.4}$$

When a disturbance force (F_{ext}) is acting on the robot in x-direction, at k^{th} sampling interval the moment about x_{zmp} is computed using (3.2) and (3.4)[3],

$$\begin{aligned} M_{zmp}^{k} &= (F_1 + \Delta F_1)(x_1 - x_{zmp}) - (F_2 + \Delta F_2)(x_2 + x_{zmp}) \\ &= \Delta F_1(x_1 - x_{zmp}) - \Delta F_2(x_2 + x_{zmp}) \\ &= \Delta F_1 x_1 - \Delta F_2 x_2 - (\Delta F_1 + \Delta F_2)x_{zmp} \\ &= \Delta F_1 x_1 - \Delta F_2 x_2 - \frac{(\Delta F_1 + \Delta F_2)}{F_1 + F_2}(F_1 x_1 - F_2 x_2). \end{aligned} \tag{3.5}$$

The values of ΔF_1 and ΔF_2 are measured from the changes in the force sensor reading between successive sampling intervals. Therefore, M_{zmp}^{k} is measurable. The system is equivalent to a two-link planner manipulator with joints located at x_{zmp} and the ankle-joint 'a'. The length of the two links are 'L' and 'l'. The torques τ and M_{zmp}^{k} are acting at the two joints which are located at x_{zmp} and 'a' respectively (Fig. 3.8).

Dynamics of the above two-link robotic system is computed by the Lagrangian formulation [6]. Without compensation, the ankle-joint torques τ and M_{zmp}^{k} are given by[4],

$$\begin{aligned} \tau &= J\ddot{\phi} + mlgsin(\phi) + F_{ext}lcos(\phi), \\ M_{zmp}^{k} &= (J + mlLcos(\phi + \alpha))\ddot{\phi} + mlgcos(\phi) + mLgsin(\alpha), \end{aligned} \tag{3.6}$$

[3]Without compensation.

[4]Derivation is available in Chapter 3 in [6].

where 'J' is the moment of inertia of the robot about y-axis of the ankle-joint i.e. $J = ml^2$. If there is no compensation provided, the ZMP will shift. The shift in ZMP value can be calculated from the force sensor readings as discussed in Section 3.1.3. Without compensation, the x-ZMP value shifts by an amount,

$$\Delta x_{zmp} = \frac{M^k_{zmp}}{F_1 + F_2 + \Delta F_1 + \Delta F_2}. \tag{3.7}$$

The compensation acts only if $(x_{zmp} + \Delta x_{zmp})$ goes beyond the designated 'safety zone'. Let, $\Delta\tau$ is the compensation torque applied at the ankle-joint during k^{th} sampling interval which makes the moment about x_{zmp} zero. The system is equivalent to a two-link planner manipulator with a zero torque at x_{zmp} and $(\tau + \Delta\tau)$ acting at ankle-joint 'a'. With the assumption A2, the system dynamics is given by,

$$\begin{aligned} \tau + \Delta\tau &= J(\ddot{\phi} + \Delta\ddot{\phi}) + mlgsin(\phi) + F_{ext}lcos(\phi), \\ 0 &= (J + mlLcos(\phi + \alpha))(\ddot{\phi} + \Delta\ddot{\phi}) + mlgcos(\phi) + mLgsin(\alpha). \end{aligned} \tag{3.8}$$

Therefore, the compensation torque $\Delta\tau$ is computed from (3.6) and (3.8),

$$\begin{aligned} \frac{\Delta\tau}{M^k_{zmp}} &= -\frac{J}{J + m \cdot l \cdot Lcos(\phi + \alpha)} \\ \implies \Delta\tau &= -\frac{M^k_{zmp}}{1 + \frac{m \cdot l \cdot Lcos(\phi+\alpha)}{J}}. \end{aligned} \tag{3.9}$$

Considering the assumption A5, it is claimed that,

$$\begin{aligned} \Delta\tau &= -\frac{M^k_{zmp}}{1 + \frac{m \cdot l \cdot Lcos(\phi+\alpha)}{ml^2}} \\ &= -\frac{M^k_{zmp}}{1 + \frac{L}{l}cos(\phi + \alpha)} \\ \implies \Delta\tau &\approx -M^k_{zmp}. \end{aligned} \tag{3.10}$$

Thus, the compensation torque $\Delta\tau$, which is required at the ankle-pitch joint, is computed from the force sensor readings. The required torque is provided by the proper adjustment of ϕ by changing the ankle-pitch-joint angular position, using (3.6) and (3.8).

$$\begin{aligned} \Delta\tau &= -M^k_{zmp} = J\Delta\ddot{\phi} = J\frac{\Delta\phi}{(\Delta t)^2} = \eta\Delta\phi, \\ \Delta\phi &= \frac{-M^k_{zmp}}{\eta}, \end{aligned} \tag{3.11}$$

where Δt is the sampling interval of the DSP controller and $\eta = \frac{J}{(\Delta t)^2}$ is a constant. $\Delta t = 12.5$ ms for the DSP controller used in this work. The total mass of the whole robot is $m = 2(m_3 + m_1 + m_4) + m_2 = 2.36$ kg. The numerical values of 'J' and η, for MaNUS-I, are given by[5],

$$\begin{aligned} J &= ml^2 = 0.0236\ kg\text{-}m^2, \\ \eta &= \frac{J}{(\Delta t)^2} = 151.04. \end{aligned} \tag{3.12}$$

The compensation at the ankle-joint's reference angle for disturbance rejection is computed by (3.11) and (3.12). Similarly, compensation is possible for the disturbances in other forms or directions.

The disturbances are compensated by changing the reference angle of the ankle-pitch-joint. The overall block diagram of the ZMP compensation technique is shown in Fig. 3.9. In Fig. 3.9, ϕ is the reference position of the ankle-pitch-joint without compensation. The reference value of the ankle-pitch-joint servo controller is changed by $\Delta\phi$ amount for disturbance rejection. From the above analysis, it is seen that,

- The proposed ZMP compensation technique is applicable to any bipedal system as long as the system closely follows the assumptions A1-A8.

[5] m=2.36 kg and l=0.1 m.

- The proposed ZMP compensation technique does not require exact disturbance modeling.
- The torque-rating of the ankle-joint motors decides the maximum amount of disturbance that can be compensated by the above technique. The higher the ankle-joint motor torque-rating is, higher the ability to reject disturbances.

In order to evaluate the effectiveness of the compensation technique, it is applied to MaNUS-I for disturbance compensation in different applications.

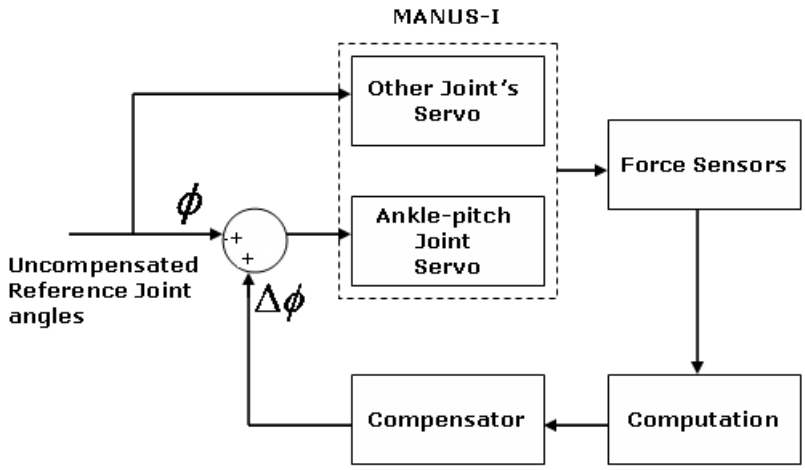

Figure 3.9: The block diagram for online ZMP compensation.

3.3 Applications, Experiments and Results

Experimentations were performed on the robot - MaNUS-I. The robot was developed in Mechatronics and Automation Laboratory, Electrical and Computer Engg dept,

National University of Singapore in 2001. MaNUS-I is the overall humanoid champion at FIRA Roboworld Cup (www.fira.net) competition in the years 2003, 2005 and 2006. It has won first runner up in FIRA Roboworld Cup competition 2004.

3.3.1 Improvement of Walking on Flat Surface

The x-ZMP positions of the MaNUS-I robot are computed from the force measurements while walking on a flat surface using (3.2). The x-ZMP value is normalized to the length between the front and back force sensors. The compensation technique comes into play whenever the x-ZMP position goes beyond the 'safety zone'. The compensation angle at the ankle-joint is calculated using (3.5), (3.11) and (3.12). The robot is made to walk on a flat surface without compensation and with compensation over a period of 20 seconds. Figs. 3.10 and 3.11 show the recorded x-ZMP positions once the walking gait is stabilized starting from a standing position. Fig. 3.12 shows the amount of compensation required at the ankle-pitch-joint to keep the x-ZMP position within the 'safety zone'. It is clear from the results that the compensator is able to reduce the magnitude of fluctuation of the ZMP keeping its value within the 'safety zone'.

3.3.2 Rejecting Disturbance due to Sudden Push

With the compensation at place, the robot's walking gait is robust to sudden disturbances such as a slight push from behind or from the front. When the robot experiences a push, the ZMP shifts momentarily out of the expected position and goes beyond the 'safety zone'. By ankle-joint-compensation the robot is able to revert back the x-ZMP position within the 'safety zone' after certain walking cycles

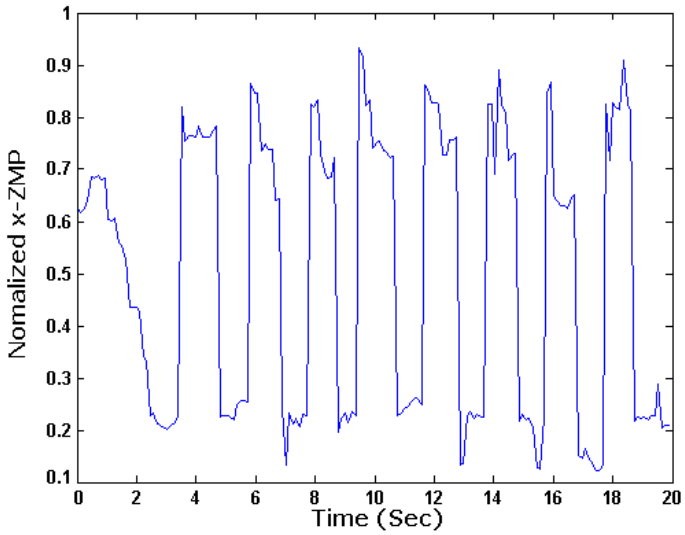

Figure 3.10: Normalized x-ZMP Position of Uncompensated Walking Gait.

depending on the amount of the disturbance.

The robot MaNUS-I was kept in standing posture and it is pushed from backside or front side. In order to provide a measure of the horizontal disturbance force that the robot can reject, force sensors are attached at the front and back of the robot body, 40 cm from the ground (Fig. 3.13) while the total height of the robot is 50 cm. The force, which is applied to the robot, is measured using an oscilloscope by recording the V_{adc} of the Force-to-Voltage converter circuit (Fig. 3.5). A short impulse of force is applied to the force sensor over a time period of about 0.5 seconds in order to measure the maximum force that the robot is able to withstand without falling down. A typical oscilloscope display of the force is shown in Fig. 3.14. Fig. 3.15 shows the normalized x-ZMP position of the robot when it experiences a sudden

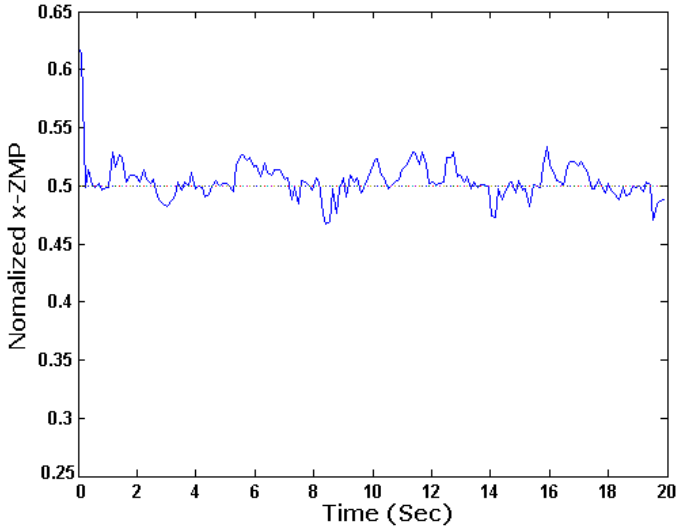

Figure 3.11: Normalized x-ZMP Position of Compensated Walking Gait.

push of intensity around 3 N from behind. The compensation required at the ankle-pitch-joint for rejecting the above disturbance is shown in Fig. 3.16.

The amount of maximum disturbance which can be rejected is dependent on the torque-rating of the ankle-pitch-joint actuator. MaNUS-I uses radio-controlled servo motor with a torque rating 0.13 Nm at the ankle-joints. The maximum forward force (from behind) that the robot can reject is around 3 Newton while it is able to reject a maximum backward force of about 1.2 N. The walking sequences of the robot with backward and forward disturbances are shown in Figs. 3.17 and 3.18 respectively.

3.3.3 Walking Up and Down a Slope

While the robot walks down/up the slope, the biped's x-ZMP moves out of the 'safety zone'. In order to bring back back the x-ZMP within the 'safety zone', compensation

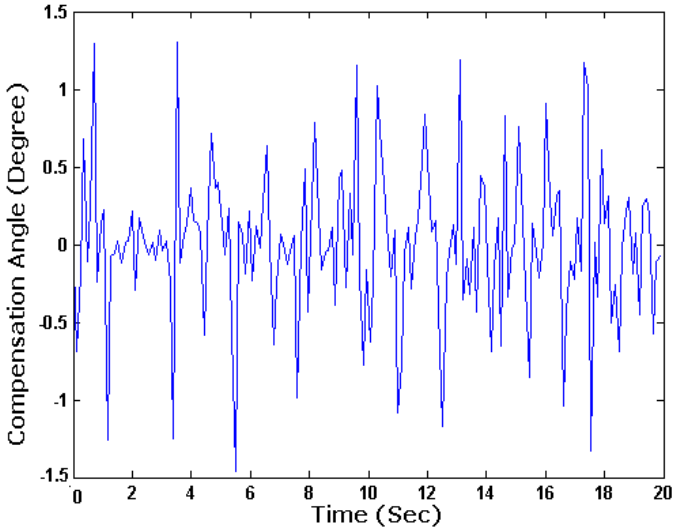

Figure 3.12: Compensation at the ankle-joint during walking on a flat surface.

is provided at the ankle-joint.

While walking up/down the slope, the compensation angle varies with inclination of the slope. As the compensation angle is changing slowly, the robot adapts to a change in inclination successfully only after about 1 to 2 seconds depending on the angle of inclination. Due to limitation in ankle-pitch-joint actuator torque-rating, robot is able to walk up a maximum slope of 10^o and walk down a maximum slope of 3^o on a wooden plank. Figs. 3.19 and 3.20 show the humanoid, MaNUS-I, walking up and down the slope.

3.3.4 Carrying Weight during Walking

For walking with additional weight, a basket is attached on the back of Manus-I (Fig. 3.21). Due to additional weight at the back, biped's x-ZMP moves beyond

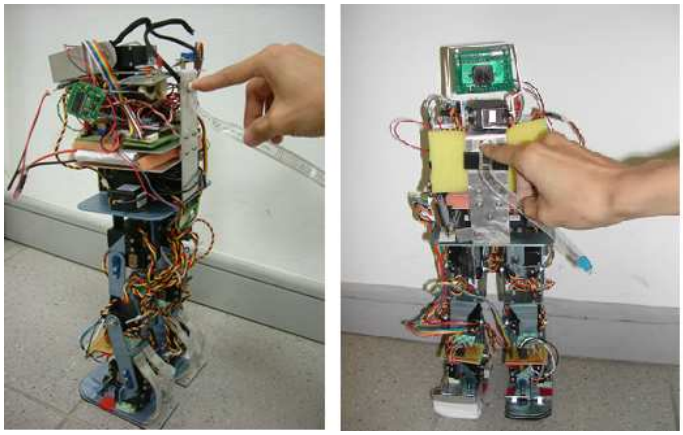

Figure 3.13: Measurement of Disturbance Force.

'safety zone'. After the compensation technique is applied, the x-ZMP moves into the 'safety zone' and the robot is able to carry a maximum of 26 batteries including a metal basket with a total weight of 390 gm and continue walking on a flat surface. The mass of the robot being 2.36 kg, the additional weight is approximately 17% of the robot's weight.

Fig. 3.22 shows the normalized x-ZMP position of the robot while carrying an additional weight of 300 gm at the back for 20 seconds. The compensation required at the ankle-pitch-joint during this period is shown in Fig. 3.23. As the constant additional weight causes the ZMP to shift, the compensation method adjusts the ankle-pitch-angle gradually until the ZMP moves within the 'safety Zone'.

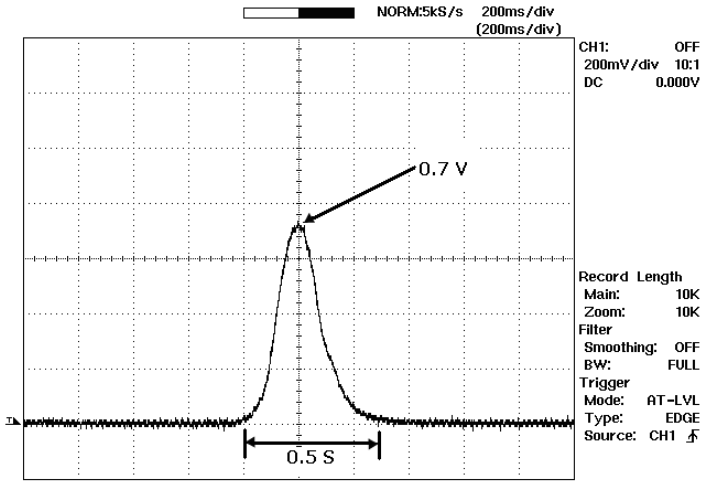

Figure 3.14: Oscilloscope display of the applied force.

3.4 Conclusions

A practical online ZMP compensation technique to reject disturbance for improved biped locomotion, is proposed and experimentally verified. The proposed compensation method is used in four applications to show its applicability in biped-locomotion-stability improvement and disturbance rejection. In comparison with the existing ZMP compensation methods, the proposed approach is easier to implement as it provides compensation to the ankle reference angles instead of changing the desired torque directly. Further investigation is required to provide a more robust performance for such approach in ZMP compensation.

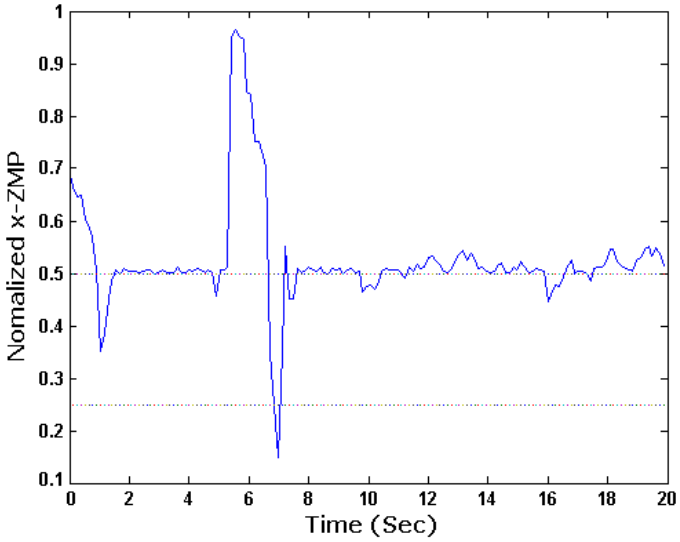

Figure 3.15: Normalized x-ZMP Position of MaNUS-I when it experience a sudden push of intensity around 3 N from behind.

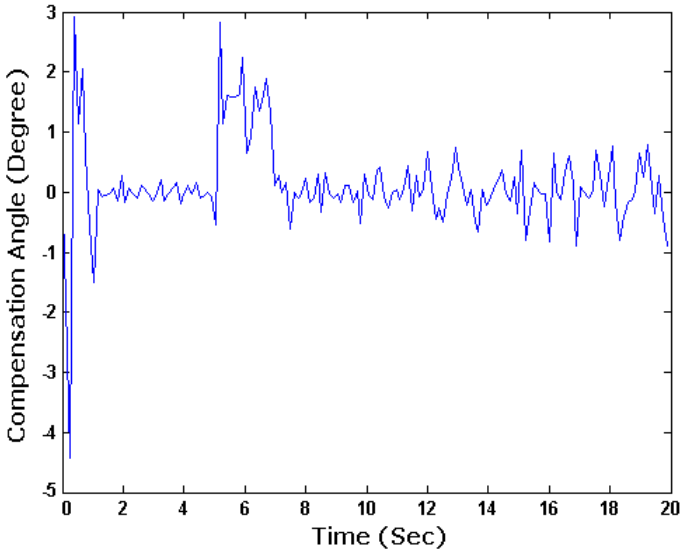

Figure 3.16: Compensation at the ankle-joint of MaNUS-I to compensate a sudden push of intensity around 3 N from behind.

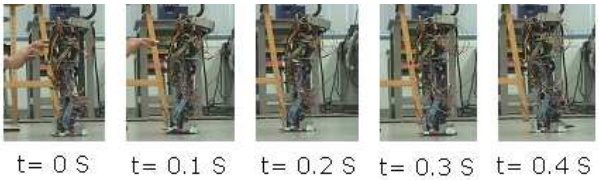

Figure 3.17: Robot walking sequence when pushed from behind.

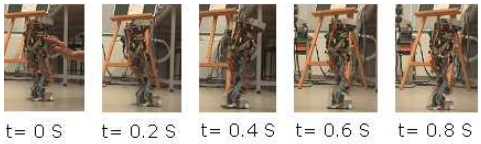

Figure 3.18: Robot walking sequence when pushed from the front.

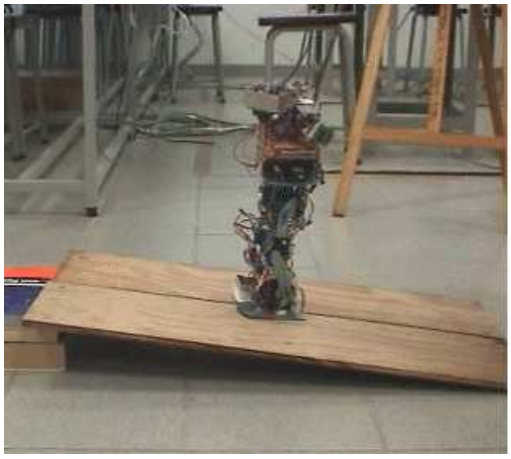

Figure 3.19: Walking up a 10^o slope.

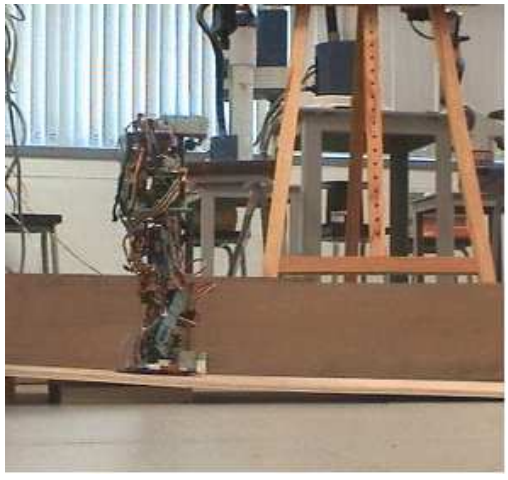

Figure 3.20: Walking down a 3^o slope.

Figure 3.21: Manus-I carrying Additional Weight.

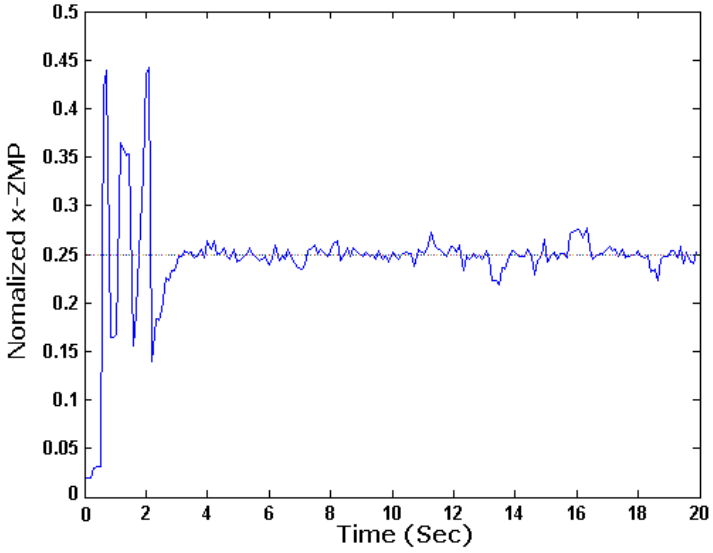

Figure 3.22: Normalized x-ZMP Position of Compensated Walking Gait while carrying 300 gm weight.

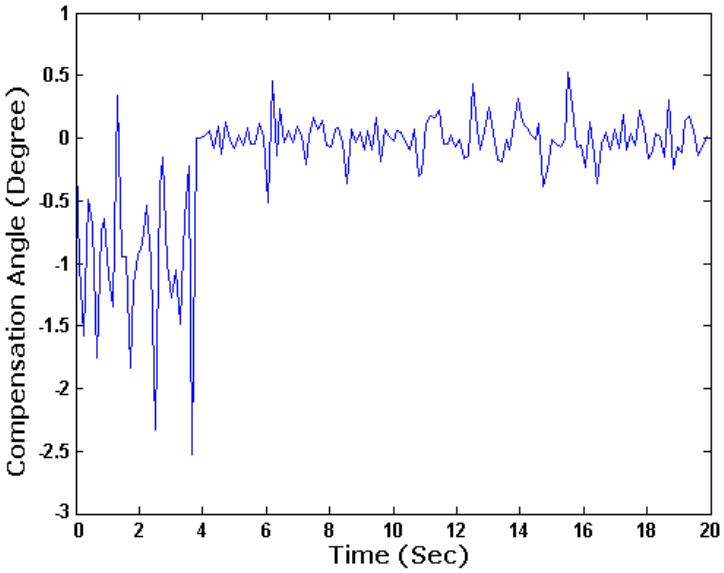

Figure 3.23: Compensation at the ankle-joint while carrying 300 gm weight.

Chapter 4

Jumping Gaits of Planar Bipedal Robot with Stable Landing

Flat-foot biped locomotion is considered while utilizing the ZMP-based stability criterion [16, 99]. Unbalanced moments at the foot leads to foot-rotation about a point on the foot boundary. The occurrence of foot-rotation changes the absolute orientation of the biped which brings in a passive DOF making the bipedal systems *underactuated*.

The absolute orientation of the biped is considered as an additional passive DOF in certain biped models [7, 76, 87, 100]. Such biped models are underactuated in nature resulting in nontrivial *zero-dynamics* [77]. It is essential to investigate the stability of the associated zero-dynamics (ZD) while dealing with underactuated systems. Periodic trajectories with the specific properties result in stable zero-dynamics of a two-link acrobot [100]. The periodic nature of the locomotion/gait is utilized to stabilize the ZD [7, 11, 12, 76]. Poincaré return map is an effective tool to validate periodicity and *orbital stability* [7,76]. Simplified biped models such as spring-damper systems are helpful in establishing periodicity in locomotion [12].

The concept of orbital stability is useful while dealing with the associated stability issues in point-foot bipeds [7, 11, 76]. By periodically attaining certain postures, even

though statically unstable, the orbital stability is achieved. Similar concepts are useful in analyzing stability of periodic activities such as running and hopping.

Fast dynamical activities like running, jumping or hopping are reported [11, 12, 78, 79] and experimentally realized [80], [81]. The Flight phase is common in these activities when the physical system looses contact with the ground. In the Flight phase it is noticeable that ground-reaction-force (GRF) becomes zero and angular momentum is conserved.

GRF is often used as a feedback to control the jumping motion [59, 82–84]. GRF data obtained from human jumping phases is utilized to compute the biped jumping gaits by optimizing the inertial forces [82]. Simplification of bipedal dynamics, for example inverted pendulum model, is helpful in developing force control strategies for jumping gait generation [83, 84]. Time of application of the control-scheme is important in designing the effective force-control strategies for vertical jumping [59].

In a number of studies, angular momentum is used for jumping motion control [58,85,86]. Mita et el. utilize an angular momentum conservation principle to develop an optimal control strategy to produce jumping motion [85]. The fight phase is initiated by non-zero angular momentum of a two-link planar robot in [85]. The motion of a four-link gymnastic robot is controlled using feedback linearizarion by Buss et al. [86]. *Non-holonomic* motion planning needs identification of few discrete states duringFlight phase [86]. Hyon et al. [58] report back-handspring experiment by controlling the angular momentum about center-of-mass (CM).

Unlike running and hopping, jumping is aperiodic. Hence, the concepts of periodicity and orbital stability are not applicable to resolve the stability issues involved in jumping. Although, static stability is possible in point-foot bipeds, presence of

foot essentially provides greater stability margin. Foot compliance model is required to obtain statically stable equilibrium for biped with foot. The traditional stability concepts such as ZMP and FRI are not suitable to address the situation when foot compliance model along with foot-rotation is considered. Flat-foot biped locomotion, which is not always the case with the foot compliance model, is normally assumed for ZMP-based stability analysis. The location of FRI point indicates whether the foot is about to rotate or not. The FRI point is not relevant once the foot rotates. Stability considerations for the activities like back-handspring, handstand, somersault are reported in [57, 58] which are confined to gait generation and control strategies. The stability issues involved with foot compliance and foot-rotation are not explicitly resolved.

Stability analysis associated with foot compliance model and foot-rotation during landing is the major motivation of the current work. Stability issues involved with landing in jumping motion of a biped structure are investigated in the work. The jumping gait is generated for a biped robot taking foot-rotation into consideration. The biped model becomes underactuated due to the presence of passive DOF at the contact between the toe and the ground. Foot compliance with ground is modeled as a spring-damper system [92]. The control problem for an underactuated model along with the foot compliance is formulated as *output zeroing* problem [77] where the *output functions* are constructed according to the desired jumping performance. The underactuated model with foot compliance results in a switching system with "*switching zero-dynamics.*" The conditions for landing stability are derived to stabilize the switching system. The stability of the switching system depends on the two quantities which are named as "*critical potential index*" and "*critical kinetic index*".

The jumping motion is experimentally realized and stability conditions are validated.

Section 4.1 describes the biped jumping robot and the computation of the associated dynamics. The control strategy is discussed in Section 4.2 while a selection procedure of desired gaits for the *output functions* is discussed in Section 4.3. The landing stability analysis is provided in Section 4.4. The simulations and experimentations of the jumping gait are described in Section 4.5 and conclusions are drawn in Section 4.6.

4.1 The Biped Jumper

4.1.1 Biped Jumper: BRAIL 2.0

BRAIL 2.0 (Bio-Robotics Activities in Locomotion 2.0) is a six degree-of-freedom (DOF) two legged robot. Each leg has three links: Foot, Shank and Thigh. The free end of the Foot link is the toe. The joint between the Foot link and the Shank link is the ankle. The joint between the Shank link and the Thigh link is the knee while that between the two Thigh links of the legs is the hip. Each leg has three joints and each joint has one actuator. The link attached at the hip is the Torso link. A weight is attached at the distal end of the Torso link. The amount and location of the weight on the Torso link are adjustable. The biped has a total of seven links. BRAIL 2.0 can not bend in frontal plane as it does not have any 'roll' DOF in its legs. BRAIL's motion is restricted to sagittal plane making it a planar robot.

The mechanical design is done in Autodesk Inventor (usa.autodesk.com). The Autodesk design and the robot BRAIL 2.0 are shown in Fig. 4.1. The robot weighs 1.37 kg and is 0.451 m high. The biped model, developed in *Autodesk Inventor*, is

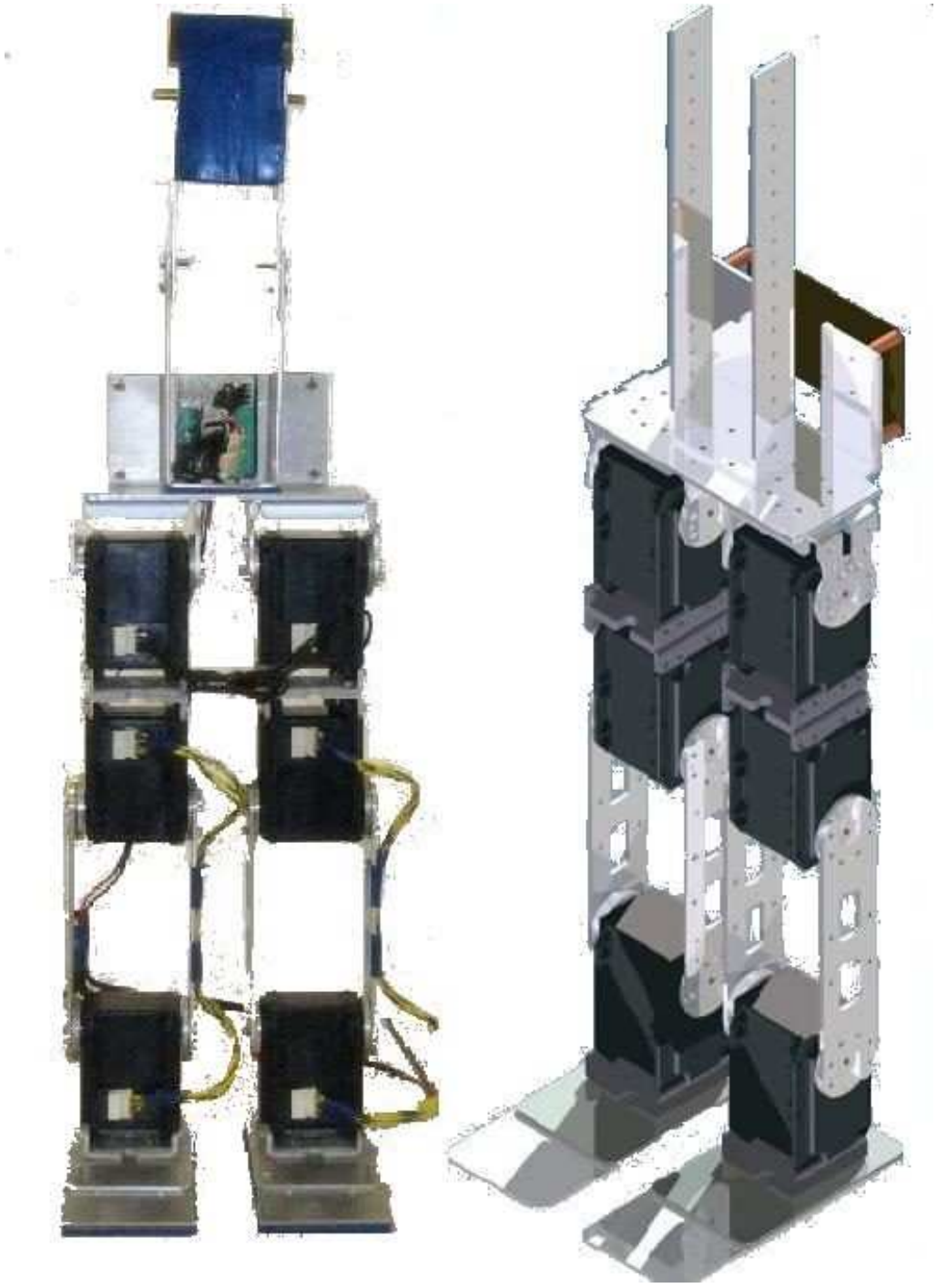

Figure 4.1: BRAIL 2.0 and Autodesk design

Table 4.1: Parameters of the BRAIL 2.0 biped

Link	Length (m)	Mass (kg)	CM (m)	Inertia about CM (kgm^2)
1	d_1=0.12	$m_1 = 0.32^a$	0.085	4.56×10^{-5}
2	d_2=0.1	$m_2 = 0.13^a$	0.05	4.6×10^{-5}
3	d_3=0.107	$m_3 = 0.61^a$	0.0535	3.65×10^{-4}
4	d_4=0.19	m_4=0.31	0.17	2.88×10^{-4}

$^a m_1/m_2/m_3$: Sum of the Foot/Shank/Thigh masses in the two legs.

imported to *Msc. Visualnastran* (www.mscsoftware.com) simulation environment. The biped parameters in Table 4.1 are collected from *Msc. Visualnastran* simulation environment and are used in the computation of the biped dynamics.

The biped jumping motion is studied with respect to the ground or any other flat surface in the sagittal plane (Fig. 4.2). The lengths and masses of the Foot, Shank, Thigh and Torso links are d_i and m_i (with $i = 1, 2, 3, 4$) respectively. The world coordinate system (X-Y) is fixed and absolute. The initial position of the toe is indicated by (x_0, y_0). The two legs are aligned to have identical pose in sagittal plane so as to act as a single leg. In sagittal plane the biped has four links and three joints (i.e. active DOFs). The Cartesian coordinates of the ankle, knee and hip joints are (x_1, y_1), (x_2, y_2) and (x_3, y_3) with respect to X-Y. The body angular coordinate vector $\theta_b = (\theta_2, \theta_3, \theta_4)^T$ describes the shape of the biped. The relative angles $(\theta_2, \theta_3, \theta_4)$ are known as *shape variables* and are realized by an actuator each in the legs. In consequence, each DOF consists of two actuators placed at the same location of the two legs in sagittal plane. θ_1 is the absolute angle between the foot and the ground. The vector of generalized coordinates $\theta_a := (\theta_1, \theta_b^T)^T$ indicates absolute posture of the biped. Angles are positive in the counter-clockwise direction.

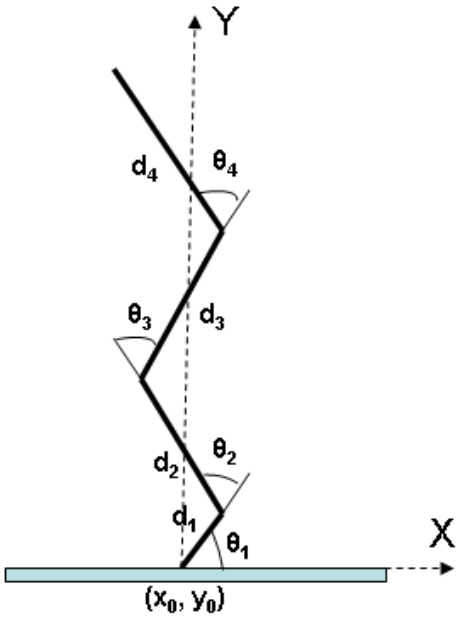

Figure 4.2: The Biped Model

Actuators

The RX-64 motors from *Robotis* Inc (www.robotis.com) are used as actuators. The motors weigh 116 g and provide a maximum torque of 6.4 Nm. With two actuators at each joints in sagittal plane, the maximum torque available at any joint is 12.8 Nm. These actuators are run in 'endless turn'/torque control mode. While controlling torque, the torque input to the motor can be adjusted at a resolution of about 0.1% of the maximum available torque at the current supply voltage. The actuators provide angular positions, velocities and joint torque as feedback.

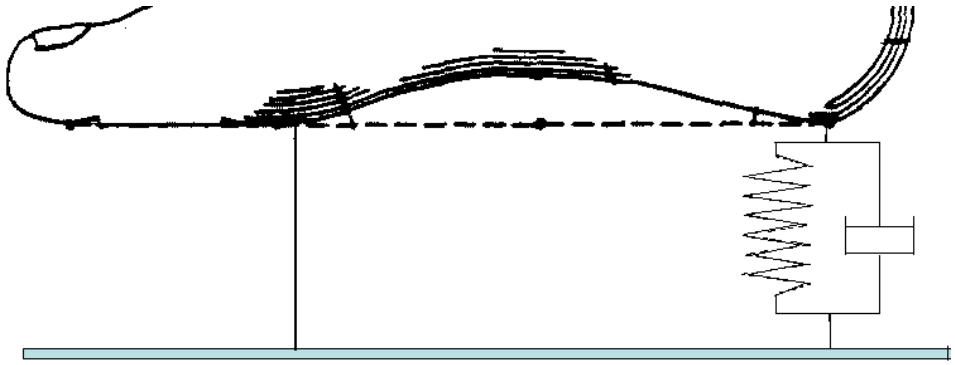

Figure 4.3: Foot compliance model.

Controller

The motors are controlled using a $CM2$ controller board *(www.robotis.com)*. The CM2 board uses an ATmega128 16 MHz processor. The controller can be connected to the PC using a RS232 port through which HEX code, generated from C programmes, are downloaded. A unique ID is set for each actuator for the controller to communicate with them. The motors utilize RS-485 communication protocol to use the daisy chain technology. The controller can read the joint angular positions, velocities and torques of the each actuator connected in the daisy chain.

4.1.2 Foot Compliance Model and Foot Design

The foot-ground compliance model is shown in Fig. 4.3 by replacing the Foot link with a human foot. The entire contact-surface between the foot and the ground is represented by a pivot and a spring-damper system located at the toe and the ankle respectively.

The assumptions on the foot compliance model are:

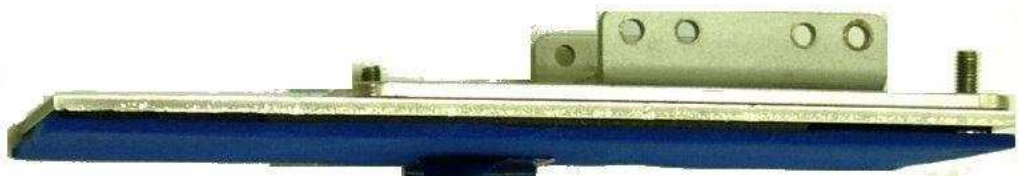

Figure 4.4: Foot plate of BRAIL 2.0

C1 When the foot is flat, the entire foot-ground contact surface is represented by the contacts at the toe and ankle.

C2 The toe-ground contact acts as a rigid pivot and the biped does not slip, rebound or penetrate at this point, that is, the vertical component of the ground reaction force is positive and the ratio of the horizontal component to the vertical component does not exceed the coefficient of static friction [7, 76].

C3 The ankle-ground contact acts as a spring-damper system where the biped can rebound or penetrate.

The Foot link of BRAIL 2.0 is shown in Fig. 4.4. Foot bottoms are cushioned by rubber sheets. The rubber cushioning helps to avoid slipping and provides damping to help shock absorption during jumping. The Foot link has two plates connected together at ankle while the toe part has only one plate. This makes the ankle-ground joint better damped and stronger to absorb impacts during landing.

4.1.3 Jumping Sequences

The jumping process is divided into three phases: Take-off phase, Flight phase, and Touch-down phase (Fig. 4.5). The biped's absolute position is specified by the Cartesian Coordinates of CM (x_{cm}, y_{cm}) with respect to the world coordinate frame

X-Y. In the Take-off phase the Foot link is in contact with the ground and $\dot{y}_{cm} > 0$. The biped is said to be in Touch-down phase when the Foot link is in contact with the ground and $\dot{y}_{cm} < 0$. There is no contact with the ground in Flight phase.

At the time of initiation of the Flight phase $\dot{y}_0 > 0$. In Flight phase the biped's CM evolves according to Newton's second law,

$$\begin{aligned} \ddot{x}_{cm} &= 0, \\ \ddot{y}_{cm} &= -g. \end{aligned} \tag{4.1}$$

In the Take-off and Touch-down phases, the CM $(x_{cm}(\theta_a), y_{cm}(\theta_a))$ of the biped can be computed with respect to the toe position:

$$\begin{aligned} x_{cm}(\theta_a) &= \frac{\sum_{i=1}^{4} m_i x_{cmi}}{\sum_{i=1}^{4} m_i}, \\ y_{cm}(\theta_a) &= \frac{\sum_{i=1}^{4} m_i y_{cmi}}{\sum_{i=1}^{4} m_i}, \\ f_{cm}(\theta_a) &= \begin{bmatrix} x_{cm}(\theta_a) \\ y_{cm}(\theta_a) \end{bmatrix}, \end{aligned} \tag{4.2}$$

where m_i and (x_{cmi}, y_{cmi}) indicate the mass and position of the CM of the i^{th} link respectively. Therefore, the linear velocity of the biped's CM (with respect to the toe) is given by:

$$\begin{bmatrix} \dot{x}_{cm}(\theta_a) \\ \dot{y}_{cm}(\theta_a) \end{bmatrix} = \frac{\partial f_{cm}(\theta_a)}{\partial \theta_a} \dot{\theta}_a. \tag{4.3}$$

While standing statically on flat-foot in sagittal plane, the biped is statically stable if condition (4.4) is satisfied [6].

$$0 \leq x_{cm}(\theta_a) \leq footlength = d_1. \tag{4.4}$$

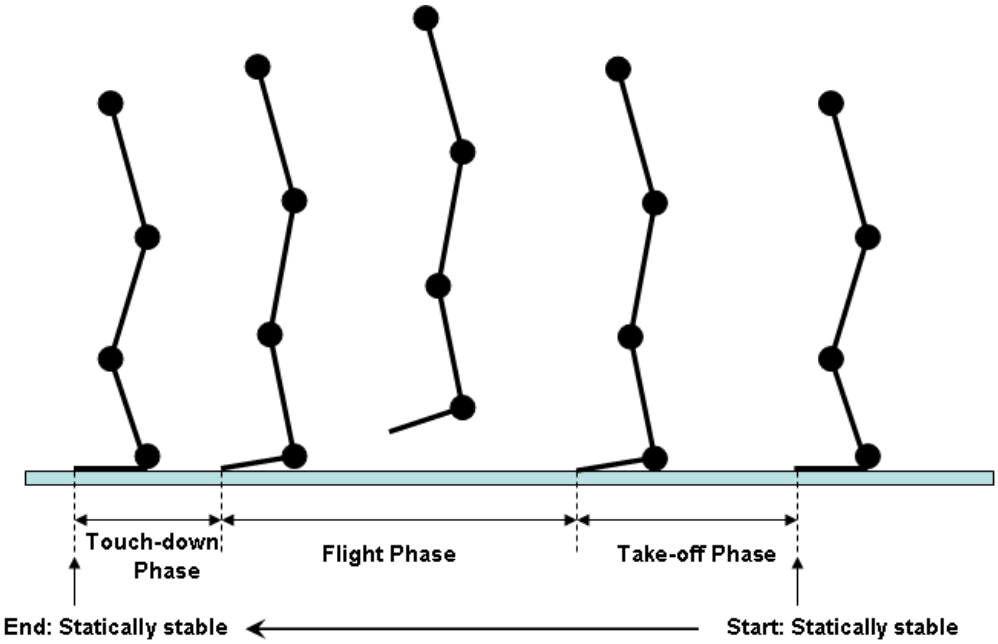

Figure 4.5: Phases of Jumping Motion.

Without loss of generality, it is assumed that the jumping motion starts from a statically stable posture with the origin of the world coordinate system coinciding with the position of the toe. The toe is in contact with the ground in both Take-off and Touch-down phases and, the toe-ground contact acts as a rigid pivot during these phases. Impact occurs when the toe touches the ground soon after the Flight phase or just before the Touch-down phase. Due to the impact, the joint angular velocities change instantaneously while the joint angular positions remain unchanged. The desired gaits in three jumping phases are computed off-line ensuring landing stability. Stability of the jumping gaits depends on the biped dynamics and control strategies. The control strategies ensure asymptotic convergence to a statically stable posture at the end of the Touch-down phase.

4.1.4 The Lagrangian Dynamics of the Biped in Take-off and Touch-down Phases

The dynamic model is obtained using the method of Lagrange, which consists of first computing the kinetic and potential energies of the each link, and then summing them up to compute the total kinetic energy, K_s and the total potential energy, P_s [75]. The Lagrangian is defined as $L_s = K_s - P_s$, and the dynamical model is determined from the Lagrange's equation,[1]

$$\frac{d}{dt}\frac{\partial L_s}{\partial \dot{\theta_a}} - \frac{\partial L_s}{\partial \theta_a} = \tau_s, \tag{4.5}$$

where τ_s is the vector of the generalized forces and torques applied to the biped.

The external torques are,[1]

$$\tau_s = \begin{bmatrix} \tau_1 \\ \\ \tau_2 \\ \\ \tau_3 \\ \\ \tau_4 \end{bmatrix} = B_{\bar{t}s}u_t + B_{ss}u_s, \tag{4.6}$$

where $u_s = [\ \tau_2 \quad \tau_3 \quad \tau_4\ ]^T$ are the torques applied at the ankle, knee and waist actuators respectively during both Take-off and Touch-down phases. $u_t = \tau_1$ is the torque generated at the toe-ground contact point due to ground reaction forces at the heel-ground contact point and is given by,

$$\tau_1 = \begin{cases} -kd_1^2\theta_1 - Dd_1^2\dot{\theta}_1 & \text{when } \theta_1 \leq 0 \\ \\ 0 & \text{otherwise,} \end{cases} \tag{4.7}$$

[1] 's' stands for the Take-off and Touch-down phase, 'f' for the Flight phase, 'b' for shape variables, 'a' for absolute orientation and '$\bar{t}$' for toe-ground joint.

where k and D are the spring constant and damping of the ankle-ground contact and,

$$B_{\bar{t}s} = \begin{bmatrix} 1 \\ 0 \\ 0 \\ 0 \end{bmatrix}, B_{ss} = \begin{bmatrix} 0 & 0 & 0 \\ 1 & 0 & 0 \\ 0 & 1 & 0 \\ 0 & 0 & 1 \end{bmatrix}. \tag{4.8}$$

The dynamic model during take-off and touch-down phases can therefore be written as,[1]

$$M_s(\theta_b)\ddot{\theta}_a + V_s(\theta_b, \dot{\theta}_a) + G_s(\theta_a) = \tau_s, \tag{4.9}$$

where M_s is the 4×4 inertial matrix about toe, V_s is 4×1 vector containing the Coriolis and centrifugal terms, and G_s is the 4×1 gravity vector. The computations of M_s, V_s and G_s are provided in Section 4.1.5.

As the inertial matrix only depends on the shape variables, the $M_s(\theta_b)$ is independent of θ_1 [76]. The kinetic and potential energies of the robot in the take-off and touch-down phases are given by,

$$\begin{aligned} K_s &= \frac{1}{2}\dot{\theta_a}^T M_s(\theta_b)\dot{\theta}_a, \\ P_s &= mgy_{cm}(\theta_a), \end{aligned} \tag{4.10}$$

where m is the total mass of the robot.

Introducing the state vector $x_s := (\theta_a^T, \dot{\theta}_a^T)^T$, the Lagrangian model (4.9) is expressed as

$$\begin{aligned} \dot{x}_s &= \begin{bmatrix} \dot{\theta}_a \\ M_s^{-1}(-V_s - G_s + B_{\bar{t}s}u_t) \end{bmatrix} + \begin{bmatrix} 0 \\ M_s^{-1}B_{ss}u_s \end{bmatrix} \\ &= f_s(x_s) + g_s(x_s)u_s, \end{aligned} \tag{4.11}$$

where $x_s \epsilon \Delta_s$, $\Delta_s := \{x_s = (\theta_a^T, \dot{\theta_a^T})^T \mid y_0 = 0, y_1 \geq 0, y_2 > 0, y_3 > 0, y_4 > 0, \theta_a \epsilon \Re^4\}$.

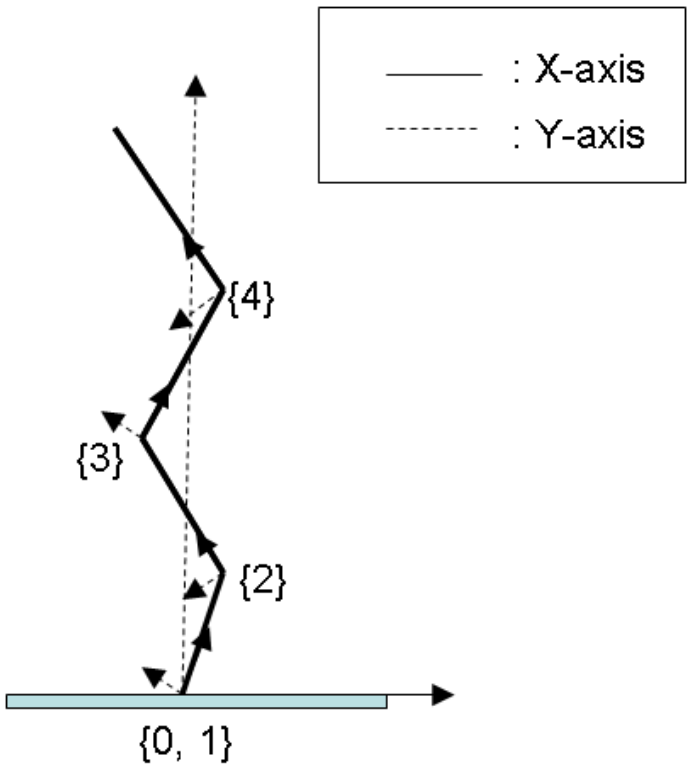

Figure 4.6: Coordinate System Assignment for Lagrangian formulation.

4.1.5 Lagrangian Dynamics Computation of the at the Take-off and Touch-down phases

For Lagrangian formulation of the biped, coordinate system assignment is shown in Fig. 4.6. The Denavit-Hartenberg (DH) [5] parameters are defined by,

A_i : The distance from Z_i to Z_{i+1} measured along X_i.

H_i : The distance from X_{i-1} to X_i measured along Z_i

ϕ_i : The angle between X_{i-1} to X_i measured about Z_i.

α_i : The angle between Z_i to Z_{i+1} measured about X_i.

Table 4.2: DH Parameters of the Robot

i	α_{i-1}	A_{i-1}	H_i	ϕ_i
1	0	0	0	θ_1
2	0	d_1	0	θ_2
3	0	d_2	0	θ_3
4	0	d_3	0	θ_4

Table 4.1.5 gives the values of DH parameters of the biped kinematic model in Fig. 4.6.

The general form of the homogeneous transformation matrix between $(i-1)^{th}$ and i^{th} link is given by [5],

$$T_i^{i-1} = \begin{bmatrix} c\phi_i & -s\phi_i & 0 & A_{i-1} \\ s\phi_i c\alpha_{i-1} & c\phi_i c\alpha_{i-1} & -s\alpha_{i-1} & -s\alpha_{i-1}H_i \\ s\phi_i s\alpha_{i-1} & c\phi_i s\alpha_{i-1} & c\alpha_{i-1} & c\alpha_{i-1}H_i \\ 0 & 0 & 0 & 1 \end{bmatrix},$$

where $s(.)$ indicates $sin(.)$ and $c(.)$ indicates $cos(.)$. The partial derivative of T_i^{i-1} with respect to ϕ_i is given by,

$$\begin{aligned} \frac{\partial T_i^{i-1}}{\partial \phi_i} &= T_i^{i-1} Q, \\ T_i^0 &= T_1^0 \cdot T_2^1 \cdot T_3^2 \cdots T_i^{i-1}, \end{aligned} \tag{4.12}$$

where Q is given by,

$$Q = \begin{bmatrix} 0 & -1 & 0 & 0 \\ 1 & 0 & 0 & 0 \\ 0 & 0 & 0 & 0 \\ 0 & 0 & 0 & 0 \end{bmatrix}.$$

Let us define,

$$\begin{aligned} U_{ij} &= \frac{\partial T_i^0}{\partial \theta_j} \\ &= \begin{cases} T_j^0 Q T_i^j & j \leq i \\ 0 & j > i \end{cases} \end{aligned} \tag{4.13}$$

and,

$$\begin{aligned} U_{ijk} &= \frac{\partial U_{ij}}{\partial \theta_k} \\ &= \begin{cases} T_k^0 Q T_j^k Q T_i^j & i \geq j \geq k \\ T_j^0 Q T_k^j Q T_i^k & i \geq k \geq j \\ 0 & i < j \ \ or \ i > k \end{cases} \end{aligned} \tag{4.14}$$

The elements of the inertial matrix M_s is given by,

$$M_{s,i,k} = \sum_{j=max(i,k)}^{4} Trace(U_{jk} J_j U_{ji}^T). \tag{4.15}$$

The elements of V_s and G_s matrices are given by,

$$\begin{aligned} V_{s,i} &= \sum_{k=1}^{4} \sum_{m=1}^{4} h_{ikm} \dot{\theta}_k \dot{\theta}_m, \\ G_{s,i} &= \sum_{j=i}^{4} (-m_j g U_{ji} r_j^j), \\ i &= 1, 2, 3, 4, \end{aligned} \tag{4.16}$$

where h_{ikm}, g and J_j are given by,

$$\begin{aligned} v_{ikm} &= \sum_{j=max(i,k,m)}^{4} Trace(U_{jkm} J_j U_{ji}^T), \\ g &= [0 \ -9.81 \ 0 \ 0]^T \ m/s^2, \\ J_i &= r_i r_i^T m_i, \end{aligned} \tag{4.17}$$

where r_i is the center of mass of the i^{th} link with respect to i^{th} coordinate system.

4.1.6 The Lagrangian Dynamics of the Biped in Flight Phase

In the Flight phase, the generalized vector coordinates are $\theta_f := (\theta_1, {\theta_b}^T, x_{cm}, y_{cm})^T$. In terms of the generalized coordinates of the robot, θ_f, the total kinetic and potential energies in the Flight phase become,[1]

$$\begin{aligned} K_f &= \frac{1}{2}{\dot{\theta}_f}^T D_f(\theta_b)\dot{\theta}_f, \\ P_f &= mgy_{cm}, \end{aligned} \tag{4.18}$$

where D_f is as per (4.19).

$$D_f = \begin{bmatrix} M_f(\theta_b) & 0_{4\times 2} \\ 0_{2\times 4} & mI_{2\times 2} \end{bmatrix}. \tag{4.19}$$

$I_{2\times 2}$ is 2×2 unity matrix and $M_f(\theta_b)$ is the inertial matrix of the robot about the center of mass [7] which is given by,

$$M_f(\theta_b) = M_s(\theta_b) - m\frac{\partial f_{cm}(\theta_a)}{\partial \theta_a}^T \frac{\partial f_{cm}(\theta_a)}{\partial \theta_a}. \tag{4.20}$$

Defining Lagrangian $L_f = K_f - P_f$, the Lagrangian equation becomes,

$$\frac{d}{dt}\frac{\partial L_f}{\partial \dot{\theta}_f} - \frac{\partial L_f}{\partial \theta_f} = \tau_f, \tag{4.21}$$

which leads to a model of the form,

$$D_f(\theta_b)\ddot{\theta}_f + V_f(\theta_f, \dot{\theta}_f) + G_f(\theta_f) = \tau_f. \tag{4.22}$$

The elements of the 6×1 vectors V_f and G_f are computed by [75],

$$\begin{aligned} V_{f,k} &= \sum_{i,j}^{6} v_{ijk}\dot{\theta}_i\dot{\theta}_j, \\ G_{f,k} &= \frac{\partial P_f}{\partial \theta_k}, \end{aligned} \tag{4.23}$$

where

$$v_{ijk} = \frac{1}{2}[\frac{\partial D_{f,k,j}}{\partial \theta_i} + \frac{\partial D_{f,k,i}}{\partial \theta_j} - \frac{\partial D_{f,i,j}}{\partial \theta_k}]. \tag{4.24}$$

The external torques are

$$\tau_f = \begin{bmatrix} 0 \\ \tau_2 \\ \tau_3 \\ \tau_4 \\ 0 \\ 0 \end{bmatrix} = B_{sf} u_f, \tag{4.25}$$

where $u_f = [\ \tau_2 \quad \tau_3 \quad \tau_4\ ]^T$ are the torques applied at the ankle, knee and waist actuators respectively during the Flight phase. And,

$$B_{sf} = \begin{bmatrix} 0 & 0 & 0 \\ 1 & 0 & 0 \\ 0 & 1 & 0 \\ 0 & 0 & 1 \\ 0 & 0 & 0 \\ 0 & 0 & 0 \end{bmatrix}. \tag{4.26}$$

Introducing state vector $x_f := (\theta_f^T, \dot{\theta_f^T})^T$, the model (4.22) becomes

$$\begin{aligned} \dot{x}_f &= \begin{bmatrix} \dot{\theta}_f \\ D_f^{-1}(-V_f - G_f) \end{bmatrix} + \begin{bmatrix} 0 \\ D_f^{-1} B_{sf} u_f \end{bmatrix} \\ &= f_f(x_f) + g_f(x_f) u_f, \end{aligned} \tag{4.27}$$

where $x_f \epsilon \Delta_f$, $\Delta_f := \{x_f = (\theta_f^T, \dot{\theta_f^T})^T \mid y_0 > 0, y_1 > 0, y_2 > 0, y_3 > 0, y_4 > 0, \theta_f \epsilon \Re^6\}$.

4.1.7 Impact Model and Angular Momentums

The impact takes place when the toe touches the ground at the end of the Flight phase. The impact model is assumed non-elastic with the velocity of the toe becoming zero instantaneously leading to discontinuity in joint velocities [91]. The position vector (θ_a) does not change due to impact. The toe-ground contact acts as an ideal pivot after the impact. The positions and velocities just before and after the impact are denoted by '$-$' and '$+$' respectively. Using the model in [91], the joint velocities just after impact are obtained.

The Cartesian position of the toe is expressed in terms of the robot's CM as per (4.28).

$$\begin{bmatrix} x_0 \\ y_0 \end{bmatrix} = \begin{bmatrix} x_{cm} \\ y_{cm} \end{bmatrix} - f_{cm}(\theta_a). \tag{4.28}$$

The impact model in [91] models the ground reaction force at impact as impulse with intensity I_G. The impact is assumed non-elastic with the velocity of the toe becoming zero instantaneously while the position vector does not change. The toe-ground contact acts as an ideal pivot after the impact. As the velocity of the toe becomes zero after the impact,

$$\begin{bmatrix} 0 \\ 0 \end{bmatrix} = \begin{bmatrix} \dot{x}^+_{cm} \\ \dot{y}^+_{cm} \end{bmatrix} - \frac{\partial f_{cm}(\theta_a)}{\partial \theta_a} \dot{\theta}^+_a. \tag{4.29}$$

The impact model is expressed as [91],

$$\begin{bmatrix} M_f(\theta_b) & 0 \\ 0 & mI_2 \end{bmatrix} \left(\begin{bmatrix} \dot{\theta}^+_a \\ \dot{x}^+_{cm} \\ \dot{y}^+_{cm} \end{bmatrix} - \dot{\theta}^-_f \right) = \begin{bmatrix} \frac{\partial f^T_{cm}(\theta_a)}{\partial \theta_a} \\ I_2 \end{bmatrix} I_G. \tag{4.30}$$

The I_G is expressed from (4.29) and (4.30),

$$I_G = m(\frac{\partial f_{cm}(\theta_a)}{\partial \theta_a}\dot{\theta}_a^+ - \begin{bmatrix} \dot{x}_{cm}^- \\ \dot{y}_{cm}^- \end{bmatrix}). \tag{4.31}$$

Using (4.31) in (4.30),

$$M_f(\theta_b)(\dot{\theta}_a^+ - \dot{\theta}_a^-) = \frac{\partial f_{cm}(\theta_a)}{\partial \theta_a}^T I_G = m\frac{\partial f_{cm}(\theta_a)}{\partial \theta_a}^T (\frac{\partial f_{cm}(\theta_a)}{\partial \theta_a}\dot{\theta}_a^+ - \begin{bmatrix} \dot{x}_{cm}^- \\ \dot{y}_{cm}^- \end{bmatrix}). \tag{4.32}$$

This further leads to,

$$\begin{aligned} (M_f(\theta_b) &- m\frac{\partial f_{cm}(\theta_a)}{\partial \theta_a}^T \frac{\partial f_{cm}(\theta_a)}{\partial \theta_a})\dot{\theta}_a^+ = M_f(\theta_b)\dot{\theta}_a^- - m\frac{\partial f_{cm}(\theta_a)}{\partial \theta_a}^T \begin{bmatrix} \dot{x}_{cm}^- \\ \dot{y}_{cm}^- \end{bmatrix}, \\ \Longrightarrow M_s(\theta_b)\dot{\theta}_a^+ &= [M_f(\theta_b); m\frac{\partial f_{cm}(\theta_a)}{\partial \theta_a}^T]\dot{\theta_f}^-, \\ \Longrightarrow \dot{\theta}_a^+ &= M_s(\theta_b)^{-1}[M_f(\theta_b); m\frac{\partial f_{cm}(\theta_a)}{\partial \theta_a}^T]\dot{\theta_f}^-. \end{aligned} \tag{4.33}$$

4.1.8 Jumping Motion and Angular Momentum relations

The jumping motion is divided into three successive phases: Take-off phase, Flight phase and Touch-down phase. At the beginning of the Take-off phase the robot is in statically stable posture. In Take-off phase $\dot{y}_{cm} > 0$. The transition from the Take-off phase to the Flight phase is initiated by causing the velocity of the toe to become positive i.e. $\dot{y}_0 > 0$. The control law in Flight phase decides the time of transition from the Take-off phase to the Flight phase. In Take-off phase, the angular momentum of the biped about the toe is given by [7],

$$\sigma = \frac{\partial K_s}{\partial \dot{\theta}_1} = M_{s,1}\dot{\theta}_a. \tag{4.34}$$

The first row of (4.9) yields,

$$\dot{\sigma} = -G_{s,1} + \tau_1 = -mgx_{cm}(\theta_a) + \tau_1. \tag{4.35}$$

To achieve continuity in position and velocity variables, the initial values of the states, x_f, in the Flight phase are taken as the values at the end of the Take-off phase. Let σ_{cm} denote the angular momentum of the biped about its center of mass. In the Flight phase, σ_{cm} is computed by [7],

$$\sigma_{cm} = \frac{\partial K_f}{\partial \dot{\theta}_1} = M_{f,1}\dot{\theta}_a, \tag{4.36}$$

The first row of (4.22) yields,

$$\dot{\sigma}_{cm} = 0, \tag{4.37}$$

where the initial value of σ_{cm}, at the beginning of the Flight phase, is computed from the final values of the Take-off phase [7],

$$\sigma_{cm} = \sigma - m(x_{cm}\dot{y}_{cm} - y_{cm}\dot{x}_{cm}). \tag{4.38}$$

In addition, last two rows of (4.22) are,

$$\begin{aligned} \ddot{x}_{cm} &= 0, \\ \ddot{y}_{cm} &= -g. \end{aligned} \tag{4.39}$$

Impact takes place at the end of the Flight phase when the toe touches the ground. Due to the effect of impact the velocities change instantaneously while the position does not. The angular momentum after the impact is computed from (4.40).

$$\sigma^+ = M_{s,1}(\theta_a^+)\dot{\theta}_a^+. \tag{4.40}$$

4.2 Control Law Development

The control law for all phases is formulated as an *output zeroing* problem resulting in nontrivial zero dynamics [77]. The output functions for all the three phases are defined as,

$$h(\theta_b, t) = \theta_b - \theta_b^d(t), \tag{4.41}$$

where $\theta_b^d(t)$ is the vector of three desired shape variable trajectories. The desired trajectories in Take-off, Flight and Touch-down phases are referred as $\theta_{bs}^d(t)$, $\theta_{bf}^d(t)$ and $\theta_{bl}^d(t)$ respectively.

From (4.41), the following equations can be derived[2],

$$\begin{aligned} \dot{h}(\theta_b, t) &= \frac{\partial h}{\partial x}\dot{x} - \dot{\theta}_b^d(t) = L_F h - \dot{\theta}_b^d(t), \\ \ddot{h}(\theta_b, t) &= (L_G L_F h)u + L_F^2 h - \ddot{\theta}_b^d(t). \end{aligned} \tag{4.42}$$

F, G and x come from the system equations (4.11) and (4.27). They are f_s, g_s and x_s for Take-off and Touch-down phases and f_f, g_f and x_f for the Flight phase. The feedback controller is defined as,

$$\begin{aligned} u(x) &= [L_G L_F h]^{-1}[v(h, L_F h) - L_F^2 h + \ddot{\theta}_b^d(t)], \\ v(h, L_F h) &= -K_d(\dot{\theta}_b - \dot{\theta}_b^d(t)) - K_p(\theta_b - \theta_b^d(t)), \end{aligned} \tag{4.43}$$

where K_d and K_p are constants such that $\ddot{h} + K_d\dot{h} + K_p h = 0$ is stable.

4.3 Selection of Desired Gait

The selection of the desired gaits[3] ($\theta_{bs}^d(t)$, $\theta_{bf}^d(t)$ and $\theta_{bl}^d(t)$) is discussed in this section. The selection procedure is based on the equivalent two-link model of the biped (Fig.

[2]Refer [77] for Lie Algebraic notations.

[3]'l' stands for the landing phase or Touch-down phase.

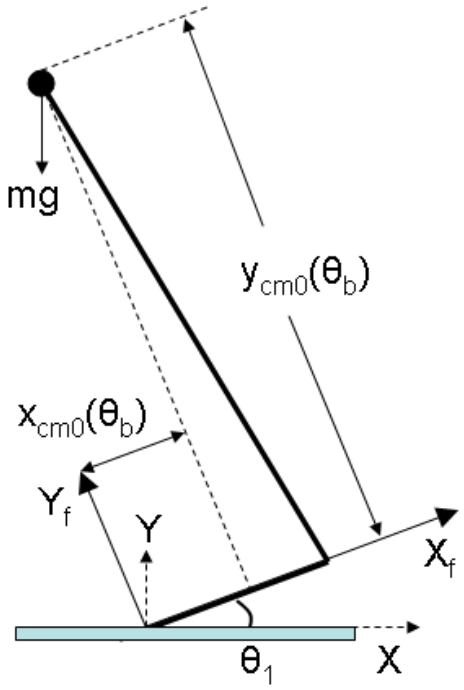

Figure 4.7: Two-link equivalent model of the biped with foot.

4.7). In the two-link model, the Foot link acts as one link and the distance from the ankle to CM of the rest of the biped acts as another link. The Cartesian coordinate $(x_{cm0}(\theta_b), y_{cm0}(\theta_b))$ is as per Fig. 4.7. Considering the mechanical structure of the biped, BRAIL 2.0, its physically reasonable configurations correspond to θ_b in the ranges (in rad): $1.8408 \leq \theta_2 \leq 3.1227$, $-2.7585 \leq \theta_3 \leq -0.5219$ and $0.2066 \leq \theta_4 \leq 1.2519$.

The desired gaits $\theta_b^d(t)$ are computed from the desired trajectories of $(x_{cm0}(\theta_b), y_{cm0}(\theta_b))$ in various phases using MATLAB's LSQNONLIN function which utilizes Trust-Region method [88] for nonlinear error minimization of the following function,

$$\Gamma(\theta_b^d) = (x_{cm0}^d(t) - x_{cm0}(\theta_b^d))^2 + (y_{cm0}^d(t) - y_{cm0}(\theta_b^d))^2, \tag{4.44}$$

where $(x_{cm0}^d(t), y_{cm0}^d(t))$ is the desired Cartesian trajectory of $(x_{cm0}(\theta_b), y_{cm0}(\theta_b))$.

The nonlinear error minimization on (4.44) is performed with the constraints that the solution vectors θ_b^d lie within the ranges of the physically reasonable configurations of the biped. Subsequently, a fourth order polynomial is considered to fit the set of solutions obtained from the nonlinear error minimization of (4.44). The fourth order polynomial resulted in error in the order of 10^{-4} m.

$$\theta_j^d(t) = a_{j,0} + a_{j,1}t + a_{j,2}t^2 + a_{j,3}t^3 + a_{j,4}t^4. \tag{4.45}$$

With the $\theta_j^d(t)$ in (4.45), $(x_{cm0}(\theta_b), y_{cm0}(\theta_b))$ closely follows $(x_{cm0}^d(t), y_{cm0}^d(t))$.

4.3.1 Take-off phase Gait

$(x^d_{cm0}(t), y^d_{cm0}(t))$ in Take-off phase is given by[4],

$$\begin{aligned} x^d_{cm0}(t) &= x_{cm0}(0) - C_x t, \\ y^d_{cm0}(t) &= y_{cm0}(0) + C_y t, \end{aligned} \tag{4.46}$$

where $(x_{cm0}(0), y_{cm0}(0))$ is the initial location of $(x_{cm0}(\theta_b), y_{cm0}(\theta_b))$. C_x and C_y are the desired horizontal and vertical take-off velocities. $(x^d_{cm0}(t), y^d_{cm0}(t))$ should be such that $\theta_a := (0, (\theta^d_b)^T)^T$ is real.

4.3.2 Flight phase Gait

The biped's CM evolves according to (4.1) in the Flight phase. The shape variables are adjusted to vary the CM position with respect to the toe (x_0, y_0). The desired trajectory, $y^d_{cm0}(t)$, is as per (4.47).

$$\begin{aligned} y_{cm}(t) &= y_{cm}(0) + \dot{y}_{cm}(0)t - \frac{1}{2}gt^2, \\ y^d_0(t) &= \eta^d sin(\frac{\pi}{t_f}t), \\ y^d_{cm0}(t) &= y_{cm}(t) - y^d_0(t), \end{aligned} \tag{4.47}$$

where η^d is the desired jumping height, t_f is the desired flight time and $y^d_0(t)$ is the desired trajectory of y_0 (Fig. 4.8). Similarly, the desired trajectory of $x^d_{cm0}(t)$ is as

[4]Negative sign appears in the expression of $x^d_{cm0}(t)$ because x is negative in the forward direction of jumping.

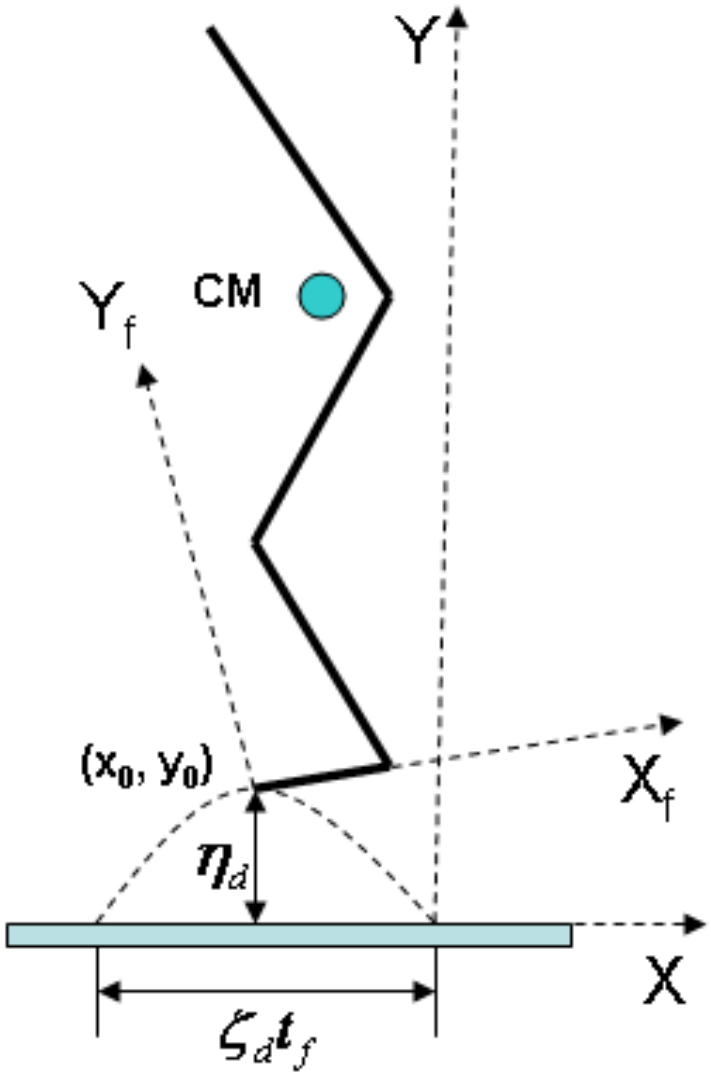

Figure 4.8: Flight-phase Gait Design Parameters.

per (4.48).

$$\begin{aligned} x_{cm}(t) &= x_{cm}(0) + \dot{x}_{cm}(0)t, \\ x_0^d(t) &= \zeta^d t, \\ x_{cm0}^d(t) &= x_{cm}(t) - x_0^d(t), \end{aligned} \tag{4.48}$$

where ζ^d is the desired length of jumping and $x_0^d(t)$ is the desired trajectory of x_0 (Fig. 4.8). The values of $x_{cm}(0)$, $\dot{x}_{cm}(0)$, $y_{cm}(0)$ and $\dot{y}_{cm}(0)$ are their values at the end of the Take-off phase. η^d, ζ^d and t_f should be chosen such that $\theta_1 > 0$ at the end of the Flight phase.

4.3.3 Touch-down phase Gait

The initial positions in the Touch-down phase are the positions at the end of the Flight phase while the initial velocities change instantaneously by (4.33) due to impact at the end of the Flight phase. The desired shape variables $\theta_j^d(t)$ $(j = 2, 3, 4)$ during the Touch-down phase are constants (4.49).

$$\theta_j^d(t) = Constant, \tag{4.49}$$

such that $0 < x_{cm0}(\theta_{bl}^d) < d_1 = footlength$ and $\dot{\theta}_j^d(t) = 0$.

4.4 Landing Stability Analysis

Landing stability is ensured by biped's asymptotic convergence to a statically stable posture. The control law (4.43), results in nontrivial ZD in Touch-down phase [77]. Stability of the closed-loop dynamics (CLD) is governed by the Touch-down phase *zero-dynamics*.

4.4.1 Switched Zero-Dynamics (SZD): Touch-down phase

The ZD manifold in Touch-down phase with the output function (4.41) is as per (4.50) [77].

$$Z_s := \{x_s \epsilon \Delta_s \mid \theta_b = \theta_b^d(t), \dot{\theta}_b = \dot{\theta}_b^d(t)\}. \tag{4.50}$$

The ZD (4.50) leads to (4.51) with desired shape trajectories as per [76].[5] (4.49)

$$\begin{aligned} \dot{\theta}_1 &= \frac{\sigma}{M_{s,1,1}(\theta_{bl}^d)}, \\ \dot{\sigma} &= -mgx_{cm}(\theta_1, \theta_{bl}^d) + \tau_1. \end{aligned} \tag{4.51}$$

The $x_{cm}(\theta_a)$ [4] has the following form,

$$x_{cm}(\theta_a) = -\sqrt{x_{cm0}^2(\theta_b) + y_{cm0}^2(\theta_b)} \times sin(\theta_1 - tan^{-1}(\frac{x_{cm0}(\theta_b)}{y_{cm0}(\theta_b)})). \tag{4.52}$$

M_s is independent of θ_1 and $M_{s,1,1}(\theta_{bl}^d)$ in (4.51) is a constant. Let us define three positive constants,

$$\begin{aligned} K_1 &= \frac{1}{M_{s,1,1}(\theta_{bl}^d)}\ kg^{-1}m^{-2}, \\ K_2 &= mg\sqrt{x_{cm0}^2(\theta_{bl}^d) + y_{cm0}^2(\theta_{bl}^d)}\ Nm, \\ K_3 &= tan^{-1}(\frac{x_{cm0}(\theta_{bl}^d)}{y_{cm0}(\theta_{bl}^d)})\ rad. \end{aligned} \tag{4.53}$$

Thus, the ZD in (4.51) becomes (4.54).

$$\begin{aligned} \dot{\theta}_1 &= K_1\sigma, \\ \dot{\sigma} &= K_2 sin(\theta_1 - K_3) + \tau_1. \end{aligned} \tag{4.54}$$

The initial value of θ_1 in Touch-down phase is positive and is given by its value at the end of the Flight phase. The value of σ changes on impact and its values at the

[5] $M_{s,r,c}$ indicates the element in r^{th} row and c^{th} column of the stance-phase inertia matrix.

point of impact, σ^+, is computed from (4.40). The torque at the toe-ground contact, τ_1, in (4.7) is written as (4.55).

$$\tau_1 = \begin{cases} -K_4\theta_1 - K_5\sigma & \text{when } \theta_1 \leq 0 \\ 0 & \text{otherwise} \end{cases} \tag{4.55}$$

where $K_4 = kd_1^2\ Nm$ and $K_5 = Dd_1^2K_1\ s^{-1}$. K_4 indicates the stiffness properties of the ankle-ground contact. The value of k is in the order of $10^6\ N/m$ for soft surfaces [95] leading to K_4 in the order of $10^4\ Nm$. The value of D is generally 5% to 25% of k making K_5 in the order of $10^2\ s^{-1}$. The zero-dynamics in (4.54) has two equilibrium points in the range $-\pi < \theta_1 < \pi$: $(\theta_1, \sigma) = (K_3, 0)$ and $(\theta_1, \sigma) \approx (-\frac{K_2 sin(K_3)}{K_4}, 0)$[6]. $(-\frac{K_2 sin(K_3)}{K_4}, 0)$ corresponds to statically stable posture where $\frac{K_2 sin(K_3)}{K_4} \approx 0$ as the value of K_4 is quite high compared to K_2.

The phase portrait of the ZD (4.54) shows that the Touch-down phase ZD is a switching system with two subsystems (Fig. 4.9): Subsystem A (4.56) for $\theta_1 > 0$ and Subsystem B (4.57) for $\theta_1 \leq 0$. Switching takes place whenever the ankle touches or leaves the ground. The overall ZD during Touch-down phase is named as Switching Zero-Dynamics (SZD).

In Subsystem A ($\theta_1 > 0$), Touch-down phase ZD is as per (4.56).

$$\begin{aligned} \dot{\theta}_1 &= K_1\sigma, \\ \dot{\sigma} &= K_2 sin(\theta_1 - K_3). \end{aligned} \tag{4.56}$$

In Subsystem B ($\theta_1 \leq 0$), the Touch-down phase ZD is as per (4.57).

$$\begin{aligned} \dot{\theta}_1 &= K_1\sigma, \\ \dot{\sigma} &= K_2 sin(\theta_1 - K_3) - K_4\theta_1 - K_5\sigma. \end{aligned} \tag{4.57}$$

[6] θ_1 is small compared to K_3 in Subsystem B i.e., $sin(\theta_1 - K_3) \approx -sin(K_3)$.

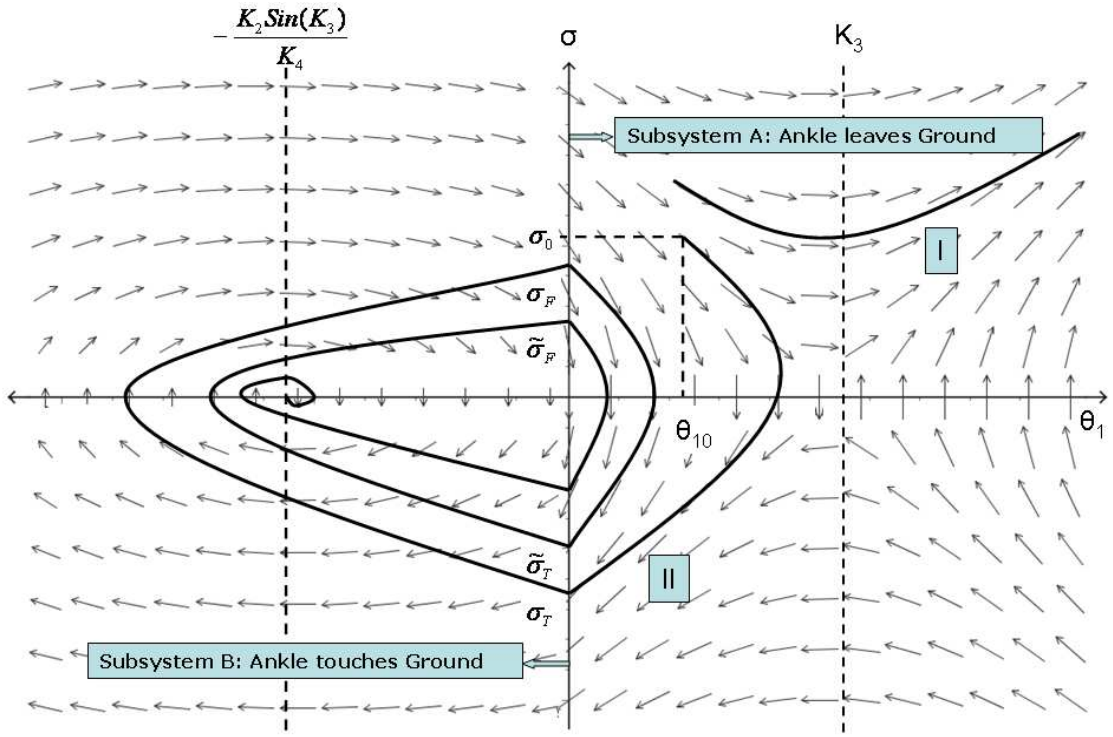

Figure 4.9: Phase Portrait of SZD (4.54). Trajectory I: Member of the set of trajectories going out with increasing θ_1. Trajectory II: Member of the set of trajectories reaching the $\theta_1 = 0$ plane.

The Touch-down phase always begins in Subsystem A. For the stability of the SZD, it needs to converge asymptotically to the equilibrium $(\theta_1, \sigma) = (-\frac{K_2 sin(K_3)}{K_4}, 0)$.

4.4.2 Stability of SZD

Stability analysis of SZD consists of three aspects. 1) In Subsystem A (Fig. 4.9), the phase-portrait can either follow trajectory I or II. Trajectory I leads to instability of the biped structure. For trajectory II, switching takes place at the $\theta_1 = 0$ plane which is required for stability of the ZD. 2) For stability in Subsystem B, the ZD should either converge to the equilibrium point $(\theta_1, \sigma) = (-\frac{K_2 sin(K_3)}{K_4}, 0)$ or it should switch back to Subsystem A. The possibility of initiating Flight phase from Subsystem B is not addressed here as the biped is not supposed to rebound at toe-ground contact according to the assumption (C2) of the foot-compliance model. 3) The switching should be such that the SZD asymptotically converges to the equilibrium point $(\theta_1, \sigma) = (-\frac{K_2 sin(K_3)}{K_4}, 0)$.

In the following analysis, it is assumed that SZD (4.54) starts at (θ_{10}, σ_0) with $\theta_{10} > 0$ being the value of θ_1 at the end of the Flight phase and σ_0 is computed from (4.40).

Theorem 4.4.1. *The SZD (4.56) reaches $\theta_1 = 0$ plane from initial states (θ_{10}, σ_0) if the following condition is satisfied ($\theta_{10} > 0$),*

(a) *When $K_3 > \theta_{10}$,*

$$\textbf{ZD1 :}\ \sigma_0 < \sqrt{\tfrac{2K_2}{K_1}(1 - cos(\theta_{10} - K_3))}$$

(b) *When $K_3 \leq \theta_{10}$,*

$$\textbf{ZD1 :}\ \sigma_0 < -\sqrt{\tfrac{2K_2}{K_1}(1 - cos(\theta_{10} - K_3))}.$$

Proof. From (4.56) for Subsystem A,

$$\begin{aligned} \frac{d\sigma}{d\theta_1} &= \frac{K_2 sin(\theta_1 - K_3)}{K_1 \sigma}, \\ \implies \sigma d\sigma &= \frac{K_2}{K_1} sin(\theta_1 - K_3) d\theta_1, \\ \implies \frac{\sigma_0^2}{2} &= \frac{\sigma^2}{2} + V_{ZD}(\theta_1), \\ \implies \sigma_0^2 &= \sigma^2 + 2V_{ZD}(\theta_1), \end{aligned} \tag{4.58}$$

where $V_{ZD}(\theta_1)$ is defined as following,

$$\begin{aligned} V_{ZD}(\theta_1) &= -\int_{\theta_{10}}^{\theta_1} \frac{K_2}{K_1} sin(\theta_1 - K_3) d\theta_1, \\ &= \frac{K_2}{K_1}(cos(\theta_1 - K_3) - cos(\theta_{10} - K_3)). \end{aligned} \tag{4.59}$$

The maximum value of $V_{ZD}(\theta_1)$ in (4.59) occurs when $\theta_1 = K_3$. The corresponding maximum value is denoted by V_{ZD}^{max} which is calculated by putting $\theta_1 = K_3$ in (4.59).

$$V_{ZD}^{max} = \frac{K_2}{K_1}(1 - cos(\theta_{10} - K_3)). \tag{4.60}$$

Equation (4.58) shows that if $\mid \sigma_0 \mid > \sqrt{2V_{ZD}^{max}}$, $\sigma = 0$ does not exists in the σ trajectory. Because $\mid \sigma_0 \mid \not> \sqrt{2V_{ZD}^{max}}$ at $\sigma = 0$. Similarly, $\mid \sigma_0 \mid < \sqrt{2V_{ZD}^{max}}$ indicates the existence of $\sigma = 0$ i.e., zero-crossing in the σ trajectory. Fig. 4.9 shows the vector field of the SZD. Depending on the initial state there can be four cases for $\theta_{10} > 0$.

1: With $K_3 > \theta_{10}$ and $\sigma_0 > 0$, the trajectories in Subsystem A (4.56) reach $\theta_1 = 0$ plane if there exists a zero-crossing in the σ trajectory. The zero-crossing exists when $\mid \sigma_0 \mid < \sqrt{2V_{ZD}^{max}}$ i.e. $\sigma_0 < \sqrt{2V_{ZD}^{max}}$ for $\sigma_0 > 0$.

2: With $K_3 > \theta_{10}$ and $\sigma_0 < 0$, the trajectories in Subsystem A (4.56) always reach the $\theta_1 = 0$ plane.

3: With $K_3 \leq \theta_{10}$ and $\sigma_0 > 0$, the trajectories in Subsystem A (4.56) never reach the $\theta_1 = 0$ plane.

4: With $K_3 \leq \theta_{10}$ and $\sigma_0 < 0$, the trajectories in Subsystem A (4.56) reach the $\theta_1 = 0$ plane if there is no zero-crossing in the σ trajectory. Zero-crossing exists if $\mid \sigma_0 \mid > \sqrt{2V_{ZD}^{max}}$, i.e. $\sigma_0 < -\sqrt{2V_{ZD}^{max}}$ for $\sigma_0 < 0$.

Cases 1 and 2 prove the part (a) while cases 3 and 4 prove the part (b) of *Theorem* 4.4.1.

It can be noticed that (4.56) represents the dynamics of a double-inverted pendulum or acrobot [4, 100]. The conditions in *Theorem* 4.4.1 ensure that the initial conditions do not correspond to the seperatrix passing through the equilibrium point $(K_3, 0)$.

□

Theorem 4.4.2. *The SZD (4.57) is locally asymptotically stable with initial states* $(0, \sigma_T)$*, if the following condition is satisfied*

ZD2 : $\frac{\sigma_T^2}{2\int_B \sigma^2 dt} > K_5 > 0$. *'B' indicates the time interval when the solution vector of (4.54) is in Subsystem B.*

Proof. Assume (4.56) reaches the $\theta_1 = 0$ plane at $(0, \sigma_T)$. From the zero-dynamics (4.57),

$$\begin{aligned} \frac{d\sigma}{d\theta_1} &= \frac{K_2 sin(\theta_1 - K_3) - K_4\theta_1 - K_5\sigma}{K_1\sigma}, \\ \Longrightarrow \int_{\sigma_T}^{\sigma} \sigma d\sigma &= \int_0^{\theta_1} \frac{K_2 sin(\theta_1 - K_3) - K_4\theta_1 - K_5\sigma}{K_1} d\theta_1, \\ \Longrightarrow \frac{\sigma_T^2}{2} &= V_B(\theta_1, \sigma) + K_5 \int_B \sigma^2 dt, \end{aligned} \tag{4.61}$$

where $V_B(\theta_1, \sigma)$ is as per (4.62).

$$V_B(\theta_1, \sigma) = -\int_0^{\theta_1} \frac{K_2 sin(\theta_1 - K_3) - K_4\theta_1}{K_1} d\theta_1 + \frac{\sigma^2}{2}. \tag{4.62}$$

(4.61) shows that $V_B(\theta_1, \sigma) > 0$ for $K_5 < \frac{\sigma_T^2}{2\int_B \sigma^2 dt}$ and $\dot{V}_B(\theta_1, \sigma) = -K_5\sigma^2$. Hence, $V_B(\theta_1, \sigma)$ is positive definite and its time derivative $\dot{V}_B(\theta_1, \sigma)$, along the zero-dynamics (4.57), is negative semi-definite when $0 < K_5 < \frac{\sigma_T^2}{2\int_B \sigma^2 dt}$. $\dot{V}_B(\theta_1, \sigma) = 0$ if $\sigma = 0$ which leads to $K_2 sin(\theta_1 - K_3) - K_4\theta_1 = 0$, the solution of which is the equilibrium point $(-\frac{K_2 sin(K_3)}{K_4}, 0)$. Therefore, $V_B(\theta_1, \sigma)$ is a *candidate Lyaponov function* [77] for $0 < K_5 < \frac{\sigma_T^2}{2\int_B \sigma^2 dt}$ and local asymptotic stability of (4.57) is proved using *LaShelle's invariance principle* [98].

□

The following are noticeable in Subsystem B,

- As $\dot{V}_B(\theta_1, \sigma) = -K_5\sigma^2$, convergence to equilibrium is faster when K_5 is higher. With higher K_5 (but less than $\frac{\sigma_T^2}{2\int_B \sigma^2 dt}$), the chances of bouncing back at the ankle-ground contact points is lesser.

- For the trajectory σ_T to σ_F (Fig. 4.9), $\int_{\sigma_T \to \sigma_F} \frac{K_2 sin(\theta_1 - K_3) - K_4\theta_1}{K_1} d\theta_1 = 0$. Therefore,

$$\sigma_F^2 = \sigma_T^2 - 2K_5 \int \sigma^2 dt. \tag{4.63}$$

  In case of bouncing back from the ankle-ground contact points, let the trajectories intersect with the $\theta_1 = 0$ plane at $\tilde{\sigma}_F$ (for $\sigma > 0$) and $\tilde{\sigma}_F$ (for $\sigma < 0$) (Fig. 4.9). (4.63) is true for the trajectories $\tilde{\sigma}_T$ to $\tilde{\sigma}_F$.

The SZD (4.54) is a switching system and switching occurs at the $\theta_1 = 0$ plane. Condition ZD1 ensures that (4.56) reaches the $\theta_1 = 0$ plane. Condition ZD2 ensures (4.57) either converges to the stable equilibrium $(-\frac{K_2 sin(K_3)}{K_4}, 0)$ or switches back to Subsystem A. However, the switching points $(0, \sigma_F)$ or $(0, \tilde{\sigma}_F)$ to Subsystem A might not satisfy ZD1, leading to instability. Therefore, conditions ZD1 and ZD2 are not sufficient to ensure the stability of SZD (4.54).

Theorem 4.4.3. *The SZD (4.54) locally asymptotically converges to the equilibrium point* $(-\frac{K_2 sin(K_3)}{K_4}, 0)$ *from initial states* (θ_{10}, σ_0) *if the following conditions are satisfied,*

SZD1 : $K_3 > \theta_{10} > 0$

SZD2 : $\mid \sigma_0 \mid < \sqrt{\frac{2K_2}{K_1}(1 - cos(\theta_{10} - K_3))}$

SZD3 : *ZD2.*

Proof. SZD1 and SZD2 are sufficient to ensure, (4.56) to reach the $\theta_1 = 0$ plane (from *Theorem* 4.4.1). SZD3 is sufficient to ensure local asymptotic stability of (4.57) (from *Theorem* 4.4.2). The stability of the SZD (4.54) is analyzed using the MLF approach [93].

The MLF approach is based on the existence of the *Lyapunov-like* functions for every subsystem whithin the switching system. The existence of *Lyapunov-like* functions for every subsystem in a switching system indicates the Lyapunov stability of the switching system. The *Lyapunov-like* function is defined as *candidate Lyaponov function* with at least negative semi-definite first derivative and monotonically non-increasing values at the switching plane during switching in a specific direction [93].

Let us define $V_A(\theta_1, \sigma)$ as (4.64).

$$V_A(\theta_1, \sigma) = \frac{\sigma^2}{2} + V_{ZD}(\theta_1). \tag{4.64}$$

(4.58) shows that $V_A(\theta_1, \sigma) > 0$ for $\sigma_0 \neq 0$ and $\dot{V}_A(\theta_1, \sigma) = 0$. $V_A(\theta_1, \sigma)$ is a *candidate Lyaponov function* for Subsystem A. Similarly, $V_B(\theta_1, \sigma)$ (4.62) is a *candidate Lyaponov function* for Subsystem B. Therefore, V_A and V_B are positive-definite and their first derivatives are at least negative semi-definite. The monotonicity of V_A and V_B can be shown considering the first few switchings. Suppose, the first switching occurs at $(0, \sigma_T)$ from Subsystem A to Subsystem B, the second switching at $(0, \sigma_F)$ from Subsystem B to Subsystem A, the third switching occurs at $(0, \tilde{\sigma}_T)$ from Subsystem A to Subsystem B (Fig. 4.9). (4.58) leads to (4.63) indicating $\mid \sigma_F \mid < \mid \sigma_T \mid$ and (4.58) leads to $\mid \tilde{\sigma}_T \mid = \mid \sigma_F \mid$. As a result $\sigma_T > \widetilde{\sigma}_T$ and $\sigma_F > \tilde{\sigma}_F$. $V_B(0, \sigma_T) > V_B(0, \widetilde{\sigma}_T)$ and $V_A(0, \sigma_F) > V_A(0, \tilde{\sigma}_F)$. Therefore, V_A and V_B are monotonically decreasing (non-increasing) at the switching plane in any particular direction of switching. Hence, V_A and V_B are *Lyapunov-like* functions for Subsystems A and B respectively. This proves the local asymptotic stability of the SZD.

It is noticeable that the stability of SZD requires $\mid \sigma_0 \mid < \sqrt{\frac{2K_2}{K_1}(1 - cos(\theta_{10} - K_3))}$ i.e., SZD2 does not allow $\sigma_0 < -\sqrt{\frac{2K_2}{K_1}(1 - cos(\theta_{10} - K_3))}$ which is not true in ZD1 for Subsystem A. Basically, SZD2 ensures the monotonic property of the candidate Lyaponov functions V_A and V_B.

□

The stability of SZD (4.54) depends on the initial states. The initial states of the SZD are the values at the closed-loop dynamics (CLD) when $h(\theta_b, t) = 0$ and $\dot{h}(\theta_b, t) = 0$. Hence, stability of SZD is dependent on that of the CLD and vice-versa.

4.4.3 Closed-loop Dynamics: Touch-down phase

Closed-loop dynamics in both Take-off and Touch-down phases is as per (4.65).

$$\begin{aligned}
\ddot{h} &+K_d\dot{h} + K_p h = 0, \\
\dot{\theta}_1 &= \frac{\sigma}{M_{s,1,1}} - \frac{M_{s,1,2}}{M_{s,1,1}}\dot{\theta}_2 - \frac{M_{s,1,3}}{M_{s,1,1}}\dot{\theta}_3 - \frac{M_{s,1,4}}{M_{s,1,1}}\dot{\theta}_4, \\
\dot{\sigma} &= -mgx_{cm}(\theta_a) + \tau_1.
\end{aligned} \tag{4.65}$$

In the Touch-down phase, the CLD leads to (4.66) with the control input (4.43) and desired gait (4.49).

$$\begin{aligned}
\dot{\xi}_1 &= \xi_2, \\
\dot{\xi}_2 &= -\frac{K_P}{\epsilon^2}\xi_1 - \frac{K_D}{\epsilon}\xi_2, \\
\dot{\theta}_1 &= \kappa_1(\xi_1)\sigma - \kappa_4(\xi_1)\xi_2, \\
\dot{\sigma} &= \kappa_2(\xi_1)sin(\theta_1 - \kappa_3(\xi_1)) + \tau_1,
\end{aligned} \tag{4.66}$$

where ϵ is a small positive constant, $K_p = \frac{K_P}{\epsilon^2}$, $K_d = \frac{K_D}{\epsilon}$, K_P, K_D are constant gains. ϵ acts as the perturbation parameter [98] and the significance of ϵ is explored in the proof of *Theorem* 4.4.5. ξ_1, ξ_2, $\kappa_1(\xi_1)$, $\kappa_2(\xi_1)$, $\kappa_3(\xi_1)$ and $\kappa_4(\xi_1)$ are as per (4.67).

$$\begin{aligned}
\xi_1 &= h(\theta_b, t) = \theta_b - \theta_{bl}^d, \\
\xi_2 &= \dot{h}(\theta_b, t) = \dot{\theta}_b, \\
\kappa_1(\xi_1) &= \frac{1}{M_{s,1,1}(\xi_1)}, \\
\kappa_2(\xi_1) &= mg\sqrt{(x_{cm0}^2(\xi_1) + y_{cm0}^2(\xi_1))}, \\
\kappa_3(\xi_1) &= tan^{-1}(\frac{x_{cm0}(\xi_1)}{y_{cm0}(\xi_1)}), \\
\kappa_4(\xi_1) &= [\ \frac{M_{s,1,2}}{M_{s,1,1}} \quad \frac{M_{s,1,3}}{M_{s,1,1}} \quad \frac{M_{s,1,4}}{M_{s,1,1}}\ ].
\end{aligned} \tag{4.67}$$

Lemma 4.4.4. *Consider the CLD (4.66).* $\kappa_3(\xi_1) > \theta_1$ *implies* $x_{cm}(\theta_a) > 0$ *and* $\kappa_3(\xi_1) \leq \theta_1$ *implies* $x_{cm}(\theta_a) \leq 0$.

Proof. Using (4.67), $\kappa_3(\xi_1) = tan^{-1}(\frac{x_{cm0}(\xi_1)}{y_{cm0}(\xi_1)})$.

$$\begin{aligned}
\kappa_3(\xi_1) &= tan^{-1}(\frac{x_{cm0}(\xi_1)}{y_{cm0}(\xi_1)}) > \theta_1, \\
\implies & \quad sin(\theta_1)y_{cm0}(\xi_1) - cos(\theta_1)x_{cm0}(\xi_1) < 0, \\
\implies & \quad \frac{\kappa_2(\xi_1)}{mg} sin(\kappa_3(\xi_1) - \theta_1) > 0, (\ \textit{Using (4.67)}) \\
\implies & \quad x_{cm}(\theta_a) > 0.(\ \textit{Using (4.52)})
\end{aligned}$$

Hence, $\kappa_3(\xi_1) > \theta_1$ implies $x_{cm}(\theta_a) > 0$ and similarly, $\kappa_3(\xi_1) \leq \theta_1$ implies $x_{cm}(\theta_a) \leq 0$. □

The last two equations in (4.66) ($\dot{\theta}_1$ and $\dot{\sigma}$) are known as *internal dynamics* of the system. Let us define $\psi = \theta_1 + \int \kappa_4(\xi_1) d\xi_1$. From (4.66) in Subsystem A ($\theta_1 > 0$),

$$\begin{aligned} \frac{d\sigma}{d\psi} &= \frac{\kappa_2 sin(\theta_1 - \kappa_3)}{\kappa_1 \sigma}, \\ \implies \sigma d\sigma &= \frac{\kappa_2}{\kappa_1} sin(\theta_1 - \kappa_3) d\psi, \\ \implies \frac{\sigma^2(0)}{2} &= \frac{\sigma^2}{2} + V_{ID}(\theta_1, \xi_1). \end{aligned} \tag{4.68}$$

where $V_{ID}(\theta_1, \xi_1) = -\int_{\psi_0}^{\psi} \frac{\kappa_2}{\kappa_1} sin(\theta_1 - \kappa_3) d\psi$, ψ_0 and $\sigma(0)$ are the values of ψ and σ at the beginning of the Touch-down phase. $\dot{V}_{ID}(\theta_1, \xi_1) = \kappa_2(\xi_1) sin(\kappa_3(\xi_1) - \theta_1)\sigma$ and the optimal values of $V_{ID}(\theta_1, \xi_1)$ occur at $\dot{V}_{ID}(\theta_1, \xi_1) = 0$. At $\sigma = 0$, with a specific combination of $\xi_1(0)$, $\xi_2(0)$, K_P, K_D and ϵ at the $\theta_1 = \theta_1(0)$ plane, $V_{ID}(\theta_1, \xi_1)$ is maximum (from (4.68)) and the maximum value is equal to $\frac{\sigma^2(0)}{2}$. Such maximum values of $V_{ID}(\theta_1, \xi_1)$ vary depending on the initial angular momentum $\sigma(0)$ during landing. There is a minimum value of $\sigma(0)$ below which the trajectory reaches the $\sigma = 0$ plane (trajectories I and IV in Fig. 4.10). In other words, there is a maximum value of $\sigma(0)$ above which the trajectory does not reach the $\sigma = 0$ plane (trajectories II and III in Fig. 4.10). The maximum values of $V_{ID}(\theta_1, \xi_1)$ corresponding to the maximum value of $\sigma(0)$ for which the trajectory reaches $\sigma = 0$ plane, indicates the restriction on the biped's joint angular velocities for stable landing and is named as the *critical kinetic index* in *Definition* 4.4.1.

Definition 4.4.1. Consider the CLD (4.66) when $\theta_1(0) < \kappa_3(\xi_1)$. For a specific combination $\xi_1(0)$, $\xi_2(0)$, K_P, K_D and ϵ at the $\theta_1 = \theta_1(0)$ plane, the value of V_{ID} corresponding to the maximum value of $\sigma(0)$ for which the trajectory reaches the $\sigma = 0$ plane is named as the *critical kinetic index*.

Critical kinetic index is denoted by V_{ID}^{max}. Numerically, V_{ID}^{max} is found by identifying the maximum Touch-down phase initial angular momentum $\sigma(0)$ for which the

trajectory reaches the $\sigma = 0$ plane and $V_{ID}^{max} = \frac{(\sigma(0))^2}{2}$.

Equation (4.3) leads to (4.69).

$$\begin{aligned} \dot{x}_{cm}(\theta_a) &= \frac{\partial x_{cm}(\theta_a)}{\partial \theta_a}\dot{\theta}_a, \\ \implies \quad & x_{cm}(\theta_a)\dot{x}_{cm}(\theta_a) = x_{cm}(\theta_a)\frac{\partial x_{cm}(\theta_a)}{\partial \theta_a}\dot{\theta}_a, \\ \implies \quad & \frac{x_{cm}^2(\theta_{a0})}{2} = \frac{x_{cm}^2(\theta_a)}{2} + V_{xcm}(\theta_1, \xi_1). \end{aligned} \tag{4.69}$$

where $V_{xcm}(\theta_1, \xi_1) = -\int_{\theta_{a0}}^{\theta_a} x_{cm}(\theta_a)\frac{\partial x_{cm}(\theta_a)}{\partial \theta_a}\dot{\theta}_a dt$ and $\theta_{a0} = \theta_a(0)$ at the beginning of the Touch-down phase. $\dot{V}_{xcm}(\theta_1, \xi_1) = -x_{cm}(\theta_a)\frac{\partial x_{cm}(\theta_a)}{\partial \theta_a}\dot{\theta}_a$. At $\theta_1 = \kappa_3(\xi_1)$, $x_{cm}(\theta_a) = 0$ and $\dot{V}_{xcm}(\theta_1, \xi_1) = 0$. Hence, $V_{xcm}(\theta_1, \xi_1)$ is maximum at $\theta_1 = \kappa_3(\xi_1)$ for a specific combination of $\xi_1(0)$, $\xi_2(0)$, K_P, K_D and ϵ at the $\sigma = \sigma(0)$ plane (from (4.69)). Such maximum values of $V_{xcm}(\theta_1, \xi_1)$ depend on the initial landing posture of the biped i.e., θ_{a0} or $x_{cm}(\theta_{a0})$. There is a maximum value of $x_{cm}(\theta_{a0})$ above which the trajectory does not reach the $\theta_1 = \kappa_3(\xi_1)$ plane (trajectories I and II in Fig. 4.10). In other words, there is a minimum value of $\theta_1(0)$ below which the trajectory does not reach $\theta_1 = \kappa_3(\xi_1)$ plane. The maximum values of $V_{xcm}(\theta_1, \xi_1)$ corresponding to the minimum value of $\theta_1(0)$ for which the trajectory reaches $\theta_1 = \kappa_3(\xi_1)$ plane, indicates the restriction on biped's joint angular positions for stable landing and is named as the *critical potential index* in *Definition* 4.4.2.

Definition 4.4.2. Consider the CLD (4.66) when $\theta_1(0) < \kappa_3(\xi_1)$. For a specific combination of $\xi_1(0)$, $\xi_2(0)$, K_P, K_D and ϵ at the $\sigma = \sigma(0)$ plane, the value of V_{xcm} corresponding to the minimum value of $\theta_1(0)$ for which the trajectory reaches the $\theta_1 = \kappa_3(\xi_1)$ plane is named as the *critical potential index*.

Critical potential index is denoted by V_{xcm}^{max}. Numerically, V_{xcm}^{max} is found by identifying the minimum value of $\theta_1(0)$ for which the trajectory reaches $\theta_1 = \kappa_3(\xi_1)$ plane

and $V_{xcm}^{max} = \frac{x_{cm}^2(\theta_{a0})}{2}$.

Theorem 4.4.5. *Consider the CLD (4.66) and SZD (4.54). The local asymptotic stability of the SZD (4.54) implies the local asymptotic stability of CLD (4.66) if the following conditions are satisfied,*

CLD1 : $x_{cm}(\theta_{a0}) > \sqrt{2V_{xcm}^{max}}$

CLD2 : $\mid \sigma(0) \mid < \sqrt{2V_{ID}^{max}}$

CLD3 : *ϵ is small enough to ensure that the internal dynamics closely follows the zero-dynamics (4.54).*

B' indicates the time interval when the solution vector of (4.66) is in Subsystem B.

Proof. Singular perturbation approach is used to prove the stability of the internal dynamics (4.66) [77, 98]. As the perturbation parameter ϵ in (4.66) changes, the system splits into two time-scaled dynamics [98]. With $\epsilon = 0$ in (4.66), the dynamics indicates the 'slow dynamics'. System dynamics with small positive non-zero ϵ indicates the 'quasi-steady-state' dynamics [98]. For the stability of the overall system both the 'slow dynamics' and the 'quasi-steady-state' dynamics must be stable.

The first two equations of (4.66) can be rewritten as (4.70). In (4.70), with $\epsilon \to 0$, $\xi_1 \to 0$ and $\xi_2 \to 0$ which leads to $\theta_b \to \theta_{bl}^d$ and $\dot{\theta}_b \to 0$. This further leads to $\kappa_1(\xi_1) \to K_1$, $\kappa_2(\xi_1) \to K_2$ and $\kappa_3(\xi_1) \to K_3$. Therefore, for $\epsilon = 0$, the *internal dynamics* (4.66) converges to SZD (4.54). The SZD (4.54) is locally asymptotically stable in a neighborhood specified by the conditions SZD1-3. For $\epsilon = 0$, (4.66) becomes locally asymptotically stable in a neighborhood specified by SZD1-3 [94]. Hence, the 'slow dynamics' with $\epsilon = 0$ is locally asymptotically stable in a neighborhood specified by SZD1-3.

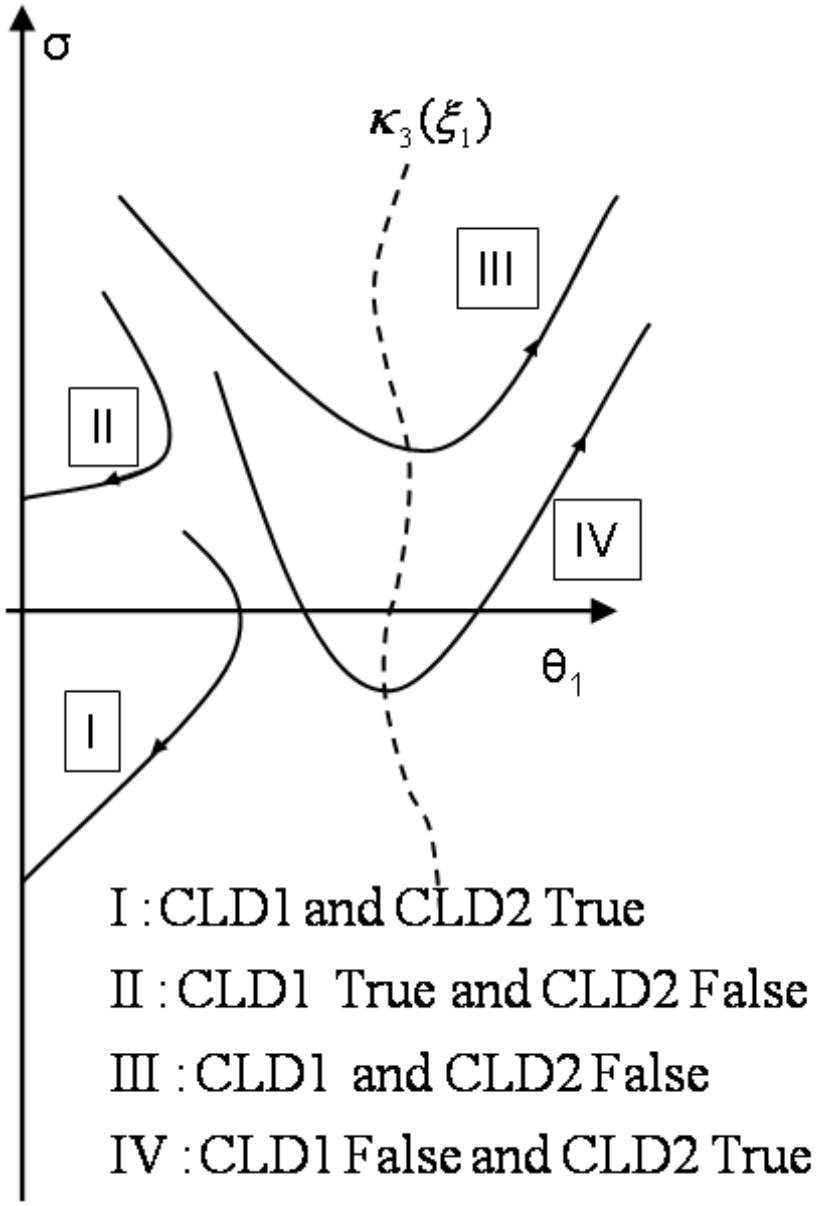

Figure 4.10: Stability of internal dynamics for $x_{cm}(\theta_{a0}) > 0$.

$$\begin{aligned} \dot{\xi}_1 &= \xi_2, \\ \epsilon^2 \dot{\xi}_2 &= -K_P \xi_1 - \epsilon K_D \xi_2. \end{aligned} \tag{4.70}$$

If $\epsilon \neq 0$ is a small positive number, then (4.66) reflects the 'quasi-steady-state' behavior. In (4.69), $\mid x_{cm}(\theta_{a0}) \mid < \sqrt{2V_{xcm}^{max}}$ indicates the existence of zero-crossing in $x_{cm}(\theta_a)$ trajectory. Similarly, $\mid \sigma(0) \mid < \sqrt{2V_{ID}^{max}}$ in (4.68) indicates the existence of zero-crossing in σ trajectory. If $x_{cm}(\theta_{a0}) > 0$, $\kappa_3(\xi_1) > \theta_1$ (using *Lemma* 4.4.4). As per CLD1, $x_{cm}(\theta_a)$ never changes sign and does not have zero-crossing which leads to $\kappa_3(\xi_1) > \theta_1$. As per CLD2, a zero-crossing exists in σ trajectory. Hence, CLD1 and CLD2 ensure that the system (4.66) follows trajectory I to reach the $\theta_1 = 0$ plane (Fig. 4.10).

In Subsystem B, with $\epsilon \neq 0$, the equilibrium point is computed by equating the last two equations of (4.66) to zero for $\xi_1 \neq 0$ and $\xi_2 \neq 0$. Considering $(\xi 1, \xi_2, \theta_1^\epsilon, \sigma^\epsilon)$ as the equilibrium of (4.66) with $\epsilon \neq 0$, θ_1^ϵ and σ^ϵ are given by (4.71)[7].

$$\begin{aligned} \theta_1^\epsilon &\approx -\frac{\kappa_2(\xi_1) sin(\kappa_3(\xi_1)) + K_5 \frac{\kappa_4(\xi_1)\xi_2}{\kappa_1(\xi_1)}}{K_4}, \\ \sigma^\epsilon &= \frac{\kappa_4(\xi_1)\xi_2}{\kappa_1(\xi_1)}. \end{aligned} \tag{4.71}$$

For analyzing the stability of the equilibrium point $(\xi 1, \xi_2, \theta_1^\epsilon, \sigma^\epsilon)$, The *candidate Lyapunov function* V_B^ϵ is chosen as (4.72). With $\frac{\sigma_T^2}{2\int_B \sigma^2 dt} > K_5 > 0$ as mentioned in CLD3, V_B^ϵ is positive definite.

$$V_B^\epsilon = \frac{\sigma_T^2}{2} - K_5 \int_B \sigma^2 dt + (\frac{K_p}{\epsilon^2}\xi_1^2 + \xi_2^2)\frac{1}{2}. \tag{4.72}$$

[7] θ_1^ϵ is small compared to $\kappa_3(\xi_1)$ in Subsystem B i.e., $sin(\theta_1 - \kappa_3(\xi_1)) \approx -sin(\kappa_3(\xi_1))$.

The time derivative of V_B^ϵ, computed along system dynamics, is given by (4.73).

$$\begin{aligned}\dot{V}_B^\epsilon &= -K_5\sigma^2 + (\frac{K_p}{\epsilon^2}\xi_1\dot{\xi}_1 + \xi_2\dot{\xi}_2), \\ &= -K_5\sigma^2 + \frac{K_p}{\epsilon^2}\xi_1\xi_2 + \xi_2(-\frac{K_P}{\epsilon^2}\xi_1 - \frac{K_D}{\epsilon}\xi_2), \\ &= -K_5\sigma^2 - \frac{K_D}{\epsilon}\xi_2^2. \end{aligned} \tag{4.73}$$

$\dot{V}_B^\epsilon = 0$ when $\sigma = 0$ and $\xi_2 = 0$ which further lead to $\xi_1 = 0$. This being the case, with $\xi_1 = 0$ and $\xi_2 = 0$, the system will behave like SZD (4.54) which is locally asymptotically stable. Hence, $\dot{V}_B^\epsilon < 0$ if CLD3 is true. The local asymptotic stability in Subsystem B is achieved by CLD3. CLD1-3 ensure the stability of the 'quasi-steady-state' system.

The 'slow dynamics' is corresponding to SZD and is locally asymptotically stable if SZD1-3 are true. The 'quasi-steady-state' system is asymptotically stable if CLD1-3 are true. CLD1-3 converges to SZD1-2 with time. Hence, the switching system (4.66) is locally asymptotically stable if CLD1-3 are true.

□

Stability of CLD is dependent on the *critical potential index* and *critical kinetic index*. Their closed-form expressions are zero and $\frac{K_2}{K_1}(1 - cos(\theta_{10} - K_3))$ respectively when the system is within the Z_s (4.50) manifold. Hence, using *Lemma* 4.4.4, SZD1-2 and CLD1-2 are equivalent stability conditions for SZD and CLD respectively. ϵ should be small enough to satisfy CLD3 to ensure CLD1-2 are held in the case of bouncing back at the ankle-ground contact point. The bipedal structure and properties of foot-ground contact surface decide the values of the stability parameters K_1, K_2, K_3, K_4 and K_5. Therefore, the stability of SZD depends mostly on the bipedal

structure and properties of foot-ground contact surfaces. However, stability of the CLD is dependent on the *critical potential index* and *critical kinetic index* which further depend on the design parameters K_p, K_d and ϵ.

4.5 Simulations and Experiments

4.5.1 Jumping Gait Simulations

Simulations are done based on the parameters shown in Table 4.1. The dynamics of the biped is computed in the MATLAB/Simulink environment. The dynamic parameters are expressed in C language code by using 'ccode' command for faster computation and simulation. The control algorithms are simulated in Microsoft VC++ environment using the C code of the biped-dynamics generated by MATLAB/Simulink. Integration algorithm is based on fourth order Runge-Kutta method with fixed step size of 0.0001 s.

The initial posture of the biped considered is $\theta_a = [\ 0 \quad 2.3638 \quad -1.5217 \quad 1.5286\ ]^T$ rad with zero joint angular velocities. With the initial posture, the location of CM is $x_{cm}(0) = 0.0646$ m and $y_{cm}(0) = 0.1155$ m. It is noticeable that $0 < x_{cm}(0) < d_1$ which indicates that the biped starts from a statically stable posture. The toe-ground contact point is considered as mentioned in (C2) and the parameters for the ankle-ground contact points are[8]: $K_4 = 40000\ Nm$ and $K_5 = 800\ s^{-1}$. The numerical values of K_4 and K_5 used in the simulation are adjusted such that negative value of θ_1 is within -0.001 rad in Subsystem B and there is no rebound at the ankle-ground

[8] K_4 and K_5 are chosen according to the range reported in [95].

Table 4.3: Robot's Jumping Gait

Phase	θ_j^d	$a_{j,0}$	$a_{j,1}$	$a_{j,2}$	$a_{j,3}$	$a_{j,4}$
Take-off	2	2.362	0.5441	-41.51	351.0	-1707.0
	3	-1.519	-1.052	79.32	-677.7	3313.0
	4	1.527	-4.826	-37.8	326.7	-1606.0
Flight	2	1.589	2.251	49.69	-537.9	1178.0
	3	-0.03766	-4.733	-105.8	1144.0	-2506.0
	4	0.5023	3.247	32.36	-423.3	922.9
Touch-down	2	2.3638	0	0	0	0
	3	-1.5217	0	0	0	0
	4	1.5286	0	0	0	0

contact points. The negative value of θ_1 corresponds to the penetration of the ankle-ground contact points into the ground. θ_1 being within -0.001 rad in Subsystem B, the penetration is approximately 0.1 mm in simulation. The desired polynomial coefficients of the shape variables $\theta_j^d(t)$ are chosen based on the method described in section 4.3 and are shown in Table 4.5.1. The values of different quantities during jumping are shown in Table 4.5.1.

In Take-off phase gait, the take-off time is 0.15 s, $C_x = 0$ and $C_y = 0.55\ m/s$. The control law (4.43) with feedback gains $K_p = 60$ and $K_d = 80$ is applied in Take-off phase. The final CM velocities are $\dot{x}_{cm}(0) = 0.2275\ m/s$ and $\dot{y}_{cm}(0) = 0.5143\ m/s$. These act as initial conditions for the Flight phase.

In the Flight phase gait, $t_f = 0.15$ s, $\eta^d = 0.025$ m and $\zeta^d = 0$. In the Flight phase, the control input is as in (4.43) with feedback gains $K_p = 400$ and $K_d = 300$. Impact occurs at the end of the Flight phase. Joint angular velocities change instantaneously as per (4.33) which leads to change in angular momentum as per (4.40). However, joint angular positions are not affected by the impact. Joint angular positions and

Table 4.4: Different Parameters Values at Jumping Phases.

Phase	Time (Seconds)	θ_1 (rad)	θ_2 (rad)	θ_3 (rad)	θ_4 (rad)	$\dot{\theta}_1$ (rad/s)	$\dot{\theta}_2$ (rad/s)	$\dot{\theta}_3$ (rad/s)	$\dot{\theta}_4$ (rad/s)	$x_{cm}(\theta_a)$ (m)	$y_{cm}(\theta_a)$ (m)
Take-off	0	0	2.3638	-1.5217	1.5286	0	0	0	0	0.0646	0.1155
	0.15	0.2646	1.8314	-0.5049	0.2492	0.9529	-11.2516	21.6933	-15.7940	0.0600	0.1797
Flight	0.1501	0.2646	1.8314	-0.5049	0.2492	0.9529	-11.2516	21.6933	-15.7940	0.0600	0.1797
	0.2866	0.1063	2.0276	-0.9337	0.5272	-1.9108	-2.4983	5.2413	-1.8405	0.0841	0.1585
Impact	0.2866	0.1063	2.0276	-0.9337	0.5272	-9.7475	5.0864	9.1061	-6.4239	0.0841	0.1585
Touch-down	0.2867	0.1063	2.0276	-0.9337	0.5272	-9.7475	5.0864	9.1061	-6.4239	0.0841	0.1585
	5.2867	0	2.3638	-1.5217	1.5286	0	0	0	0	0.0646	0.1155

velocities after the impact act as initial conditions for the Touch-down phase. After the impact $\sigma(0) = -1.62\ kgm^2s^{-1}$ and $\theta_1(0) = 0.1063$ rad. The flight time is 0.1366 seconds in simulation (Table 4.5.1).

The actual height (η) and length (ζ) of jumping is computed by,

$$\begin{bmatrix} \zeta \\ \eta \end{bmatrix} = \begin{bmatrix} 0 & 0 & 0 & 0 & 1 & 0 \\ 0 & 0 & 0 & 0 & 0 & 1 \end{bmatrix} \theta_f - f_{cm}(\theta_a). \tag{4.74}$$

The Flight phase is indicated by $\eta > 0$. $\zeta < 0$ indicates that the biped is jumping forward while $\zeta > 0$ indicates that the biped is jumping backward. With the parameters in Table 4.5.1, the biped jumped backward 7 mm and the maximum jumping height is 0.0249 m in simulation (Fig. 4.11).

The desired gait in Touch-down phase is the same as the initial posture of the biped. In Touch-down phase, the control law (4.43) with feedback gains $K_P = 9$, $K_D = 6$ and $\epsilon = 0.1$ is applied.

Table 4.5.1 shows the values of the various parameters during the jumping phases obtained in simulation (joint angular positions, velocities and torque inputs are discussed in section 4.5.2). The Touch-down phase is run in simulation for 5 s. Joint angular positions converge to the initial positions with time in the Touch-down phase.

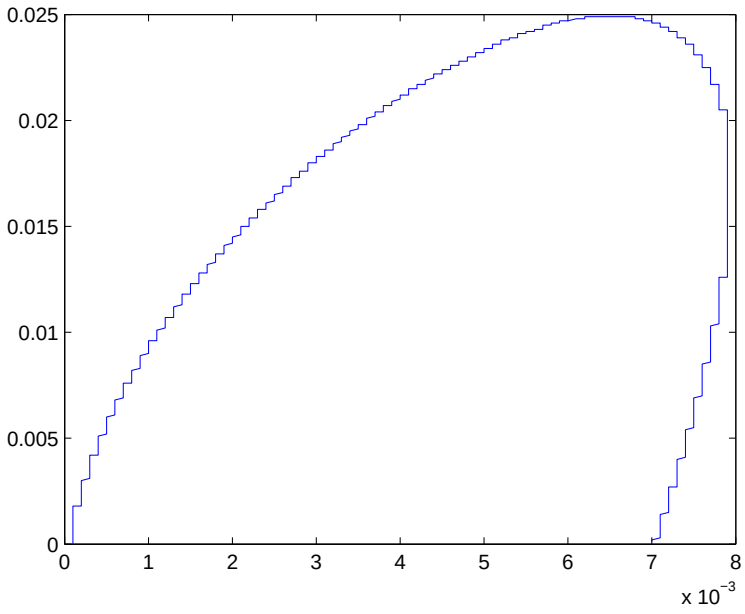

Figure 4.11: ζ vs. η.

Angular velocities converge to zero with time in the Touch-down phase (after 2.0 s). Fig. 4.13 shows the variation of τ_1 in Touch-down phase. Due to sudden change in angular velocities at point of impact, $\tau_1 = 37.3042$ Nm.

Stability in Touch-down phase

With the control input (4.43) and the desired gaits as per the Table 4.5.1, the values of different joint angles and velocities are shown in Table 4.5.1. Considering the final posture as $\theta_a = [\ 0 \quad 2.3638 \quad -1.5217 \quad 1.5286\ ]^T$ rad with zero joint angular velocities, $K_1 = 27.6501\ kg^{-1}m^{-2}$, $K_2 = 1.6873\ Nm$ and $K_3 = 0.5101\ rad$. The corresponding stable equilibrium point of zero-dynamics (4.54) is $(-0.000021, 0)$. The stability conditions CLD1-3 converge to SZD1-3 when the *internal dynamics* in (4.66)

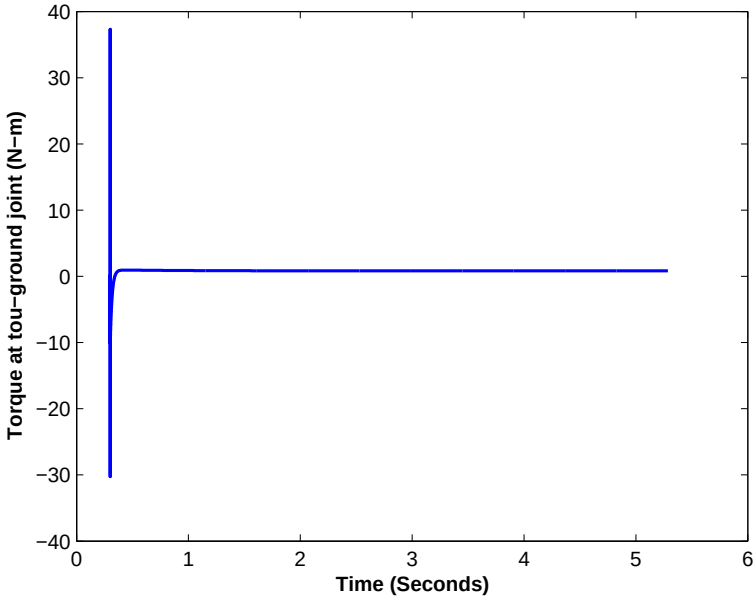

Figure 4.12: τ_1 at Touch-down phase.

Table 4.5: V_{xcm}^{max} and V_{ID}^{max}.

		$\theta_1(0)$ (rad)	θ_2 (rad)	θ_3 (rad)	θ_4 (rad)	$\dot{\theta}_1$ (rad/s)	$\dot{\theta}_2$ (rad/s)	$\dot{\theta}_3$ (rad/s)	$\dot{\theta}_4$ (rad/s)	$x_{cm}(\theta_a)$ (m)	$\sigma(0)$ kgm^2s^{-1}
V_{xcm}^{max} (m^2)	0.00	0.5934	2.0276	-0.9337	0.5272	-9.7475	5.0864	9.1061	-6.4239	0.000	-0.1619
V_{ID}^{max} ($kg^2m^4s^{-2}$)	0.015	0.1063	2.0276	-0.9337	0.5272	-4.3864	5.0864	9.1061	-6.4239	0.0841	0.1732

converges to SZD (4.54). Therefore, the stability of the closed-loop dynamics (CLD1-3) also implies the stability of the Switching Zero-Dynamics (SZD1-3).

The stability in Touch-down phase is verified by CLD1-3. Angular positions and velocities in Table 4.5.1 at $t = 0.2867$ s indicate $\sigma(0) = -0.1620\ kgm^2s^{-1}$ and $\theta_1(0) = 0.1063$ rad. Table 4.5.1 shows the V_{xcm}^{max} and V_{ID}^{max} values. It can be verified that CLD1-2 are satisfied. Fig 4.13 shows the plots for θ_1 vs. σ and κ_3 vs. σ with $K_4 = 40000$, $K_5 = 800$ and $\epsilon = 0.1$. It is seen that all the time $\theta_1 < \kappa_3$ i.e. $x_{cm}(\theta_a) >$

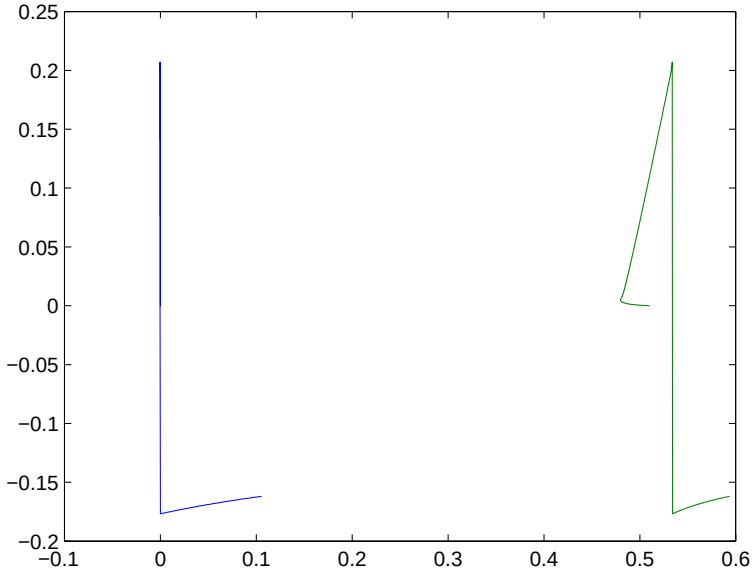

Figure 4.13: θ_1 vs. σ (dotted) and κ_3 vs. σ (solid).

0. CLD3 is satisfied as θ_1 converges to the stable equilibrium point $(-0.000021, 0)$ with time. The conditions CLD1-3, for the stability of Touch-down phase closed-loop dynamics, are satisfied.

4.5.2 Jumping Experiment on BRAIL 2.0

For jumping gait realization, actuators (in section 4.1.1) are operated in torque control mode ('endless turn mode'). The input torques to the actuators are computed based on the control law (4.43). The control law (4.43) computes torques inputs at ankle, knee and hip. The Ankle, knee and hip joints have two actuators each, one placed at each leg. The actuator inputs are half the joint torques computed by the control law (4.43).

Control law (4.43) uses the bipedal dynamics and computation of bipedal dynamics needs the joint angular position and velocity feedbacks. Controller (in section 4.1.1) reads the feedbacks from the actuators and computes the biped dynamics at each sampling instant. Controller sampling time is 0.01 s i.e., controller applies the control input (4.43) to the actuators at an interval of 0.01 s. The controller gains are chosen as it is described in simulation. The control inputs change according to the change in desired joint angular positions from $\theta_{bs}^{d}(t)$ to $\theta_{bf}^{d}(t)$ at $t = 0.15$ s, and $\theta_{bf}^{d}(t)$ to $\theta_{bl}^{d}(t)$ at $t = 0.29$ s. The torque inputs are read from the actuator 'load' feedback at each sampling instant and are plotted in Fig. 4.14. The torque reading are collected from joint actuators (ankle, knee and hip) both from the right and left legs at each sampling instant. Fig. 4.14 (a) ((b) and (c)) shows the experimental result as the sum of the 'load' reading of both the joint actuators placed at the ankle (knee and hip) of each leg.

The variations of joint angular positions and velocities for 1.5 s during jumping are shown in Figs. 4.15 and 4.16. The figures show the joint angular positions and velocities with control inputs as per (4.43). Joint angular position and velocity feedbacks are read from both right and left legs. As the reading from both the actuators placed at the ankle, knee and hippositions of the legs are almost equal, Figs. 4.15 and 4.16 show the reading from left leg actuators. Due to slow response-time of the actuators, certain deviations of the actual joint parameters from the simulated one can be noticed in the plot. However, the actual joint parameters of the bipeds closely follow the simulation results.

The biped's absolute orientation at $t = 0.15$ s (at the end of Take-off phase) is $\theta_a = [\ 0.19 \quad 1.90 \quad -0.62 \quad 0.35\ ]^T$ rad. The joint angular velocities

$\dot{\theta}_a = [\ 0.85 \quad -9.25 \quad 15.69 \quad -11.79\ ]^T$ rad/s at $t = 0.15$ s. θ_1 and $\dot{\theta}_1$ are computed from the internal dynamics (4.66) (by fourth order Runge-Kutta method with fixed step size of 0.01 s) using the measured actuator positions. The desired joint angular positions change from $\theta^d_{bs}(t)$ to $\theta^d_{bf}(t)$ at $t = 0.15$ s (Take-off phase to Flight phase).

In Flight phase, the joint angular positions and velocities for experimental and simulation results between $t = 0.15$ to $t = 0.29$ s are shown in Figs. 4.15 and 4.16. The deviations from actual and simulated angular positions and velocities are due to the slow actuator response. The biped's absolute orientation and joint angular velocities at $t = 0.30$ s (at the end of Flight phase) are $\theta_a = [\ 0.08 \quad 2.1162 \quad -0.741 \quad 0.3747\ ]^T$ rad and $\dot{\theta}_a = [\ -0.75 \quad -2.54 \quad 3.57 \quad -1.38\ ]^T$ rad/s. Impact takes place at around t =0.30 to 0.31 s (sensed by the sudden change in joint velocities). The joint velocities become $\dot{\theta}_a = [\ -1.35 \quad -3.58 \quad 4.50 \quad -1.90\ ]^T$ rad/s due the impact.

After the impact, $\sigma(0) = -0.1261\ kgm^2s^{-1}$ and $\theta_1(0) = 0.08$ rad. The the control inputs change at $t = 0.30$ s as desired joint angular positions change from $\theta^d_{bf}(t)$ to $\theta^d_{bl}(t)$ at $t = 0.30$ s (Flight phase to Touch-down phase). With control input (4.43) and the feedback gain $K_P = 9$, $K_D = 6$, $\epsilon = 0.1$, $V^{max}_{xcm} = 0$ and $V^{max}_{ID} = 0.00975\ kg^2m^4s^{-2}$. Therefore, the stability conditions CLD1 and CLD2 are satisfied which results in the stability of the Subsystem A. It can be noticed from the plots (Fig. 4.15 and 4.16) that the actual Touch-down phase angular positions and velocities closely follow the simulated ones.

With the desired gaits as per Table 4.5.1 and control input as per (4.43), the biped's jumping sequence is shown in Fig. 4.17. The maximum jumping height measured is ~ 0.025 m. The robot could jump backward by 0.004 m.

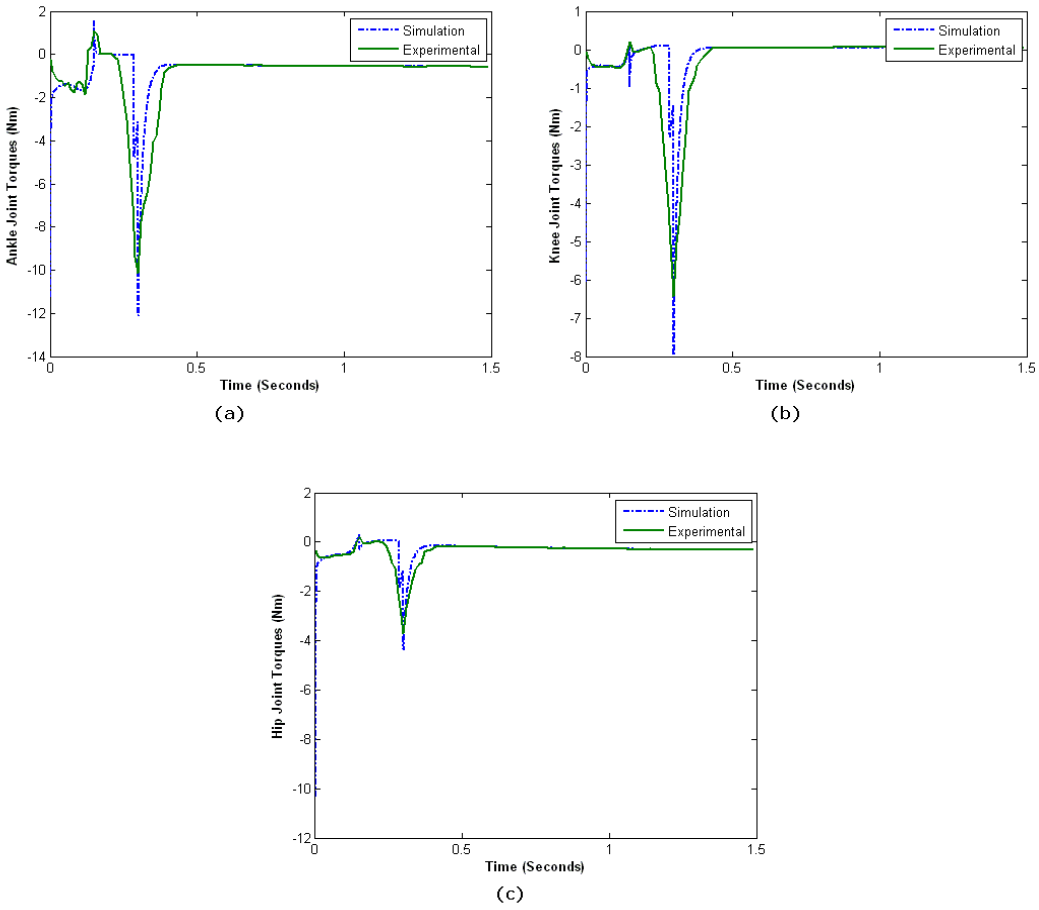

Figure 4.14: Variations of the joint torques in experimental and simulation studies: (a) τ_2, (b) τ_3 and (c) τ_4.

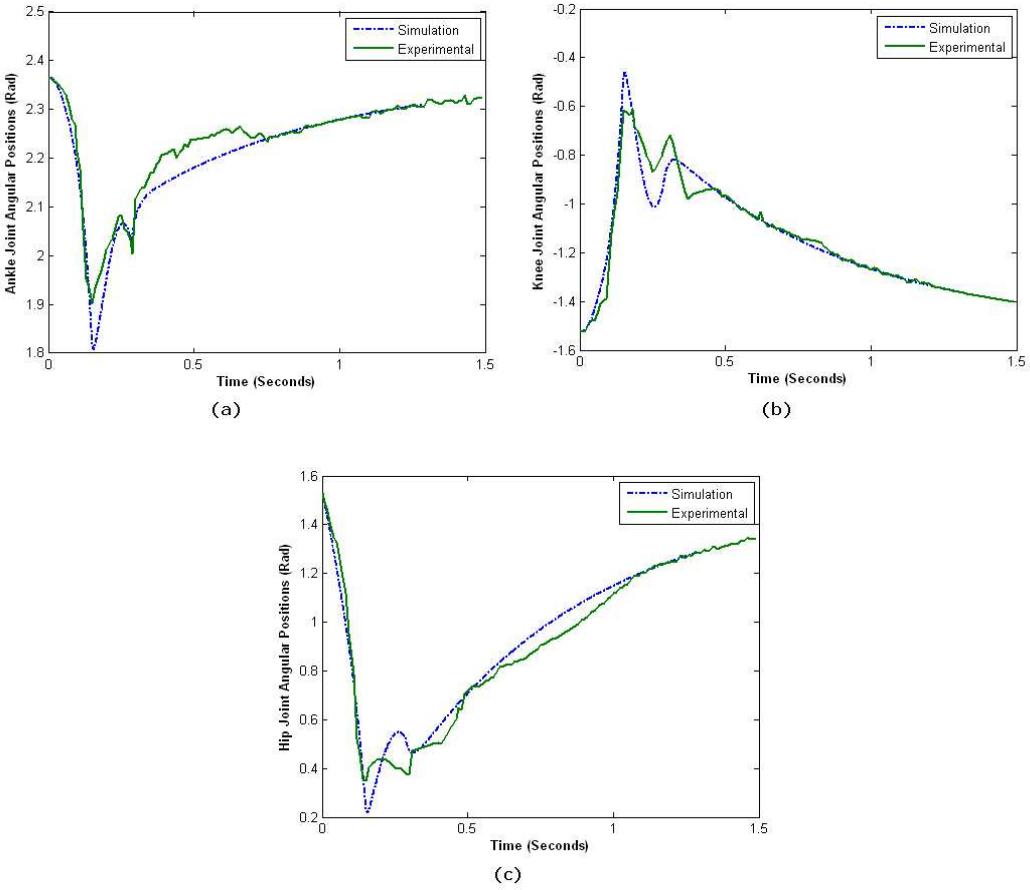

Figure 4.15: Variations of the joint angular positions in experimental and simulation studies: (a) θ_2, (b) θ_3 and (c) θ_4.

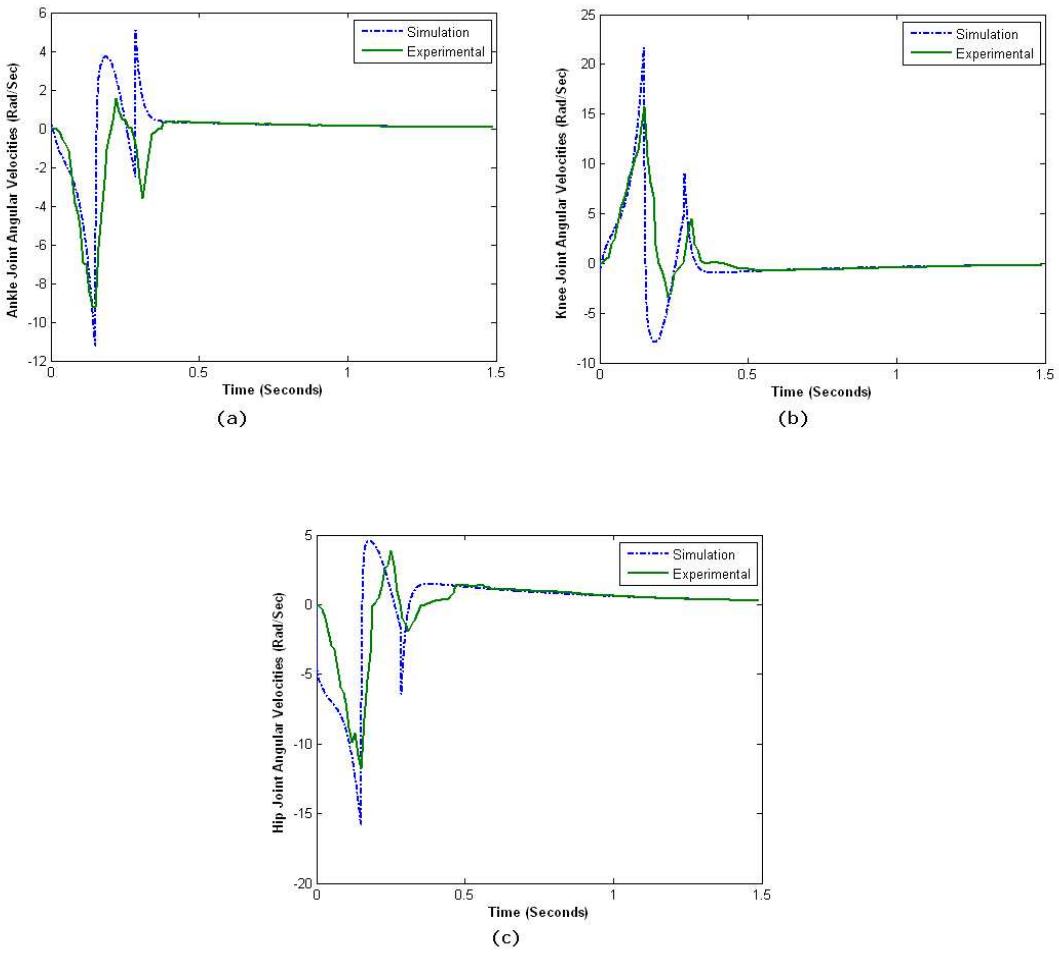

Figure 4.16: Variations of the joint angular velocities in experimental and simulation studies: (a) $\dot{\theta}_2$, (b) $\dot{\theta}_3$ and (c) $\dot{\theta}_4$.

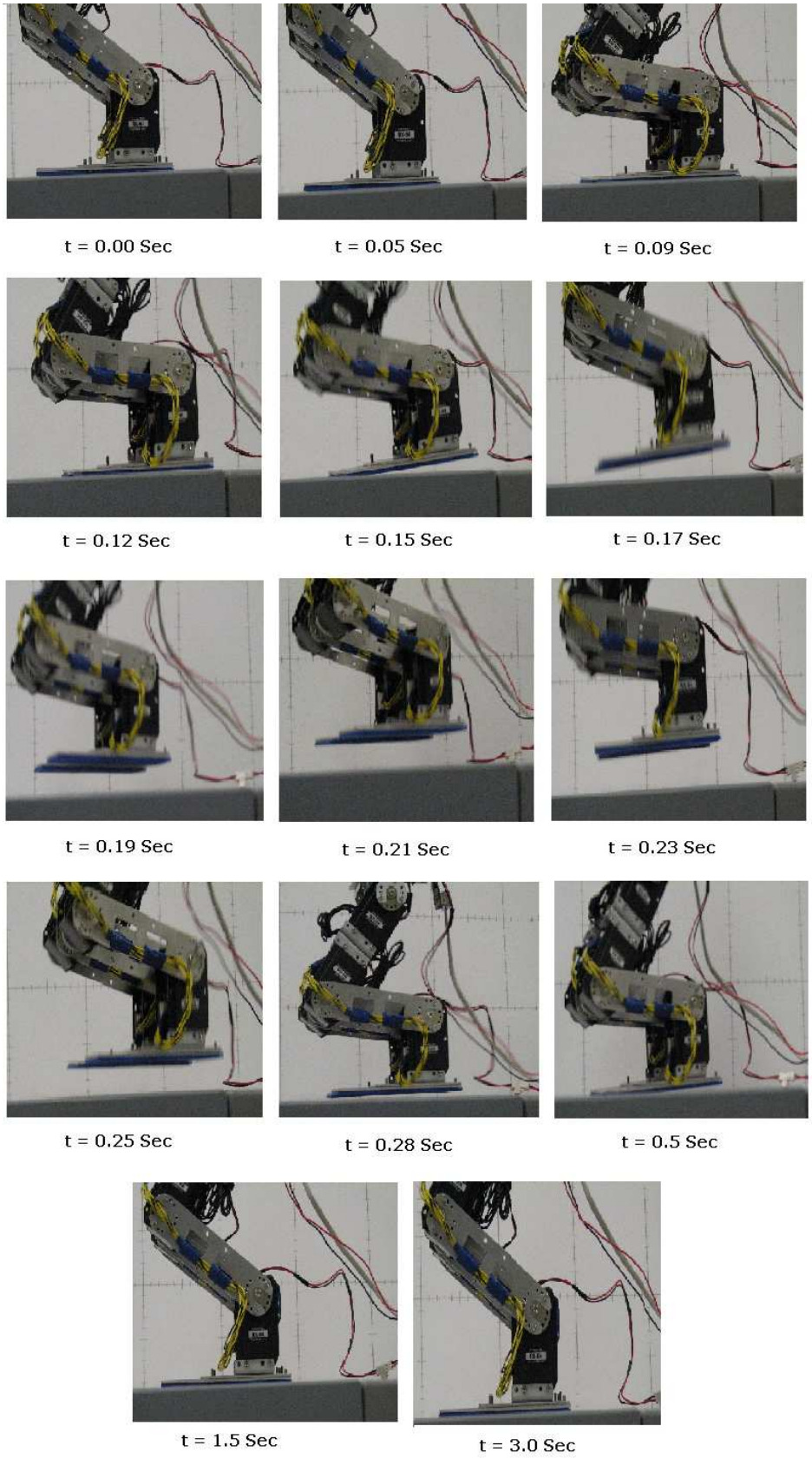

Figure 4.17: Jump Sequence with control input (4.43) and desired gait as per Table 4.5.1.

4.5.3 Comments on Simulations and Experimental Results

In Figs 4.14, 4.15 and 4.16, certain deviations of the actual input torques, joint positions and velocities from the simulation results are noticed. Following are the possible causes of such deviations.

- Actuator Time Constant: Considering the controller's sampling time of 0.01 s, the actuator time constant (0.002 to 0.006 s depending on the load) essentially introduces both actuation and measurement latency.
- Impact Model: The non-elasticity assumption on the impact model in Section 4.1.7 is not completely satisfied.
- Foot-Ground Contact Model: The estimated ranges of K_4 and K_5 might not be able to exactly model the behavior of the foot-ground contact surface. Moreover, jumping performance varies depending on the nature of the ground surface such as wooden or cemented. The experimentations in Section 4.5.2 are performed on a cemented surface.
- Sampling Time: The experimental results sometimes fail to capture certain features (i.e., exact peak values) of the simulated plots (with an integration step size of 0.0001 s) due to larger sampling time (0.01 s).
- Mismatches in Dynamic Parameters: The estimated biped parameters in Table 4.1 (using *Autodesk* and *Msc. Visualnastran*) might not be exact.

However, the actual input torques, joint positions and velocities could capture the key aspects related to the stability analysis discussed in Section 4.4. The biped's jumping performance, with stable landing, is quite close to the simulated results

(jumping height is almost the same as in simulation) even in presence of the mismatches between simulation and experimental environments. The following points are notable on the robustness of the controller.

- From the experimental data shown in Fig. 4.14, it is noticed that the actual control inputs are not exactly matching the simulated inputs. The biped could jump stably in spite of the difference between simulated and actual control inputs.

- Robustness in the controller can be quantified by the conditions CLD1-2. The controller parameters, K_P, K_D and ϵ, can be chosen such that the stability margin is more. As long as CLD1-3 are satisfied, the landing is stable even in presence of disturbances.

4.6 Conclusions

A planar, four-link robot model is considered in the study. The robot is underactuated by one DOF due to the passive DOF at the joint between the toe and ground. The foot compliance model with ground is considered as spring-damper system at the ankle and as a pivot at toe. The overall system dynamics behaves like a switching system. The jumping process is divided into three phases: Take-off, Flight and Touch-down. The controls for the three phases are formulated as an *output-zeroing* problem. The output functions in all the phases are selected such that the desired jumping performance is achieved with stable landing. Stability at the landing phase is governed by the Switching-Zero-Dynamics and Closed-Loop-Dynamics at the Touch-down phase. The stability conditions for the SZD and CLD in Touch-down phase

are established. *Critical potential index* and *critical kinetic index* are introduced to measure the stability margin of CLD while stability of SZD depends on certain properties of the bipedal structure and foot-ground contact surfaces. Jumping gait with stable landing is generated and experimented on the BRAIL 2.0 biped.

The choice of various jumping parameters are dependent on the dynamics of the biped. The validity of the jumping parameters is verified off-line. Therefore, the jumping gaits are computed off-line and implemented on the BRAIL 2.0 biped. The jumping performance is restricted by the maximum torque provided by the actuator.

4.6.1 Future Directions

The selection of desired jumping gaits (Section 4.3) involves the proper choice of a number of parameters, i.e. C_x, C_y, η^d, ζ^d and the various controller gains. In the current research, the selection of desired jumping gaits does not involve system dynamics. However, it would be an interesting direction to include dynamics in the selection process of desired gait parameters. It would be a multi-objective optimization problem to choose such parameters so as to meet a desired jumping performance, i.e. jumping height and length, effect of impact.

Chapter 5

Rotational Stability Index (RSI) Point: Postural Stability in Bipeds

ZMP is a widely used concept to analyze postural stability of legged systems [6]. The ZMP is the point on the ground where the resultant of moments acting on the legged system is zero. To maintain postural stability in legged systems the ZMP is kept within the area covered by the foot i.e., the support polygon [16, 79, 99]. Biped locomotion is normally considered with flat-foot while utilizing the ZMP-based stability criterion [16, 99].

The absolute orientation of the biped is considered as an additional passive DOF in point foot bipeds [7, 76, 87, 100]. As ZMP criterion is not applicable to point foot bipeds, the concepts of periodicity and orbital stability are useful while dealing with the associated stability issues [7, 11, 76]. By periodically attaining certain postures, even though statically unstable, orbital stability is achieved.

In the stability issues associated with the various gaits for bipeds with non-trivial foot size, one fundamental consideration is the possibility of rotation of the overall biped about the foot edge. This is termed as "rotational equilibrium" [10, 96]. Unbalanced moments at the foot leads to foot-rotation about a point on the foot boundary.

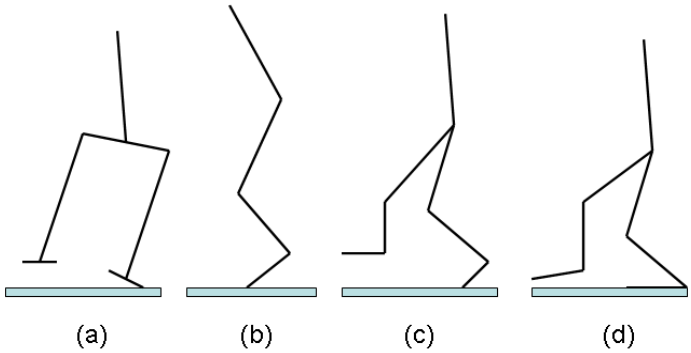

Figure 5.1: (a) Foot-Rotation in frontal plane (b) Foot-rotation in double-support phase (sagittal plane) (c) Foot-rotation in single-support phase (sagittal plane) (d) Foot-rotation in swinging leg (sagittal plane).

Foot-rotation is an important aspect to look into while addressing stable locomotion. The FRI point explains the occurrence of foot-rotation [10]. If the FRI point is outside the foot-print area, the foot rotates about certain point on the foot boundary. The foot-rotation changes the absolute orientation of the biped bringing in a passive DOF which makes the bipedal systems *underactuated*. Foot/feet rotation can occur both in single-support and double-support phases (Fig. 5.1 (a), (b)).

The ground reference points such as ZMP and FRI use ground reaction force (GRF) for their evaluation. The locations of such ground reference points depend on the distribution of GRF at the foot/ground contact surface. When foot is rotated, GRF acts on the point about which the foot is rotating. ZMP/FRI fails to indicate the stability aspects in such situations. Hence, foot-rotation is often noted to reflect a loss of stability in biped locomotion and is dealt by preventing foot-rotation [9,10,97].

Foot-rotation during locomotion does not essentially indicate postural imbalance of the biped. The biped can still be stable even in the presence of foot-rotation. The configuration, when foot is rotated about the edge, is commonly referred as tiptoe

configuration (Fig. 5.1 (a), (b), (c)). The biped with rotated foot often becomes *underactuated*. In some scenarios, the biped is fully-actuated even in the presence of foot-rotation. Fig. 5.1 (d) shows such an example where foot-rotation occurs in swinging leg. Postural stability of fully actuated bipeds is commonly analyzed by ZMP or FRI criteria [10, 16, 99, 101]. In this research, the stability aspects of underactuated bipeds are looked into. A novel stability concept *rotational stability* is introduced to analyze the stability in such bipedal postures. The rotational stability investigates whether the bipedal posture would lead to a flat-foot posture from a particular underactuated configuration with foot-rotation. A ground reference point 'Rotational Stability Index (RSI)' point is proposed to measure the degree of *rotational stability*. Conditions are established based on the RSI point to analyze postural stability during bipedal locomotion. The stability conditions in presence of foot-rotation are validated on a biped robot.

Section 5.1 describes the planar biped model and the computation of the associated dynamics. Section 5.1.3 investigates the stability aspects of the biped robot using the dynamics computed in section 5.1. The concepts of *rotational stability* and RSI point are introduced in section 5.2. Section 5.2.1 discusses the *rotational stability* in perspective of planar two-link model discussed in section 5.1. Section 5.3 explains the RSI point based criterion to analyze stability in bipedal locomotion. Various simulations and experimentations are described in Section 5.4 and conclusions are drawn in Section 5.5.

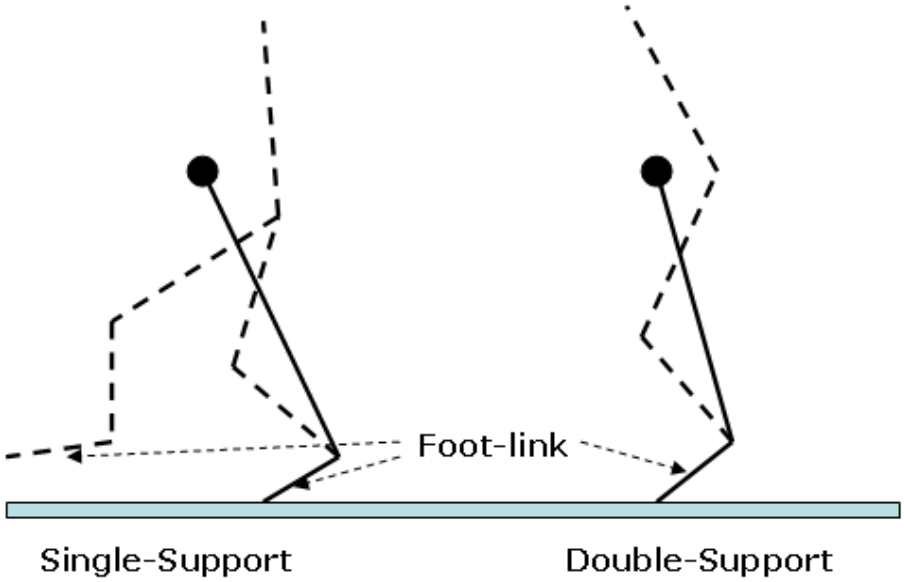

Figure 5.2: Tiptoe Model.

5.1 Planar Biped: Two-link model

While considering foot-rotation during locomotion, a planar biped can be modeled as a two-link model (Fig. 5.2). The model considers the rotating foot as a link i.e., the foot link. The ankle joint connects the foot link and the rest of the biped. The rest of the biped is represented by a concentrated mass located at the center of mass of the rest of the biped. The line connecting the ankle of the rotating foot and the center of mass of the rest of the biped (except the rotating foot) is considered as another link i.e., the body link.

The two-link bipedal model is shown in Fig. 5.3. The Foot length is l_1. The biped is rotated about the foot-edge by an angle θ_1. The length of the body link is l_b. The body link makes an angle of θ_2 with the foot. Let the masses of the foot and rest of the biped be m_f and m_b respectively, and the total mass of the biped is m. The

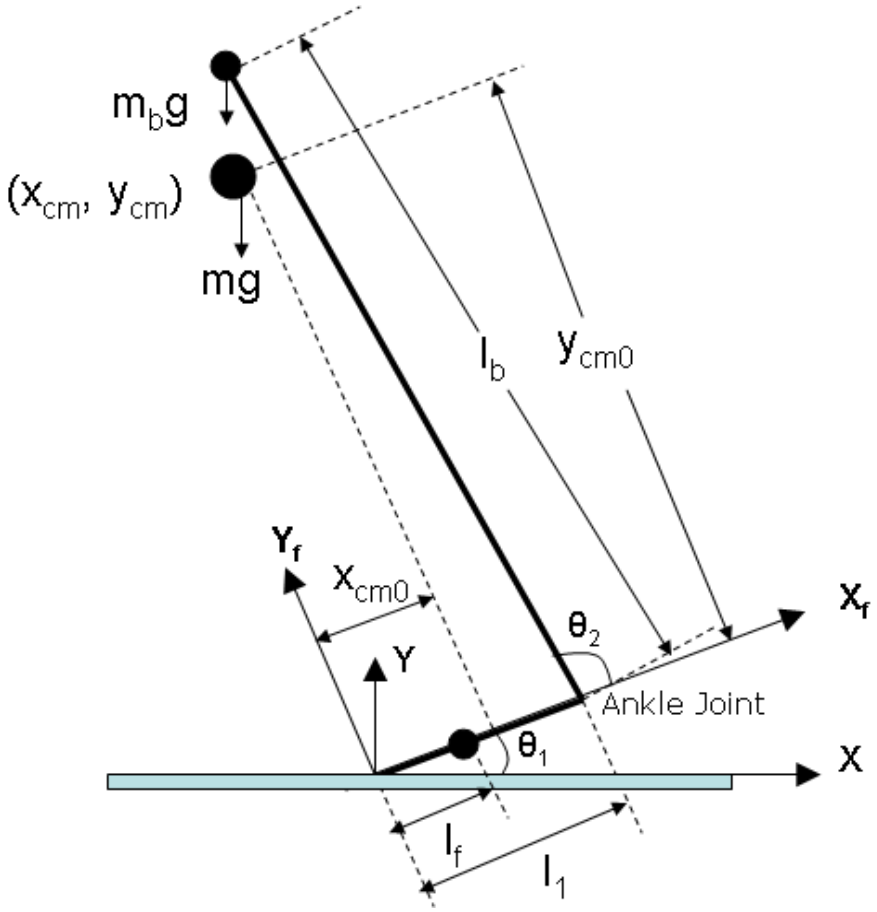

Figure 5.3: Tiptoe Configuration: Two-link model.

center of mass of the foot-link is located at a distance of l_f from the point of rotation. The biped's center of mass (CM) $(x_{cm}(\theta), y_{cm}(\theta))$ with respect to world coordinate (X, Y) is expressed as (5.1) where $\theta = [\theta_1, \theta_2]^T$.

$$\begin{aligned}
x_{cm}(\theta) &= \frac{m_f l_f cos(\theta_1) + m_b(l_1 cos(\theta_1) + l_b cos(\theta_1 + \theta_2))}{m}, \\
&= \frac{(m_f l_f + m_b l_1)cos(\theta_1) + m_b l_b cos(\theta_1 + \theta_2)}{m}, \\
&= x_{cm0}(\theta_2)cos(\theta_1) - y_{cm0}(\theta_2)sin(\theta_1), \\
&= \sqrt{x_{cm0}^2(\theta_2) + y_{cm0}^2(\theta_2)}sin(tan^{-1}(\frac{x_{cm0}(\theta_2)}{y_{cm0}(\theta_2)}) - \theta_1), \\
y_{cm}(\theta) &= \sqrt{x_{cm0}^2(\theta_2) + y_{cm0}^2(\theta_2)}cos(tan^{-1}(\frac{x_{cm0}(\theta_2)}{y_{cm0}(\theta_2)}) - \theta_1). \qquad (5.1)
\end{aligned}$$

Where $(x_{cm0}(\theta_2), y_{cm0}(\theta_2))$ is the biped's CM with respect to the (X_f, Y_f) coordinate (5.2).

$$\begin{aligned}
x_{cm0}(\theta_2) &= \frac{m_f l_f + m_b(l_1 + l_b cos(\theta_2))}{m}, \\
y_{cm0}(\theta_2) &= \frac{m_b l_b sin(\theta_2)}{m}. \qquad (5.2)
\end{aligned}$$

5.1.1 Dynamics

The dynamics of the two-link model has the form shown in (5.3) [4]. M_{ij} is an element of the inertial matrix, $V_i(.)$ are the coriolis and centrifugal forces and $G_i(.)$ are the gravitational term.

$$\begin{bmatrix} M_{11}(\theta_2) & M_{12}(\theta_2) \\ M_{21}(\theta_2) & M_{22}(\theta_2) \end{bmatrix} \begin{bmatrix} \ddot{\theta}_1 \\ \ddot{\theta}_2 \end{bmatrix} + \begin{bmatrix} V_1(\dot{\theta}_1, \dot{\theta}_2)\dot{\theta}_2 \\ V_2(\dot{\theta}_1) \end{bmatrix} + \begin{bmatrix} G_1(\theta) \\ G_2(\theta) \end{bmatrix} = \begin{bmatrix} 0 \\ \tau \end{bmatrix}. \qquad (5.3)$$

It is notable that the inertia matrix is independent of θ_1. There is no torque applied at the joint between toe and ground making the biped *underactuated*. τ is the effective torque of the externally applied torques at different joints of the biped.

5.1.2 Internal Dynamics

The second row of (5.3) shows that θ_2 can be controlled using *input-output linearization* [8] or *output-zeroing* technique [77] (discussed in section 1.3). The part of biped dynamics shown in (5.4) remains "unobservable" in such techniques. Precisely, if output function is chosen as $h(\theta) = \theta_2$, (5.4) is the *internal dynamics* of the biped.

$$M_{11}(\theta_2)\ddot{\theta}_1 + M_{12}(\theta_2)\ddot{\theta}_2 + V_1(\dot{\theta}_1, \dot{\theta}_2)\dot{\theta}_2 + G_1(\theta_1, \theta_2) = 0. \tag{5.4}$$

The postural stability of biped structure with rotated foot is governed by the internal dynamics shown in (5.4). The boundedness of the internal dynamics is essential for the postural stability of the biped.

5.1.3 Postural Stability

During biped locomotion, foot-rotation may occur both in forward or backward directions and θ_2 varies depending on the nature of bipedal gait. The following sections investigate the stability aspects of forward foot-rotation with $\dot{\theta}_2 = 0$. The analysis is further extended in section 5.3 to establish the generic stability conditions in biped locomotion.

To investigate the stability of a bipedal posture with forward foot-rotation and $\dot{\theta}_2 = 0$, we explore the stability aspects of the corresponding internal dynamics. The

postural stability analysis investigates what is going to happen to a particular bipedal posture with $\theta_2 = \theta_2^*$. For such analysis, $\theta_2 = \theta_2^*$, $\dot{\theta}_2 = 0$, and $\ddot{\theta}_2 = 0$ in (5.4) leading the internal dynamics to (5.5).

$$M_{11}(\theta_2^*)\ddot{\theta}_1 + G_1(\theta_1, \theta_2^*) = 0. \tag{5.5}$$

The expression of $G_1(\theta)$ is as (5.6) [4].

$$G_1(\theta) = mgx_{cm}(\theta). \tag{5.6}$$

Putting (5.6) into (5.5) and considering the two states as θ_1 and σ where σ is defined by (5.7), the state model of the biped internal dynamics can be derived.

$$\sigma(t) = -\int_0^t mgx_{cm}(\theta)dt. \tag{5.7}$$

σ is the angular momentum of the bipedal system about the point of rotation [3]. Utilizing (5.1), the biped internal dynamics for a particular posture has the form as per (5.8).

$$\begin{aligned} \dot{\theta}_1 &= \frac{\sigma}{M_{11}(\theta_2^*)}, \\ \dot{\sigma} &= -mgx_{cm}(\theta_1, \theta_2^*) \\ &= mg\sqrt{x_{cm0}^2(\theta_2^*) + y_{cm0}^2(\theta_2^*)}sin(tan^{-1}(\theta_1 - \frac{x_{cm0}(\theta_2^*)}{y_{cm0}(\theta_2^*)})). \end{aligned} \tag{5.8}$$

Let us the define the following three positive constants[1],

[1]Units of constants are same as shown in (5.9) throughout the chapter.

$$\begin{aligned} K_1 &= \frac{1}{M_{1,1}(\theta_2^*)}\ kg^{-1}m^{-2}, \\ K_2 &= mg\sqrt{x_{cm0}^2(\theta_2^*) + y_{cm0}^2(\theta_2^*)}\ Nm, \\ K_3 &= tan^{-1}(\frac{x_{cm0}(\theta_2^*)}{y_{cm0}(\theta_2^*)})\ rad. \end{aligned} \tag{5.9}$$

Utilizing (5.9), internal dynamics becomes as per (5.10).

$$\begin{aligned} \dot{\theta}_1 &= K_1\sigma, \\ \dot{\sigma} &= K_2 sin(\theta_1 - K_3). \end{aligned} \tag{5.10}$$

The phase portrait of (5.10) is shown in Fig. 5.4. The internal dynamics (5.10) has one equilibrium point $(\theta_1, \sigma) = (K_3, 0)$ for $0 < \theta_1 < \pi$. In the flat-foot configurations $\theta_1 = 0$. In the tiptoed biped $\theta_1 > 0$ which indicates forward foot-rotation. When the foot rotates about the other end of the foot (other than toe) $\theta_1 < 0$.

Qualitative Behavior near Equilibrium Point

The qualitative behavior of a nonlinear system near an equilibrium point can be determined via. *linearization* with respect to that point [98]. Linearization of (5.10) around the equilibrium point $(K_3, 0)$ gives (5.11). The linearized internal dynamics (5.11) has two poles $\lambda_{1,2} = \pm\sqrt{K_1K_2}$. The equilibrium point is a *saddle point* [98] and the phase portrait indicates the nature of the equilibrium point (Fig. 5.4). The unstable pole $+\sqrt{K_1K_2}$ makes the equilibrium point *unstable* [98] (*using Lyapunov's indirect method*).

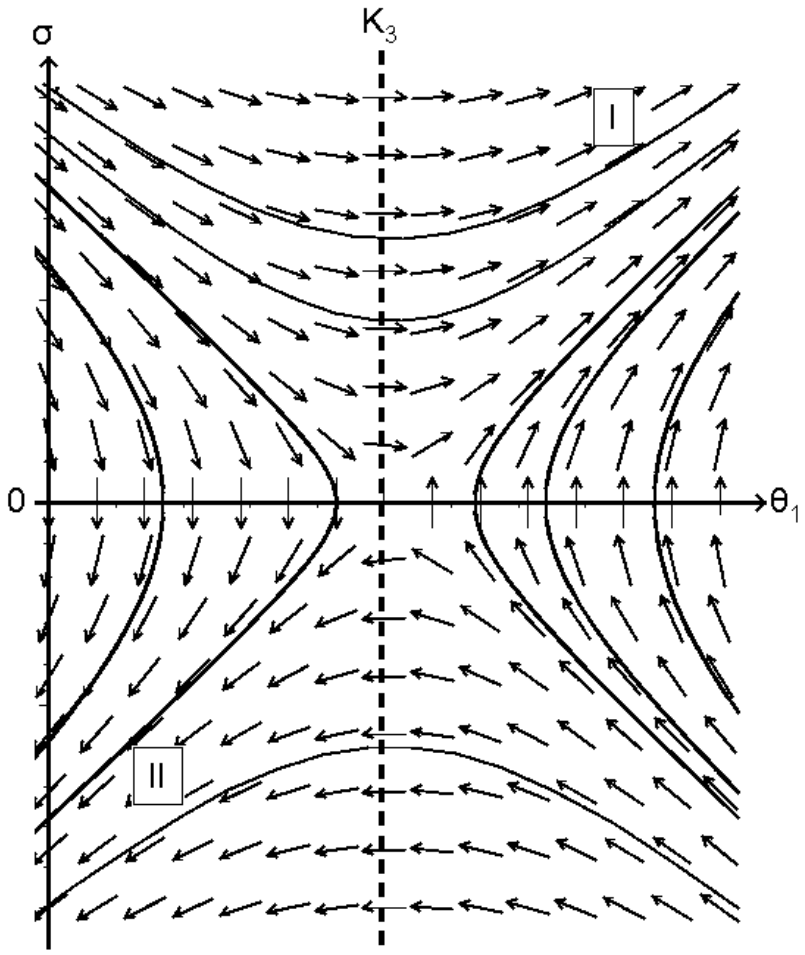

Figure 5.4: Phase Portrait of (5.10). Trajectory I: Member of the set of trajectories going out with increasing θ_1. Trajectory II: Member of the set of trajectories reaching the $\theta_1 = 0$ plane.

$$\begin{bmatrix} \Delta\theta_1 \\ \Delta\sigma \end{bmatrix} = \begin{bmatrix} 0 & K_1 \\ K_2 & 0 \end{bmatrix} \begin{bmatrix} \theta_1 \\ \sigma \end{bmatrix}. \tag{5.11}$$

A stationary tiptoed biped is *statically* stable only in certain specific scenarios, for example, when initial conditions of the internal dynamics (5.10) is the equilibrium point $(K_3, 0)$. However, it is seen from the phase portrait (Fig. 5.4) that with any arbitrary initial conditions (expect $(K_3, 0)$) the vector fields never converge to the equilibrium point. The equilibrium point $(K_3, 0)$ being unstable by nature, such bipedal configurations are not posturally stable.

5.2 Rotational Stability and Rotational Stability Index (RSI) Point

It is shown in Section 5.1.3 that the stationary tiptoed biped is not posturally stable i.e., unable to maintain such posture for a long time. While the biped is in motion, such tiptoed configurations can lead to either a flat-foot posture or toppling over of the biped. To formally analyze such stability of the bipeds, a term *rotational stability* is introduced.

Definition 5.2.1. *A bipedal posture is 'rotational stable' if the particular posture leads to a flat-foot posture with time.*

Physical significance of the *rotational stability* is explained in Fig. 5.5. A particular bipedal posture goes to a flat-foot posture when it is *rotational stable* and topples over when it is not. To quantify the *rotational stability* of bipedal systems, a ground reference point 'Rotational Stability Index (RSI) Point' is introduced.

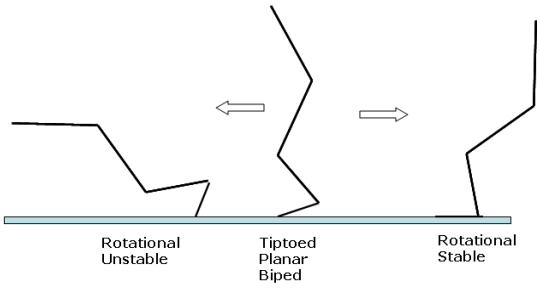

Figure 5.5: *Rotational Stability.*

Definition 5.2.2. *The point on the foot/ground contact surface, where the resultant force acts on the body, is defined as Rotational Stability Index point.*

The "resultant force" is mainly contributed by the gravitational components and the biped's angular momentum and not the ground reaction forces. The concept of *rotational stability* and RSI points are illustrated in subsequent sections. The RSI point and its significance are explored for planar biped robots in Section 5.2.1. The concepts can be extended to three dimensional structure. The RSI point is established as a stability criteria in biped locomotion in Section 5.3.

5.2.1 Planar Bipeds and Rotational Stability

A tiptoed bipedal posture can be represented by a combination of θ_1 and θ_2 (Section 5.1). With $\theta_2 = \theta_2^*$, the "unobservable" dynamics of the planar biped is given by (5.10). Therefore, the stability analysis for such bipeds can be performed by analyzing the stability issues associated with (5.10).

From the states (θ_{10}, σ_0), corresponding to physically reasonable biped configurations, if the solution vector of (5.10) reaches $\theta_1 = 0$ plane (Fig. 5.4) with time, then the bipedal posture is *rotational stable*. The RSI point (x_{RSI}, y_{RSI}) for such planar

biped is defined as (5.12).

$$\begin{aligned} x_{RSI} &= x_{cm}(\theta_{10}, \theta_2^*) - \frac{\sigma_0}{mg}\sqrt{\frac{K_1 K_2(1 + cos(K_3 - \theta_{10}))}{2}}, \\ y_{RSI} &= 0. \end{aligned} \tag{5.12}$$

As mentioned in the Definition 5.2.2, the resultant force on the biped acts on the ground reference point $(x_{RSI}, 0)$. As the resultant force acts at $(x_{RSI}, 0)$, the tiptoed biped experiences a moment which depends on the location of the RSI point i.e., x_{RSI}. Hence, the *rotational stability* depends on the value of x_{RSI}. Dependency of *rotational stability* of a tiptoed biped on the RSI point is investigated in the following analysis.

Lemma 5.2.1. *Consider (5.3) and (5.10) of planar bipeds. For states (θ_{10}, σ_0) corresponding to physically reasonable biped configurations, and the RSI point $(x_{RSI}, 0)$, statements (A) and either part (a) or (b) of statement (B) are true:*

(A) $x_{RSI} > 0$

(B) **(a)** $K_3 > \theta_{10}$ *and*
$\sigma_0 < \sqrt{\frac{2K_2}{K_1}(1 - cos(\theta_{10} - K_3))}$,

(b) $K_3 \leq \theta_{10}$ *and*
$\sigma_0 < -\sqrt{\frac{2K_2}{K_1}(1 - cos(\theta_{10} - K_3))}$.

Proof. From (5.1), $x_{cm}(\theta)$ can be rewritten for a specific biped posture as (5.13).

$$x_{cm}(\theta_1, \theta_2^*) = \frac{K_2}{mg} sin(K_3 - \theta_1). \tag{5.13}$$

Using (5.12) and (5.13), statement (A) gives,

$$x_{cm}(\theta_{10}, \theta_2^*) \quad -\frac{\sigma_0}{mg}\sqrt{\frac{K_1K_2(1+cos(K_3-\theta_{10}))}{2}} > 0$$

$$\implies \qquad \sigma_0 < \sqrt{\frac{2K_2}{K_1}}\frac{sin(K_3-\theta_{10})}{\sqrt{(1+cos(\theta_{10}-K_3))}}. \tag{5.14}$$

For part (a) of statement (B) $K_3 > \theta_{10}$,

$$\begin{aligned}\frac{sin(K_3-\theta_{10})}{\sqrt{(1+cos(\theta_{10}-K_3))}} &= \frac{\sqrt{(1-cos^2(K_3-\theta_{10}))}}{\sqrt{(1+cos(\theta_{10}-K_3))}} \\ &= \sqrt{(1-cos(\theta_{10}-K_3))}. \end{aligned} \tag{5.15}$$

Using (5.14) and (5.15), it is seen that statement (A) and part (a) of statement (B) are true when $K_3 > \theta_{10}$.

For part (b) of statement (B) $K_3 \leq \theta_{10}$,

$$\begin{aligned}\frac{sin(K_3-\theta_{10})}{\sqrt{(1+cos(\theta_{10}-K_3))}} &= -\frac{\sqrt{(1-cos^2(\theta_{10}-K_3))}}{\sqrt{(1+cos(\theta_{10}-K_3))}} \\ &= -\sqrt{(1-cos(\theta_{10}-K_3))}. \end{aligned} \tag{5.16}$$

Using (5.14) and (5.16), it is seen that statement (A) and part (b) of statement (B) are true when $K_3 \leq \theta_{10}$. □

Theorem 5.2.2. *Consider (5.3) and (5.10) of planar bipeds and* $(\theta_{10}, \sigma_0) \neq (K_3, 0)$ *being the values of the states corresponding to physically reasonable biped configurations. The bipedal posture is rotational stable if the location of the RSI point* $(x_{RSI}, 0)$ *is such that* $x_{RSI} > 0$.

Proof. Consider (5.10) with values of the states $(\theta_{10}, \sigma_0) \neq (K_3, 0)$. Using Lemma 5.2.1, it can be stated that when $x_{RSI} > 0$,

(I) $K_3 > \theta_{10}$ and $\sigma_0 < \sqrt{\frac{2K_2}{K_1}(1 - cos(\theta_{10} - K_3))}$

(II) $K_3 \leq \theta_{10}$ and $\sigma_0 < -\sqrt{\frac{2K_2}{K_1}(1 - cos(\theta_{10} - K_3))}$

Therefore, *Theorem* 5.2.2 can be proved if it is shown that from a given posture with initial conditions $(\theta_{10}, \sigma_0) \neq (K_3, 0)$, the solution vector of (5.10) reaches $\theta_1 = 0$ plane when either statement I or II is true.

From (5.10),

$$\begin{aligned} \frac{d\sigma}{d\theta_1} &= \frac{K_2 sin(\theta_1 - K_3)}{K_1 \sigma}, \\ \sigma d\sigma &= \frac{K_2}{K_1} sin(\theta_1 - K_3) d\theta_1, \\ \frac{\sigma_0^2}{2} &= \frac{\sigma^2}{2} + E_\sigma(\theta_1), \\ \sigma_0^2 &= \sigma^2 + 2E_\sigma(\theta_1), \end{aligned} \tag{5.17}$$

where $E_\sigma(\theta_1)$ is defined as follows:

$$\begin{aligned} E_\sigma(\theta_1) &= -\int_{\theta_{10}}^{\theta_1} \frac{K_2}{K_1} sin(\theta_1 - K_3) d\theta_1, \\ &= \frac{K_2}{K_1}(cos(\theta_1 - K_3) - cos(\theta_{10} - K_3)). \end{aligned} \tag{5.18}$$

The maximum value of $E_\sigma(\theta_1)$ in (5.18) occurs when $\theta_1 = K_3$. The corresponding maximum value is denoted by E_σ^{max} which is calculated by putting $\theta_1 = K_3$ in (5.18).

$$E_\sigma^{max} = \frac{K_2}{K_1}(1 - cos(\theta_{10} - K_3)). \tag{5.19}$$

Equation (5.17) shows that if $\mid \sigma_0 \mid > \sqrt{2E_\sigma^{max}}$, $\sigma = 0$ does not exists in the σ trajectory. Because $\mid \sigma_0 \mid \not> \sqrt{2E_\sigma^{max}}$ at $\sigma = 0$. Similarly, $\mid \sigma_0 \mid < \sqrt{2E_\sigma^{max}}$ indicates the existence of $\sigma = 0$ i.e., zero-crossing in the σ trajectory. Depending on the values of (θ_{10}, σ_0), there can be four possible cases with $\theta_{10} > 0$ (Fig. 5.4).

(a) With $K_3 > \theta_{10}$ and $\sigma_0 > 0$, the trajectories of (5.10) reach $\theta_1 = 0$ plane if there exists a zero-crossing in the σ trajectory. The zero-crossing exists when $\mid \sigma_0 \mid < \sqrt{2E_\sigma^{max}}$ i.e., $\sigma_0 < \sqrt{2E_\sigma^{max}}$ for $\sigma_0 > 0$.

(b) With $K_3 > \theta_{10}$ and $\sigma_0 < 0$, the trajectories of (5.10) always reach $\theta_1 = 0$ plane.

(c) With $K_3 \leq \theta_{10}$ and $\sigma_0 > 0$, the trajectories of (5.10) never reach $\theta_1 = 0$.

(d) With $K_3 \leq \theta_{10}$ and $\sigma_0 < 0$, the trajectories of (5.10) reach $\theta_1 = 0$ plane if there is no zero-crossing in the σ trajectory. Zero-crossing exists if $\mid \sigma_0 \mid > \sqrt{2E_\sigma^{max}}$ i.e., $\sigma_0 < -\sqrt{2E_\sigma^{max}}$ for $\sigma_0 < 0$.

Cases (a) and (b) prove *Theorem* 5.2.2 when (I) is true while cases (c) and (d) prove *Theorem* 5.2.2 when (II) is true. □

5.2.2 CM criteria for Rotational Stability

Suppose $(x_{cm}(\theta_1, \theta_2^*), y_{cm}(\theta_1, \theta_2^*)) = (\chi, \psi)$ and $x_{cm}(\theta_{10}, \theta_2^*) = \chi_0$. Hence,

$$\begin{aligned}
\chi &= -\frac{K_2}{mg} sin(\theta_1 - K_3), \\
\dot{\chi} &= -\psi\dot{\theta}_1 \ \textit{(Time derivative)}, \\
\chi d\chi &= -\chi\psi d\theta_1, \\
\chi^2 &= \chi_0^2 - 2\int_{\theta_{10}}^{\theta_1} \chi\psi d\theta_1, \\
\chi_0^2 &= \chi^2 + 2E_\chi,
\end{aligned} \tag{5.20}$$

where $E_\chi = \int_{\theta_{10}}^{\theta_1} \chi\psi d\theta_1$.

Lemma 5.2.3. *Consider (5.3) and (5.10) of planar bipeds. For the states* (θ_{10}, σ_0) *with* $(x_{cm}(\theta_1, \theta_2^*), y_{cm}(\theta_1, \theta_2^*)) = (\chi, \psi)$ *and* $x_{cm}(\theta_{10}, \theta_2^*) = \chi_0$*, corresponding to physically reasonable biped configurations, the following two statements are equivalent:*

(A) $\chi_0 > \sqrt{2E_\chi^{max}}$

(B) $\sigma_0 < \sqrt{\frac{2K_2}{K_1}(1 - cos(\theta_{10} - K_3))}$

Similarly, the following two statements are equivalent:

(C) $0 > \chi_0 > -\sqrt{2E_\chi^{max}}$

(D) $\sigma_0 < -\sqrt{\frac{2K_2}{K_1}(1 - cos(\theta_{10} - K_3))}$

where E_χ^{max} *is the maximum value of* E_χ*.*

Proof. As per equation (5.20), χ will not change sign if $\chi_0 > \sqrt{2E_\chi^{max}}$. When $\chi_0 > \sqrt{2E_\chi^{max}}$, it is seen from (5.13) that $K_3 > \theta_{10}$. Hence, as χ never changes sign, $K_3 > \theta_{10}$ should be always true. E_χ^{max} occurs at $\theta_1 = K_3$. However, if statement (B) is not true, then $K_3 > \theta_{10}$ is not true always (see Fig. 5.4 and proof of *Theorem*) 5.2.2. Hence, the statement (B) is also true when (A) is true. Therefore, statement (A) and (B) are equivalent. Similar proof is possible to show the equivalence of statement (C) and (D). □

With the states $(\theta_{10}, \sigma_0) \neq (K_3, 0)$, corresponding to physically reasonable biped configurations, the biped is *rotational stable* if either statements (A) or (C) of Lemma 5.2.3 is true. It can be noted that the such criterion on CM is equivalent to the stability criterion mentioned in *Theorem* 5.2.2 (*Using Lemma* 5.2.1 and 5.2.3).

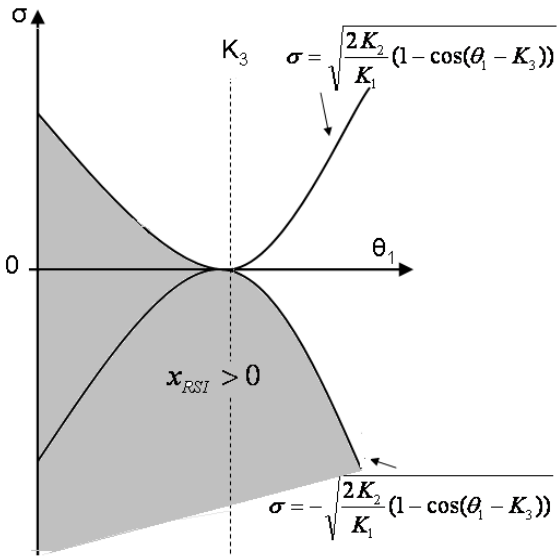

Figure 5.6: RSI point and Phase Portrait.

REMARK. The two loci for $\sigma = \sqrt{\frac{2K_2}{K_1}(1 - cos(\theta_{10} - K_3))}$ and $\sigma = -\sqrt{\frac{2K_2}{K_1}(1 - cos(\theta_{10} - K_3))}$ are shown in Fig. 5.6. $x_{RSI} > 0$ in any bipedal posture corresponding to the shaded area in Fig. 5.6. Hence, the shaded area corresponds the *rotational stable* postures.

When $K_3 > \theta_{10}$, the value of σ_0, for which $\sigma = 0$ and $\theta_1 = K_3$ occur simultaneously, corresponds to $E_\sigma^{max} = \frac{\sigma_0^2}{2}$ (from (5.17) and (5.18)). For $K_3 > \theta_{10}$, the minimum value of θ_{10}, for which the trajectory reaches $\theta_1 = K_3$ plane, corresponds to $E_\chi^{max} = \frac{1}{2}\frac{K_2^2}{(mg)^2} sin^2(K_3 - \theta_{10})$ (from (5.20) and (5.13)). σ_0 and θ_{10} corresponding to E_σ^{max} and E_χ^{max} lie on the two loci shown in Fig. 5.6.

5.2.3 Discussions on the RSI Point

Some useful notes on RSI point:

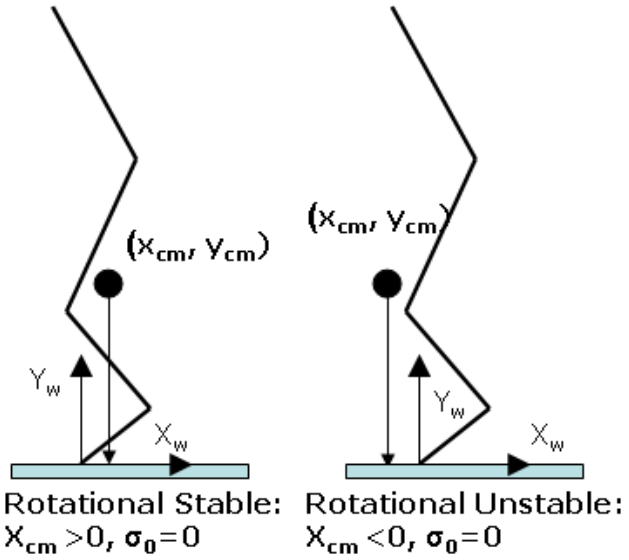

Figure 5.7: *Rotational Stability* for stationary biped.

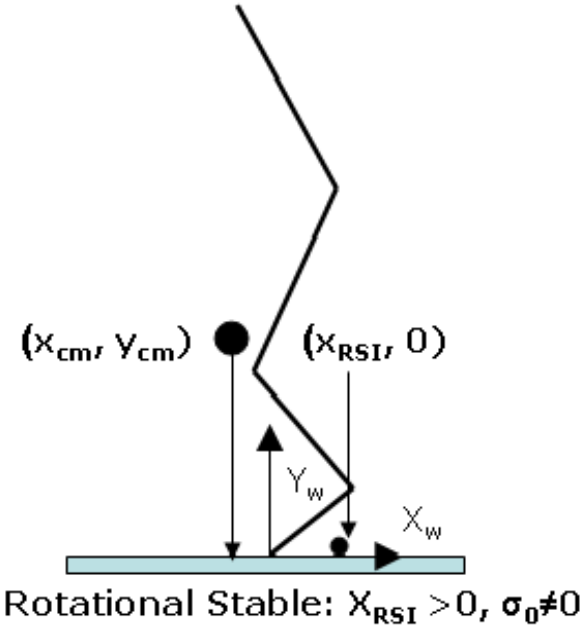

Figure 5.8: RSI point $x_{RSI} > 0$. Biped is *rotational stable* even if $x_{cm}(\theta) < 0$.

1. Consider the expression of x_{RSI} in (5.12). If $\sigma_0 = 0$, the stability condition in *Theorem* 5.2.2 effectively leads to $x_{cm}(\theta) > 0$ (Fig. 5.7). Basically, this is the GCM (Ground Projection of CM) which explains the *rotational stability* for stationary biped [10]. The location of RSI point addresses the effects of the non-zero angular momentum.

2. The magnitude of the positive x_{RSI} indicates the degree of *rotational stability*. When $\sigma > 0$, larger value of σ lessen the positive magnitude of x_{RSI} leading to lesser *rotational stability*. Actually, the positive value of σ tries to rotate the biped counterclockwise inducing tendency to topple forward. That is reflected in the value of x_{RSI}. Similar explanation is possible when $x_{cm}(\theta) < 0$ and the biped is *rotational stable* because the negative value of σ is such that $x_{RSI} > 0$ (Fig. 5.8). The biped becomes 'rotational unstable' when $x_{RSI} \not> 0$.

3. The concept of planar RSI point can be extended to three-dimensional representation when both frontal and sagittal planes are considered (Fig. 5.1 (a), (b)). The RSI point will have $(x_{RSI}, 0, z_{RSI})$ form in three-dimensional case. The x_{RSI} and z_{RSI} can be computed independently. The constants K_1, K_2 and K_3 would vary in different planes. x_{RSI} indicates degree of *rotational stability* in sagittal plane while z_{RSI} indicates that in frontal plane.

5.3 RSI Point Based Stability Criteria

The RSI-based criterion in *Theorem* 5.2.2 determines stability in postures with forward foot-rotation and $\dot{\theta}_2 = 0$. For utilizing RSI point as stability criterion during

biped locomotion, the RSI-based criterion in *Theorem* 5.2.2 is revisited in two perspectives: (1) *rotational stability* when $\dot{\theta}_2 \neq 0$ and (2) backward foot-rotation.

5.3.1 Gaits with $\dot{\theta}_2 \neq 0$

In the bipedal gaits with $\dot{\theta}_2 \neq 0$, the system internal dynamics becomes as (5.21) [7].

$$\begin{aligned} \dot{\theta}_1 &= \frac{\sigma}{M_{11}(\theta_2)} - \frac{M_{12}(\theta_2)}{M_{11}(\theta_2)}\dot{\theta}_2, \\ \dot{\sigma} &= -mgx_{cm}(\theta). \end{aligned} \tag{5.21}$$

For bipedal gaits with $\dot{\theta}_2 \neq 0$, (θ_1, σ) can be solved from (5.21) at any point of time. The *rotational stability* of the biped at the posture corresponding to such (θ_1, σ) solutions can be decided based on the RSI criterion mentioned in *Theorem* 5.2.2. If such (θ_1, σ) solutions satisfy the criterion mentioned in *Theorem* 5.2.2, the biped is rotationally stable at the posture at that particular time. For stability of a particular gait, every posture of the gait and corresponding solutions of (5.21) should be *rotational stable*. While utilizing the RSI criteria, the constants in (5.9) have to be computed for every posture associated with the gait.

5.3.2 Backward foot-rotation

Consider the foot link shown in Fig. 5.9. To decide on the forward toppling we can use the criterion mentioned in *Theorem* 5.2.2 with $l_1 = L_{ff}$ in (5.2) and (5.9). If positive value of x_{RSI} is sufficiently large, the ankle hits the ground and the impact might make the biped to topple backward. During backward toppling, the biped rotates about the end-point (other than toe) of the foot-link and can be considered

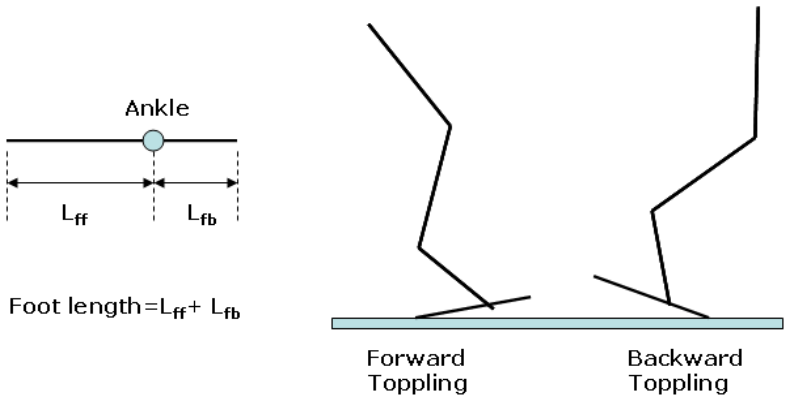

Figure 5.9: Forward and backward foot-rotation.

like tiptoed biped about the other end-point of the foot-link.

In case of backward foot-rotation, $\theta_1 < 0$ and the phase-portrait is the mirror image of Fig. 5.4. The expression for RSI with respect to the point of rotation during backward foot-rotation (x^b_{RSI}) is given by (5.22) where $\sigma_0^{'}$ is the angular momentum about the point of rotation in backward direction and $K_1^{'}$, $K_2^{'}$, $K_3^{'}$ are computed from (5.9) with $l_1 = L_{fb}$. $\sigma_0^{'}$ is dependent on the nature of impact and foot/ground compliance. Without impact $\sigma_0^{'} = \sigma_0 - m\dot{x}_{cm}(\theta)(L_{ff} + L_{fb})$ where σ_0 is the angular momentum about toe [3]. Impact can be taken into account by modifying $\sigma_0^{'}$ according to the impact model [91]. The equilibrium point during backward foot-rotation is $(K_3^{'}, 0)$. The condition for *rotational stability* is $x^b_{RSI} < 0$ (similar to the criterion in *Theorem* 5.2.2). The relative position between x^b_{RSI} and x_{RSI} with respect to (X, Y) is given by (5.22).

$$\begin{aligned} x^b_{RSI} &= x_{cm}(\theta_{10}, \theta_2^*) - (L_{ff} + L_{fb}) - \frac{\sigma_0^{'}}{mg}\sqrt{\frac{K_1^{'}K_2^{'}(1 + cos(K_3^{'} - \theta_{10}))}{2}}, \\ \implies x^b_{RSI} &= x_{RSI} - (L_{ff} + L_{fb}). \end{aligned} \tag{5.22}$$

Hence, the condition to avoid backward toppling is as per (5.23).

$$\begin{aligned} & x^b_{RSI} && < 0, \\ \implies & x_{RSI} && < (L_{ff} + L_{fb}), \\ \implies & x_{RSI} && < \textit{foot length}. \end{aligned} \tag{5.23}$$

5.3.3 Stability Criterion

Merging the conditions for both forward (*Theorem* 5.2.2) and backward foot-rotation in (5.23), the overall bipedal stability condition is rewritten as (5.24). It is notable for the computation of x_{RSI} that the constants in (5.9) is dependent on the point of foot-rotation during biped locomotion. Moreover, σ is the angular momentum about the point of foot-rotation during forward and backward rotation.

$$\textit{Biped Stability Criteria :} \quad 0 < x_{RSI} < \textit{foot length}. \tag{5.24}$$

5.3.4 Comparison with other Ground Reference Points

RSI-based stability criterion fundamentally differs from well known ground reference points in a number of ways. When ZMP is within the support polygon, it coincides with the center of pressure (CP) [10]. Such postures with ZMP/CP within the support polygon are statically stable and there is no foot-rotation. When ZMP is outside the support polygon, it is termed as Fictitious ZMP (FZMP) [9]. The location of ZMP/FZMP being outside the support polygon indicates that the foot is about to

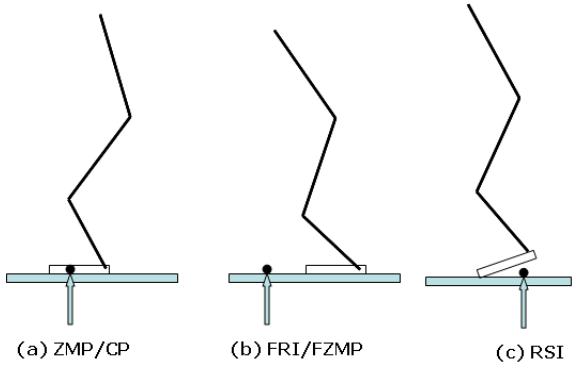

Figure 5.10: ZMP/FRI/CP/FZMP and RSI: (a) Foot is not going to rotate. (b) Foot is about to rotate. (c) Foot is rotated, and bipedal posture is *rotational stable*.

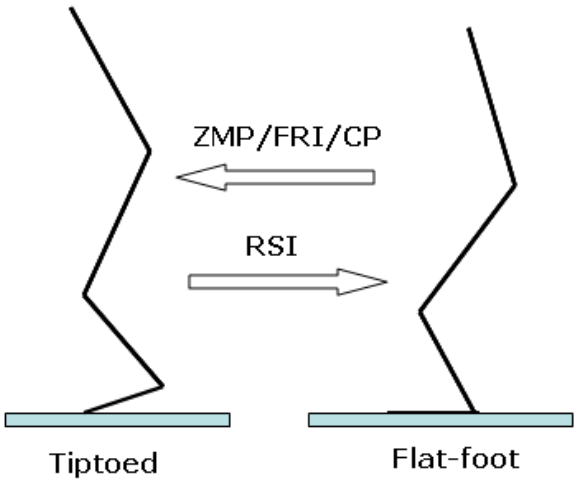

Figure 5.11: ZMP/FRI/CP and RSI: ZMP/CP/FRI indicate whether the foot is about to rotate or not, RSI point indicates whether the bipedal posture will lead to a flat-foot posture or not.

rotate. FZMP and FRI indicates similar stability aspects of biped locomotion (Fig. 5.10). The location of FRI point indicates whether the foot is going to rotate or not. When FRI is located within the support polygon it coincides with ZMP. All these ground reference points investigates certain stability aspects associated with the flat-foot bipedal posture. Location of such points indicates the possibility of foot-rotation during locomotion. On the contrary, RSI point deals with situations when foot is already rotated but the biped has not fallen down. The location of the RSI point indicates whether the biped is going back to flat-foot posture or topple over (Fig. 5.11).

In flat-foot postures, ZMP and FRI use the torque generated at the toe-ground contact point due to GRF. Such torques due to GRF becomes zero in tiptoed bipeds because GRF acts at the point of rotation. Therefore, ZMP and FRI are not suitable for postural stability analysis when the foot is already rotated. On the other hand, RSI point does not use GRF in its computation and is able to analyze stability in tiptoed bipedal postures. However, RSI is not relevant in ideal flat-foot postures. The torques due to GRF will appear in equations (5.5) and (5.6) in flat-foot biped. Therefore, the stability concepts associated with RSI and ZMP/FRI are complementary to each other.

5.4 Simulations and Experiments

The applicability of RSI point in various scenarios associated with the biped locomotion is illustrated through simulation studies and validated experimentally. We limit our study to forward toppling, as backward toppling can be performed in a similar way. Four cases are studied and analyzed through simulations and experimentations.

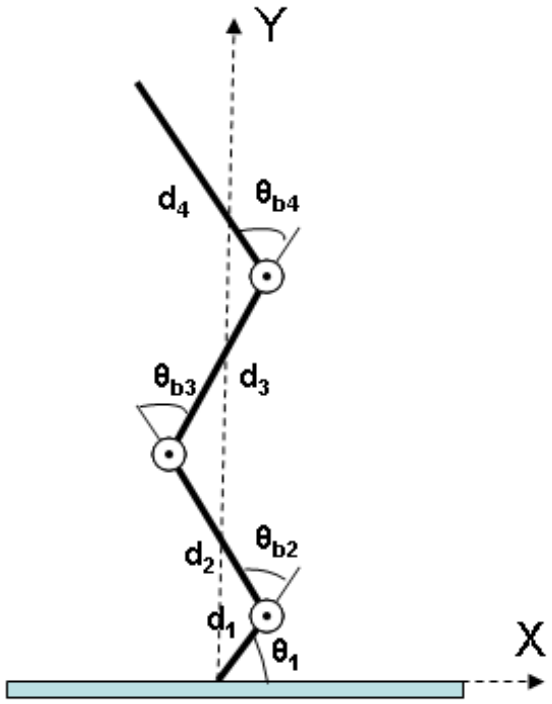

Figure 5.12: Parameters of BRAIL 2.0

In the first two cases, the biped's foot is already rotated with non-zero angular momentum. In the last two cases, the biped is stationary at the beginning and a force is applied from the backside. Stability of the biped in such scenario is analyzed using RSI point.

Simulation studies and experimental verifications are performed on the bipedal platform, BRAIL 2.0. The biped robot - BRAIL 2.0 - is described in Section 4.1.1. The parameters of the BRAIL 2.0 biped are shown in Table 4.1. The kinematic model of BRAIL 2.0 is shown in Fig. 5.12. The lengths and masses of the Foot, Shank, Thigh and Torso links are d_i and m_i (with $i = 1, 2, 3, 4$) respectively. Body angles i.e.,

ankle, knee and hip angles are $\theta_b = [\ \theta_{b1} \quad \theta_{b2} \quad \theta_{b2}\ ]^T$. Biped's absolute orientation is $\theta_a = [\ \theta_1 \quad \theta_b^T\ ]^T$.

5.4.1 Simulations

Simulations are done based on the parameters shown in Table 4.1. The dynamics of the biped is computed in the MATLAB/Simulink environment. The dynamic parameters are expressed in C language code by using 'ccode' command for faster computation and simulation. The control algorithms are simulated in Microsoft VC++ environment using the C code of the biped-dynamics generated by MATLAB/Simulink. Integration algorithm is based on fourth order Runge-Kutta method with a fixed step size of 0.0001s.

Four different examples are provided to illustrate the applicability of RSI point in stability analysis of biped locomotion. In the first example, the biped's foot is rotated such that $x_{cm}(\theta) < 0$. In this scenario, the location of GCM makes the biped to topple forward when it is stationary. However, with negative angular momentum, the location of the RSI point satisfies the stability criterion in *Theorem* 5.2.2. Therefore, the bipedal posture is *rotational stable*. In the second example, the biped's foot is rotated but $x_{cm}(\theta) > 0$. In this scenario, the location of GCM makes the biped *rotational stable* when it is stationary. However, with positive angular momentum, location of RSI point is negative i.e., the biped is 'rotational unstable'. The Biped starts from a stationary posture in third and fourth examples. A force is applied on the biped from the backside. Whether the biped is rotational stable (example 3) or unstable (example 4) is investigated using RSI point.

Let us consider a bipedal posture with the body joint angles given by $\theta_b =$

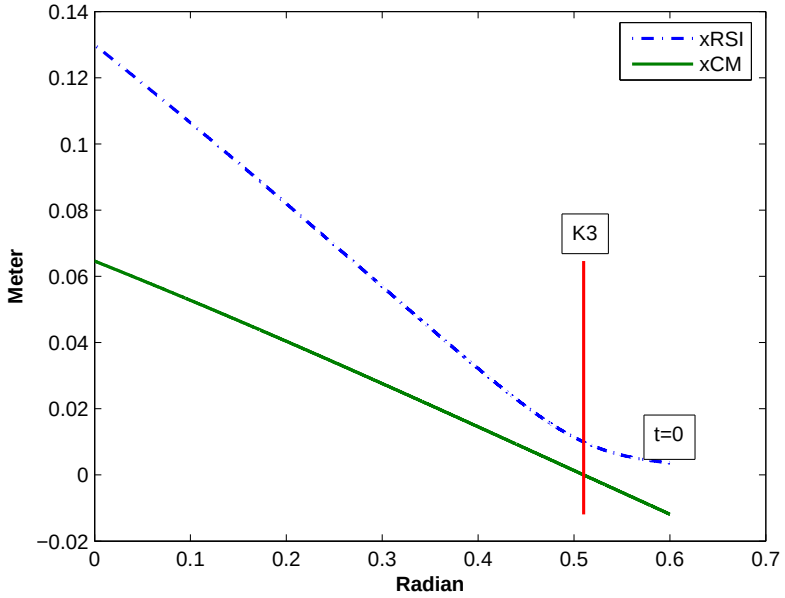

Figure 5.13: θ_1 Vs. x_{RSI} θ_1 Vs. x_{cm} and : $\theta_{10} = 0.6$ rad and $\sigma_0 = -0.0289\ kgm^2s^{-1}$.

$[\ 2.3638\quad -1.5217\quad 1.5286\ ]^T$ rad. With this body posture and $\theta_1 = 0$ i.e., $\theta_a = [\ 0\quad 2.3638\quad -1.5217\quad 1.5286\ ]^T$, the location of CM is $x_{cm}(\theta_a) = 0.0646$ m and $y_{cm}(\theta_a) = 0.1155$ m. It is noticeable that $0 < x_{cm}(\theta_a) < d_1$ which indicates that the biped is in a statically stable posture with $\theta_1 = 0$. The values of the three constants in (5.9) with $\theta_b = [\ 2.3638\quad -1.5217\quad 1.5286\ ]^T$ are $K_1 = 27.6501$, $K_2 = 1.6873$ and $K_3 = 0.5101$. Examples are shown to illustrate the effects of *rotational stability* on the bipedal systems.

Example 1 ($x_{cm}(\theta) < 0$, but *rotational stable*)

Consider the posture given by $\theta_a = [\ 0.6\quad 2.3638\quad -1.5217\quad 1.5286\ ]^T$. Let, the initial joint angular velocity is $\dot{\theta}_1 = -0.8\ rad/s$ and the rest of the angular velocities are zeroes. Therefore, $\theta_{10} = 0.6$ and $\theta_{10} > K_3$ indicate that $x_{cm}(\theta) < 0$ i.e., the biped

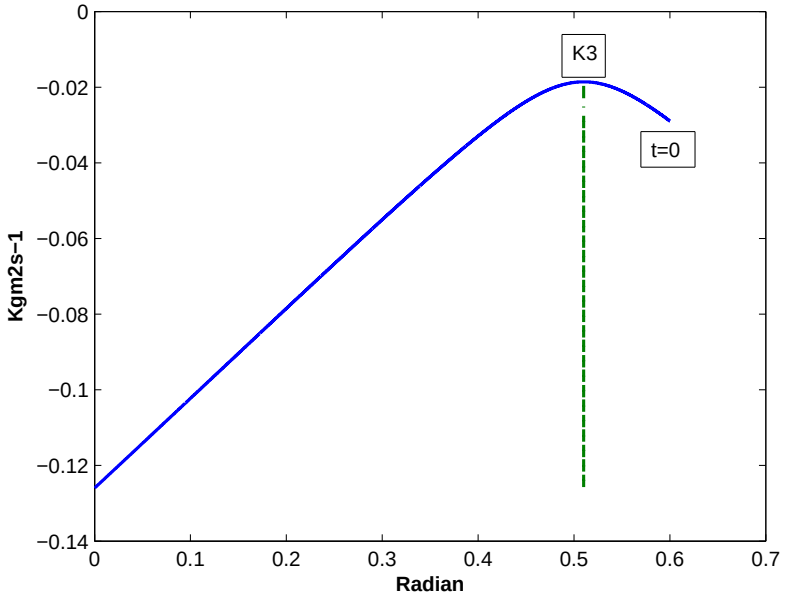

Figure 5.14: θ_1 Vs. σ: $\theta_{10} = 0.6$ rad and $\sigma_0 = -0.0289\ kgm^2s^{-1}$.

was statically unstable at the beginning. However, $\sigma_0 = \frac{\dot{\theta}_1}{K_1}$ is such that $x_{RSI} > 0$ which indicates *rotational stability* of the bipedal posture. Fig. 5.13 shows the plots for θ_1 vs x_{cm} and θ_1 vs x_{RSI}. It is seen that always $x_{RSI} > 0$ although $x_{cm}(\theta) < 0$. Fig. 5.13 shows the θ_1 vs σ plot. As $\theta_1 = 0$ plane is reached, the particular biped posture, θ_a, is *rotational stable*.

Example 2 ($x_{cm}(\theta) > 0$, but rotational unstable)

Consider the posture given by $\theta_a = [\ 0.3 \quad 2.3638 \quad -1.5217 \quad 1.5286\ ]^T$. The initial joint angular velocity $\dot{\theta}_1 = 1.5\ rad/s$ and the rest of the angular velocities are zeroes. Therefore, $\theta_{10} = 0.3$ and $\theta_{10} < K_3$ indicate that $x_{cm}(\theta) > 0$ i.e., the biped was statically stable at the beginning. However, $x_{RSI} < 0$, which indicates rotational instability (Figs. 5.15 and 5.16). The particular biped posture topples forward with

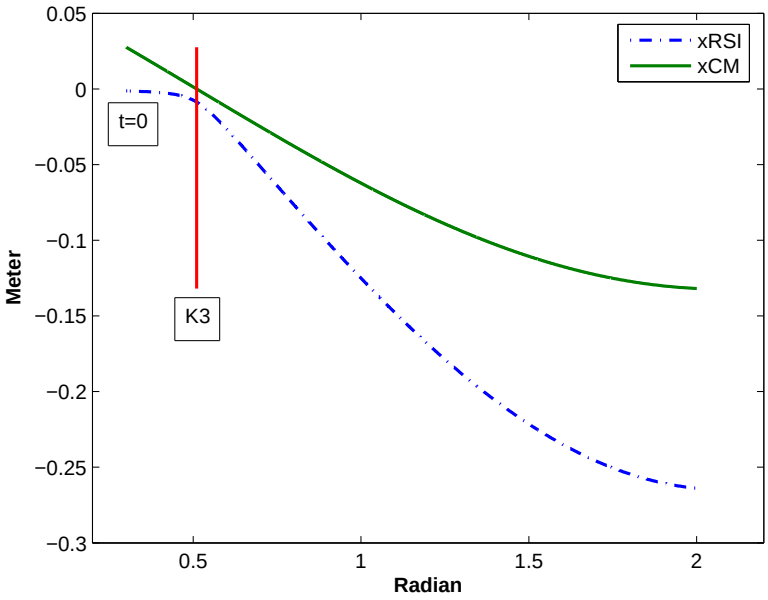

Figure 5.15: θ_1 Vs. x_{RSI} and θ_1 Vs. x_{cm}: $\theta_{10} = 0.3$ rad and $\sigma_0 = 0.0542\ kgm^2s^{-1}$.

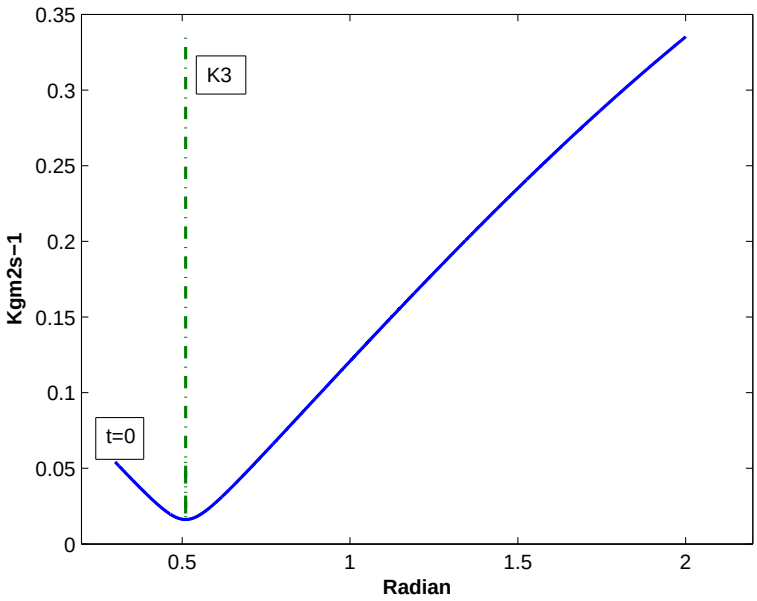

Figure 5.16: θ_1 Vs. σ: $\theta_{10} = 0.3$ rad and $\sigma_0 = 0.0542\ kgm^2s^{-1}$.

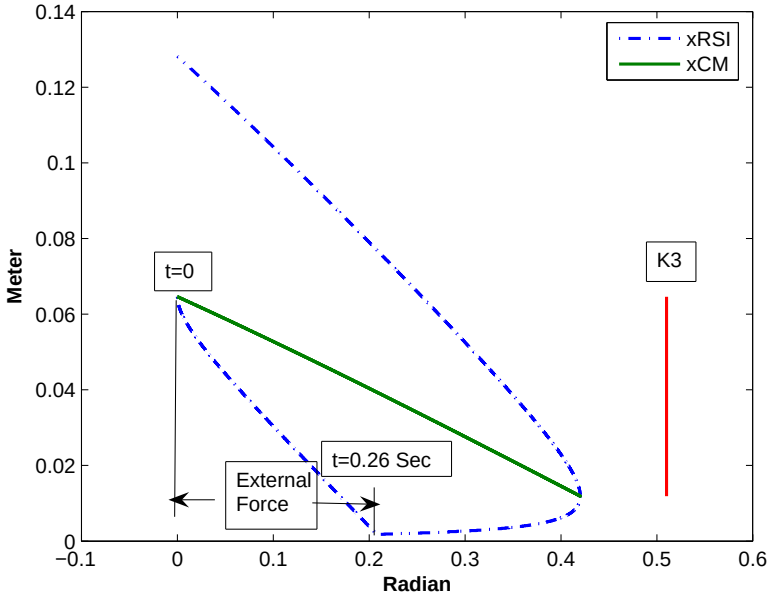

Figure 5.17: θ_1 Vs. x_{RSI} and θ_1 Vs. x_{cm}: Pushed from the backside and *rotational stable*.

time and is 'rotational unstable'.

Example 3 (push from back and *rotational stable*)

The initial posture of the biped is considered as $\theta_a = [\ 0 \quad 2.3638 \quad -1.5217 \quad 1.5286\ ]^T$ and all the angular velocities are zero. The biped is pushed from the backside by a force of 2.6 N at a height of 40 cm for 0.26 sec (based on the experiment discussed in section 5.4.2). It is equivalent to a torque of $2.6 \times 0.4 = 1.04$ Nm for 0.26 sec at the joint between toe and ground. Hence, (5.10) is modified as (5.25). Due to the application of the external push from the backside, the biped moves forward which leads to $\theta_{10} = 0.2078$ rad and $\sigma_0 = 0.0710\ kgm^2s^{-1}$.

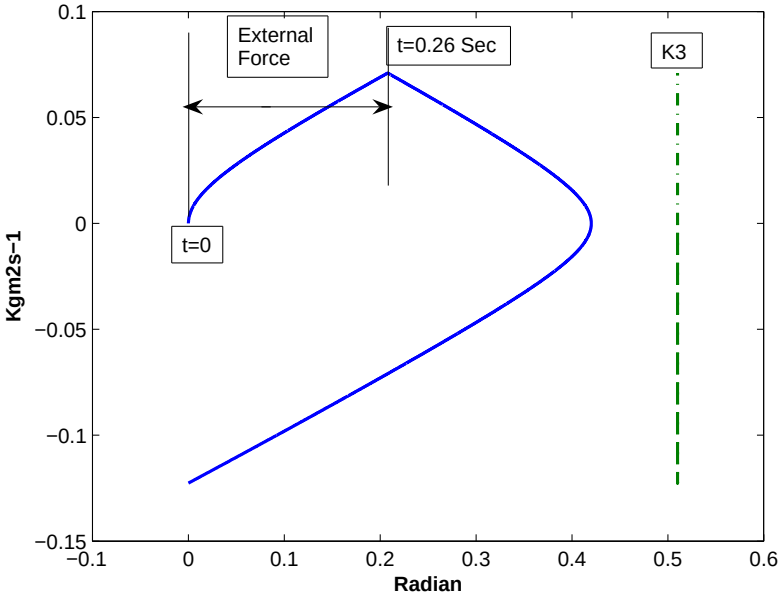

Figure 5.18: θ_1 Vs. σ: Pushed from the backside and *rotational stable*.

$$\begin{aligned} \dot{\theta}_1 &= K_1\sigma, \\ \dot{\sigma} &= K_2 sin(\theta_1 - K_3) + 1.04. \end{aligned} \tag{5.25}$$

Now, consider the posture given by $\theta_a = [\ 0.2078 \quad 2.3638 \quad -1.5217 \quad 1.5286\ ]^T$ with $\sigma_0 = 0.0710\ kgm^2s^{-1}$. As $x_{RSI} > 0$, the posture is *rotational stable*. Therefore, the biped was able to absorb the push (Figs. 5.17 and 5.18).

Example 4 (push from back and rotational unstable)

The initial posture of the biped is considered as $\theta_a = [\ 0 \quad 2.3638 \quad -1.5217 \quad 1.5286\ ]^T$ and all the angular velocities are zeroes. A force of 2.6 N is applied at a height of 40 cm for 0.265 sec from the backside of the biped. It is equivalent a torque of around $2.6 \times 0.4 = 1.04$ Nm for 0.265 sec at the joint between the toe and ground. Due to

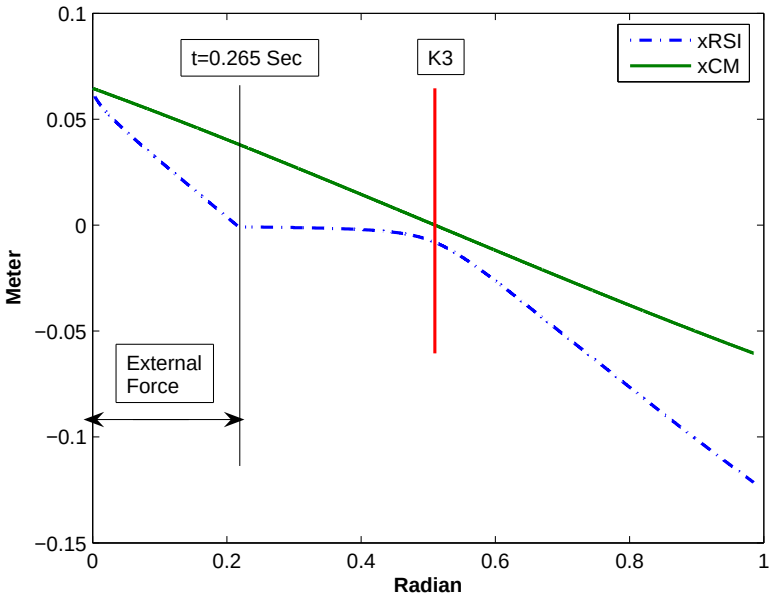

Figure 5.19: θ_1 Vs. σ: Pushed from the backside and 'rotational unstable'.

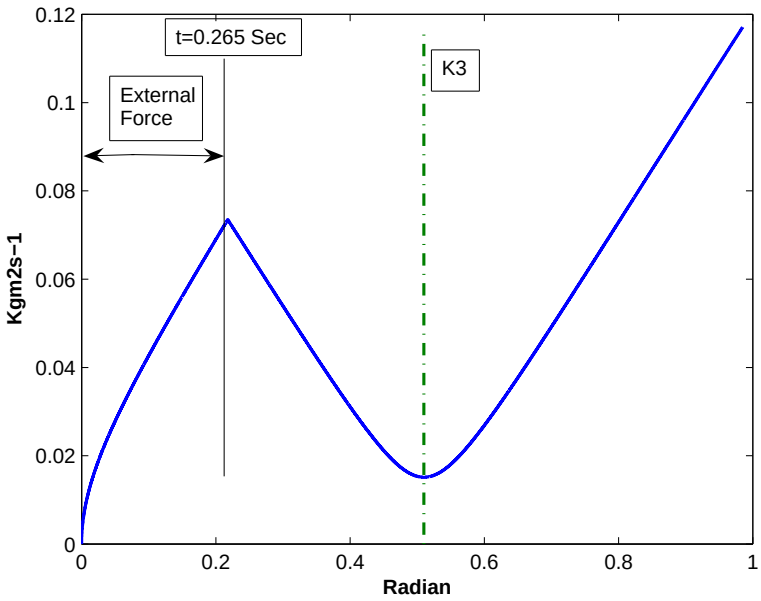

Figure 5.20: θ_1 Vs. σ: Pushed from the backside and 'rotational unstable'.

the application of the external force from backside the biped moves forward leading $\theta_{10} = 0.2178$ rad and $\sigma_0 = 0.0735\ kgm^2s^{-1}$ (from (5.25)). Now, consider the posture given by $\theta_a = [\ 0.2178 \quad 2.3638 \quad -1.5217 \quad 1.5286\ ]^T$ with $\sigma_0 = 0.0735\ kgm^2s^{-1}$. As $x_{RSI} < 0$, the biped topples forward due to the push (Figs. 5.19 and 5.20).

5.4.2 Experiments

The experiments were performed on the biped BRAIL 2.0 based on the examples 3 and 4. The biped's initial posture is $\theta_a = [\ 0 \quad 2.3638 \quad -1.5217 \quad 1.5286\ ]^T$ (Fig. 5.21). All the six motors at the three joints of the both legs are rotated to the angular positions corresponding to $\theta_b = [\ 2.3638 \quad -1.5217 \quad 1.5286\ ]^T$ and are hold at those positions. A force is applied on it from backside and intensity of the push is measured using force sensors. The force measurement system uses Tekscan FlexiForce force sensors and certain linearization circuitry (details available in [99]).

The height of the point of application of the force is 40 cm above the ground. The sensing portion of the FlexiForce sensor is placed at the point of application of force. Force is applied with different amplitude and time duration. It is found that when a force of 2.6 N is applied for 0.26 sec the biped can maintain *rotational stability*. This validates the *example 3* in simulation. When similar amount of force is applied for $0.26 - 0.30$ sec the biped becomes 'rotation unstable'. This validates the *example 4* in simulation.

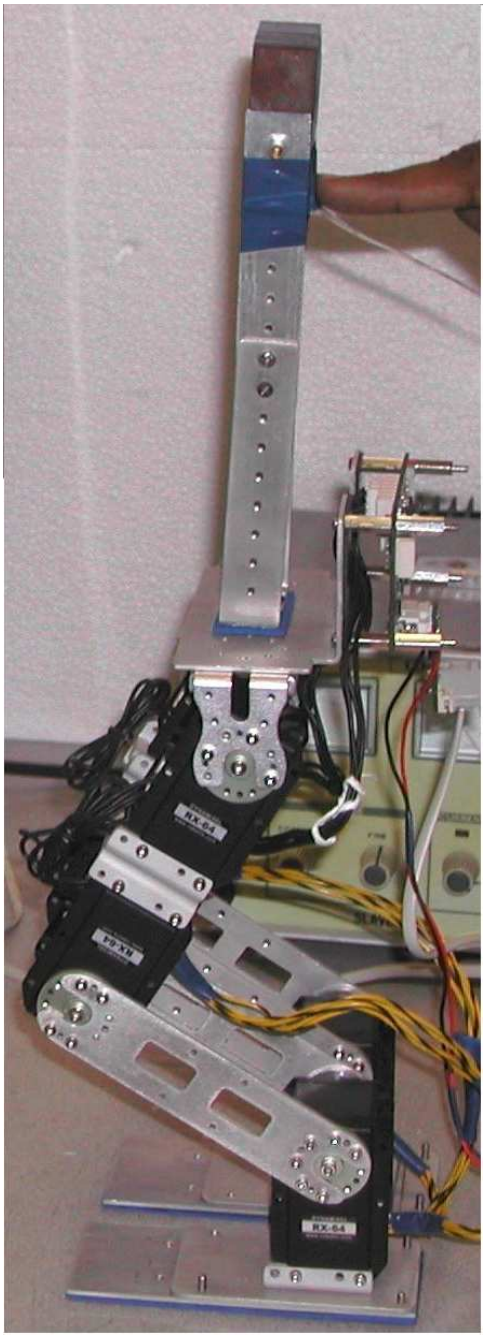

Figure 5.21: BRAIL 2.0: Push from back.

5.5 Conclusions

The stability aspects of biped locomotion with foot-rotation is investigated in the article. The planar bipeds are modeled as a two-link kinematic structure with the rotating foot being the first link and rest of the biped being modeled as an inverted pendulum (and second link). The model is *underactuated* due to the absence of actuation at the joint between the rotating foot and ground. Presence of underactuation in the model leads to non-trial internal dynamics. A stability concept named *rotational stability* is introduced to indicate the stability of the internal dynamics (5.10) corresponding to a bipedal posture with foot-rotation. It is established that the *rotational stability* of the bipeds is quantified by the location of the ground reference point called 'rotational stability index (RSI)' point. Examples of 'rotational stable/unstable' bipedal configurations in different postures are illustrated in simulation and are validated experimentally on a biped robot.

Chapter 6

Conclusions and Future Directions

6.1 Conclusions

Biped locomotion can be either flat-foot (foot-link does not loose contact with ground surface) or with foot-rotation (foot-link rotates about toe). Presence of foot-rotation, during biped locomotion, brings in various stability issues associated with the additional passive DOF at the joint between toe and ground. Based on the presence of foot-rotation during locomotion, the research contributions reported in this dissertation can be divided into two parts. First part of the dissertation deals with stability, optimization and robustness of flat-foot walking gaits while the second part deals with stability issues associated with the foot-rotation during biped locomotion.

The inverse-kinematics based walking gait is generated for a twelve DOF biped robot. The walking gait is parameterized in terms of certain parameters i.e., Step length, Bending-height, Maximum Lifting-height and Maximum Frontal-shifting. The gait is optimized by finding the optimum values of the parameters considering a tradeoff between postural stability and walking speed. ZMP is utilized as a stability criterion and it is assumed that foot is flat during locomotion. Inverse kinematic

based gait is computed off-line and implemented on a biped robot - BRAIL 1.0. Due to off-line computation of the inverse kinematic based gait, such gaits need further enhancement for robustness. Stability of such gaits is further addressed when the biped is subjected to disturbances.

An online ZMP compensation technique for disturbance rejection is proposed to improve the biped locomotion gait. In this method, the ZMP is kept within a closer range of the the ankle joint ('safety zone'). Whenever the ZMP falls outside the 'safety zone', due to disturbances, the online compensation is activated to bring back the ZMP location within the 'safety zone'. The ZMP compensation method is utilized in various applications to show its suitability to improve biped-locomotion-stability and reject disturbances. Utilizing the compensation technique, a humanoid robot was able to carry additional weight placed at the backside of robot, climb up or down slopes and absorb pushes from back or front. In the compensation technique, ZMP is utilized as stability criterion considering a flat-foot locomotion.

The later part of the dissertation deals with biped locomotion in presence of foot-rotation. The foot being already rotated, the bipedal systems becomes *underactuated* due to the additional passive DOF at the joint between toe and ground. The underactuated bipedal system has two dimensional zero-dynamics submanifold of the full order biped dynamics. For the postural stability in such scenarios where the foot is rotated, the stability of the associated zero-dynamics plays a key role. The stability analysis in the dissertation is mainly focused on the stability of such zero-dynamics. Conditions are established for the stability of the zero-dynamics as well as the underactuated bipedal dynamics (with foot-rotation).

Landing stability analysis is performed while considering jumping gait of planar

biped robot. Landing is considered in presence of foot rotation and is modeled as underactuated two-link inverted pendulum. While considering the asymptotic stability of the biped's ZD for stable landing, the foot compliance model with ground is modeled as spring-damper. Stability conditions are established for stable landing and, *critical potential index* and *critical kinetic index* are introduced to measure the landing stability margin. The stability margin depends on certain properties of the bipedal structure, foot-ground contact surface and the control parameters.

The stability conditions of biped locomotion with foot-rotation is established. The biped with foot rotation is underactuated by one DOF due to the passive DOF at the joint between the toe and ground, and such bipeds are modeled as underactuated two-link inverted pendulum. The stability aspects of such configurations are indicated by "*rotational stability*". A ground reference point named "*rotational stability index (RSI)*" point is introduced to quantify *rotational stability* of a biped with foot rotation.

6.2 Future Directions

The concept of RSI point is useful to analyze stability of biped locomotion with foot rotation. Biped (with foot) locomotion is stable irrespective of occurrence of foot rotation if the location of RSI point satisfies the stability criterion mentioned in *Theorem* 5.2.2 and section 5.3.3.

Some possible applications of RSI point might be:

- Landing stability of jumping and hopping gaits: In the landing stability analysis in Chapter 4, the stability conditions are based on foot-ground compliance

model and certain control parameters.

When the foot is rotated, RSI point can analyze whether the biped is about to attain a flat-foot posture (stability in Subsystem A, Fig. 4.9). However, the concept of RSI point is not relevant in flat-foot postures. Hence, RSI point can not explain stability in Subsystem B (Fig. 4.9). The stability of flat-foot bipeds is analyzed by ZMP or FRI. The unification of the concepts of RSI and ZMP/FRI is an interesting area to work on.

- Stability of walking gaits: The concept of RSI point can be applied to find out stable walking gait with foot rotation for biped robots.

  Advantage of using RSI-based stability criterion is that it takes into account the foot-rotation during locomotion. Therefore, RSI-based criteria provides greater stability margin than ZMP-based criteria. For example, ZMP criteria says biped is statically unstable when ZMP is outside the foot support area because such ZMP locations cause foot-rotation. However, the RSI-based criteria suggests that the biped is *rotational stable* as long as $0 < x_{RSI} <$ *foot length*, irrespective of foot-rotation. Similar argument is true for FRI point as well.

- Periodicity aspects of walking, hopping and running gaits: RSI point approach can be useful in establishing periodicity of various periodic gaits.

  The existence of periodic orbits in biped locomotion can be investigated with periodic occurrence of forward and backward foot-rotation.

Chapter 7

Author's Publications

7.1 International Journal

1. P. Vadakkepat, Dip Goswami and Chia Meng Hwee. "Disturbance Rejection by Online ZMP Compensation," Robotica, Cambridge Press, vol. 26, pp. 9-17, 2007.

2. P. Vadakkepat and Dip Goswami. "Biped Locomotion: Stability, Analysis and Control," Int. Journal of Smart Sensing and Intelligent Systems, vol. 1, no 1, pp 187-207, March 2008.

3. Dip Goswami, Prahlad Vadakkepat and Phung Duc Kien, "Genetic Algorithm-based Optimal Bipedal Walking Gait Synthesis considering Tradeoff between stability margin and Speed," Robotica (2008).

4. Prahlad Vadakkepat, Ng Buch Sin, Dip Goswami, Zhang Rui Xiang, Tan Li Yu, "Soccer Playing Humanoid Robots: Processing Architecture, Gait Generation and Vision System," Robotics and Autonomous Systems (Accepted for publication).

5. Dip Goswami, Prahlad Vadakkepat, "Jumping Gaits for Planer Biped Robots with Stable Landing," IEEE Transaction on Robotics (Under 2nd Review).

6. Dip Goswami, Prahlad Vadakkepat, "RSI Point: Postural Stability in Bipeds," IEEE Transaction on Robotics (Under Review).

7.2 International Conference

1. Vadakkepat, P and Dip Goswami, "MANUS Humanoid: A Test bed for Advanced Robotics Research," International Conference on Emerging Mechanical Technology Macro to Nano, ed. R. K. Mittal and N. N. Sharma (2007): 195 203 (Emerging Mechanical Technology Macro to Nano, 16 18 Feb 2007, Birla Institute of Technology and Science, Pilani, India).

2. P. Vadakkepat and Dip Goswami, "Biped Locomotion: Stability, Analysis and Control," CIRAS, Palmerston North, New Zealand, 28-30 November 2007.

3. Jin Yongying, Dip Goswami, and Prahlad Vadakepat, "Walking Gait Generation for Humanoid Robot BRAIL 1.0," CIRAS, 19-21 June 2008, Linz, Austria.

4. Burra Pavan Kumar, Dip Goswami, and Prahlad Vadakepat, "Jumping and Hopping Robot: Development and Experimentation," CIRAS, 19-21 June 2008, Linz, Austria.

Bibliography

[1] J. Yamaguchi, D. Nishino, A. Takanishi, "Realization of dynamic biped walking varying joint stiffness using antagonistic driven joints," Proceedings of International Conference of Robotics and Automation, Vol. 3, pp 2022-2029 (1998).

[2] M. Ogino, Y. Katoh, M. Aono, M. Asada, K. Hosoda, "Vision-based reinforcement learning for humanoid behaviour generation with rhythmic walking parameters," Proceedings of IROS, Vol. 2, pp 1665-1671 (2003).

[3] ER Westervelt, JW Grizzle, C. Chevallerau, JH Choi, B. Morris "Feedback control of dynamic bipedal robot locomotion," Boca Raton : CRC Press (2007).

[4] John J. Craig, "Introduction to Robotics: Mechanics and Control," Second Edition, Addison-Wesley Longman Publishing Co., Inc. Boston, MA, USA. 1989.

[5] K.S. Fu, R.C. Gonzalez and C.S.G. Li, "Robotics: control, sensing, vision, and intelligence," McGraw-Hill, New York, USA, 1987.

[6] M. Vukobratović, B. Borovac, D. Surla and D. Stokić, "Biped Locomotion: Dynamics, Stability, Control and Application," Springer, 1990.

[7] C. Chevallereau, E.R. Westervelt and J. W. Grizzle, "Asymptotically Stable Running for a Five-Link, Four-Actuator, Planar Bipedal Robot," The International Journal of Robotics Research, vol. 24, no. 6, pp. 431-464, 2005.

[8] Jean-Jacques E. Slotine, Weiping Li, "Applied Nonlinear Control," New Jersey, 1991.

[9] M. Vukobratovic and B. Borovac, "Zero Moment Point - Thirty Five Years of its Life," International Journal of Humanoid Robotics Vol. 1, No.1 157-173, 2004 .

[10] Ambarish Goswami, "Postural Stability of Biped Robots and the Foot-Rotation Indicator (FRI) Point," The International Journal of Robotics Research, vol. 18, no. 6,pp. 523-533, 1999.

[11] M.H. Raibert, Jr H.B. Brown and M. Chepponios, "Experiments in Balance with a 3D One-legged Hopping-Machine," International Journal of Robotic Research, vol. 3, no. 2, pp 75-92, 1984.

[12] E. Koditschek and Martin Bhler, "Analysis of a Simplified Hopping Robot," The International Journal of Robotics Research, vol. 10, no. 6, pp. 587-605, 1991.

[13] T. Sugihara, Y. Nakamura and H. Inoue, "Real-time humanoid motion generation through ZMP manipulation based on inverted pendulum control," ICRA, pp. 1404 - 1409 vol.2, 11-15 May 2002.

[14] S. Kajita, F. Kanehiro, K. Kaneko, K. Fujiwara, K. Harada, K. Yokoi and H. Hirukawa, "Biped walking pattern generation by using preview control of zero-moment point," IEEE International Conference on Robotics and Automation (ICRA), pp. 1620 - 1626, vol.2, 14-19 Sept. 2003.

[15] S. Kitamura, Y. Kurematsu and M. Iwata, "Motion generation of a biped locomotive robot using an inverted pendulum model and neural networks," IEEE Conference on Decision and Control, pp. 3308 - 3312, vol.6, 5-7 Dec. 1990.

[16] Napoleon, S.Nakaura, M. Sampei, "Balance control analysis of humanoid robot based on ZMP feedback control," IEEE International Conference on Intelligent Robots and System, Vol. 3, pp. 2437-2442 (2002).

[17] Hun-ok Lim, Y. Yamamoto and A. Takanishi, "Control to realize human-like walking of a biped humanoid robot," IEEE International Conference on Systems, Man, and Cybernetics, pp. 3271 - 3276, vol.5, 8-11 Oct. 2000.

[18] JH Choi, JW Grizzle, "Planar bipedal walking with foot rotation," American Control Conference, Vol. 7, pp. 4909- 4916 (2005).

[19] A.Goswami, "Foot rotation indicator (FRI) point: a new gait planning tool toevaluate postural stability of biped robots," IEEE International Conference on Robotics and Automation, Vol. 1, pp. 47-52 (1999).

[20] Yamaguchi, J., Soga, E., Inoue, S., Takanishi, A., "Development of a bipedal humanoid robot-control method of whole body cooperative dynamic biped walking," Proceedings of 1999 IEEE International Conference on Robotics and Automation, Vol. 1, 10-15, 368 - 374, 1999.

[21] J. Vermeulen, B. Verrelst, D. Lefeber, P. Kool B. Vanderborght, "A real-time joint trajectory planner for dynamic walking bipeds in the sagittal plane," Robotica, Volume 23, Issue 06, Nov 2005, pp 669-680.

[22] K. Hirai, M. Hirose, Y. Haikawa and T. Takenaka, "The Development of Honda Humanoid Robot," Proceedings of the 1998 IEEE International Conference on Robotics and Automation, 1321-1326, 1998.

[23] N. Shiraishi, Y. Kawaida, Y. Kitamura, S. Nakaura and M. Sampei, "Vertical jumping control of an Acrobat Robot with consideration of input timing," Proceedings of the 41st SICE Annual Conference, vol. 4, pp. 2531 - 2536, 5-7 Aug. 2002.

[24] K. Mitobe, N. Mori N, K. Aida, Y. Nasu, "Nonlinear feedback control of a biped walking robot," Proceedings of 1995 IEEE International Conference on Robotics and Automation, Vol. 3, pp 2865 - 2870 (1995).

[25] Garcia M., Chatterjee A., Ruina A., "Efficiency, speed, and scaling of two-dimensional passive-dynamic walking," Dynamics and Stability of Systems, Vol. 15, No. 2, 75-99, 2000.

[26] Steve Collins, Andy Ruina, Russ Tedrake, Martijn Wisse, "Efficient Bipedal Robots Based on Passive Dynamic Walkers," Science Magazine, Vol. 307, 1082-1085, 2005.

[27] F. Yamasaki, K. Hosoda and M. Asada, "An Energy consumption based control for humanoid walking," IEEE/RSJ International Conference on Intelligent Robots and System (IROS), pp. 2473 - 2477, vol. 3, 30 Sept.-5 Oct. 2002.

[28] K. Ono, R. Takahashi,A. Imadu and T. Shimada, "Self-excitation control for biped walking mechanism," IROS, pp. 1143 - 1148, vol.2, 31 Oct.-5 Nov. 2000.

[29] Kyung-Kon Noh, Jin-Geol Kim and Uk-Youl Huh, "Stability experiment of a biped walking robot with inverted pendulum," 30th IEEE Annual Conference of Industrial Electronics Society, pp. 2475 - 2479, vol. 3, 2-6 Nov. 2004.

[30] Xiuping Mu and Qiong Wu, "Synthesis of a complete sagittal gait cycle for a five-link biped robot," Robotica, pp 581-587, vol. 21, Issue 05, Oct 2003.

[31] A.W. Salatian and Y.F. Zheng, "Gait synthesis for a biped robot climbing sloping surfaces using neural networks. II. Dynamic learning," ICRA, pp. 2607 - 2611 vol.3, 12-14 May 1992.

[32] M. Cao and A. Kawamura, "A design method of neural oscillatory networks for generation of humanoid biped walking patterns," ICRA, pp. 2357 - 2362 vol.3, 16-20 May 1998.

[33] A. Dasgupta and Y. Nakamura,"Making feasible walking motion of humanoid robots from human motion capture data," ICRA, pp. 1044 - 1049 vol.2, 10-15 May 1999.

[34] Sang-Ho Choi, Young-Ha Choi and Jin-Geol Kim, "Optimal walking trajectory generation for a biped robot using genetic algorithm," IROS, pp. 1456 - 1461, vol.3, 17-21 Oct. 1999.

[35] M.Y. Cheng and C.S. Lin, "Genetic algorithm for control design of biped locomotion Systems," IEEE International Conference on Man and Cybernetics, pp. 1315 - 1320 vol.2, 22-25 Oct. 1995.

[36] Jung-Shik Kong, Bo-Hee Lee and Jin-Geol Kim, "A study on the gait generation of a humanoid robot using genetic algorithm," SICE 2004 Annual Conference, pp. 187 - 191 vol.1, 4-6 Aug. 2004.

[37] F. Arakawa and T. Fukuda, "Natural motion trajectory generation of biped locomotion robot using genetic algorithm through energy optimization," IEEE International Conference on Systems, Man, and Cybernetics, pp. 1495 - 1500, vol.2, 14-17 Oct. 1996.

[38] Z. Tang, C. Zhou, Z. Sun, "Humanoid Walking Gait Optimization Using GA-Based Neural Network," pp. 252-261, ICNC(2) 2005.

[39] Y. Sakagami, R. Watanabec, C. Aoyama, S. Matsunaga, N. Higaki, "The intelligent ASIMO: System overview and integration" Proceedings of the IEEE/RSJ International Conference on Intelligent Robots and Systems, Switzerland. pp. 24782483, 2002.

[40] L. Righetti, A.J. Ijspeert, "Programmable Central Pattern Generators: an application to biped locomotion control," IEEE International Conference on Robotics and Automation (ICRA06). Orlando, pp. 1585-1590, 2006.

[41] P. Manoonpong, T. Geng, T. Kulvicius, B. Porr, F. Wrgtter, "Adaptive, Fast Walking in a Biped Robot under Neuronal Control and Learning," PLoS Comput Biol, 3(7), e134, 2007.

[42] C. Capaday, "The special nature of human walking and its neural control," Trends Neurosci 25: 370376, 2002.

[43] J. Duysens, V. de Crommert, "Neural control of locomotion. Part 1: The central pattern generator from cats to humans," Gait and Posture 7: 131141, 1998.

[44] T. McGeer, "Passive dynamic walking," International Journal of Robotics Research, vol. 9, no., 2, pp. 62-82, 1990.

[45] A. J. Ijspeert, A. Crespi, D. Ryczko, J. M. Cabelguen, "From swimming to walking with a salamander robot driven by a spinal cord model," Science 315 (5817) 14161420, 2007.

[46] H. Kimura, Y. Fukuoka, A. H. Cohen, "Adaptive dynamic walking of a quadruped robot on natural ground based on biological concepts," International Journal of Robotics Research 26 (5) 475490, 2007.

[47] P. Manoonpong, F. Pasemann, H. Roth, "Modular reactive neurocontrol for biologically-inspired walking machines," The International Journal of Robotics Research, vol. 26, no. 3, pp. 301-331, 2007.

[48] R.D. Beer, R.D.Quinn, H.J. Chiel, R.E. Ritzmann, "Biologically inspired approaches to robotics: what can we learn from insects?," Communications of the ACM, Vol. 40, No. 3, pp. 3038, 1997.

[49] T. Geng, B. Porr, F. Wrgtter, "Fast Biped Walking with A Sensor-driven Neuronal Controller and Real-time Online Learning," The International Journal of Robotics Research, vol. 25, no.3, pp. 243-259, 2006.

[50] WA Gruver, TT Lee, PL Jeng, "Control of a 5-link biped robot for steady walking," IEEE International Symposium on Intelligent Control, pp 484-489 (1998).

[51] L. Roussel, C.-De-Wit, A. Goswami, "Generation of energy optimal complete gait cycles for biped robots," IEEE International Conference on Robotics and Automation, Vol. 3, Page(s): 2036-2041 (1998).

[52] Vibet M, "Control law decoupling for 2-D biped walking system Cotsaftis," IEEE Engineering in Medicine and Biology Magazine, Volume 7, Issue: 3, pp 41-45 (1988).

[53] S. Kajita, O. Matsumoto, M. Saigo, "Real-time 3D walking pattern generation for a biped robot with telescopic legs," IEEE International Conference on Robotics and Automation, Vol. 2, pp. 2299-2306 (2001).

[54] JS Albus, "A new approach to manipulator control: the cerebellar model articulation controller (CMAC)," ASME Journal of Dynamic systems, Measurements and Control, pp 220-227, (1975).

[55] YH Kim, FL Lewis, "Optimal design of CMAC neural-network controller for robot manipulators," IEEE Transactions on Systems, Man and Cybernetics: Part C, Vol. 30, Issue 1, pp 22-31 (2000).

[56] DM Katic, MK Vukobratovic, "Highly efficient robot dynamics learning by decomposed connectionist feedforward control structure," IEEE Transactions on Systems, Man and Cybernetics, Vol. 25, Issue 1, pp 145 - 158 (1995).

[57] M. Yamakita, M. Kishikawa and T. Sadahiro, "Motion control for robust landing of acrobat robot," Proc. IEEE/RSJ Int. Conf. on Intelligent Robots and Systems, pp. 1141-1146, 2003.

[58] S. Hyon, N. Yokoyama and T. Emura, "Back handspring of a multi-link gymnastic robot - reference model approach," Advanced Robotics, vol.20, no.1, pp. 93-113, 2006.

[59] Hun-ok Lim, Kaneshima, Y., Takanishi, A., "Online walking pattern generation for biped humanoid robot with trunk," Proceedings of IEEE International Conference on Robotics and Automation, Vol. 3, 11-15, 3111 - 3116, 2002 .

[60] McGeer T., "Passive walking with knees," Proc. IEEE Int. Conf. Robotics and Automation, Cincinnati, OH, 1640-1645, 1990.

[61] Russ Tedrake, Teresa Weirui Zhang, Ming-fai Fong, and H. Sebastian Seung, "Actuating a Simple 3D Passive Dynamic Walker," Proceedings of the IEEE International Conference on Robotics and Automation (ICRA), Vol. 5, 4656-4661, 2004.

[62] Collins, S. H., Wisse, M., Ruina, A. "A Three-Dimensional Passive-Dynamic Walking Robot with Two Legs and Knees," International Journal of Robotics Research, Vol. 20, No. 2, 607-615, 2001.

[63] M.D. Mann, "The Nervous System and Behavior," Harper and Row, Philadelphia, 1981.

[64] Y. Fukuoka, H. Kimura and A. H. Cohen, "Adaptive dynamic walking of a quadruped robot on irregular terrain based on biological concepts," International Journal of Robotics Research, Vol. 22, No. 3-4, 187-202 2003.

[65] Jun Nakanishi, Jun Morimoto, Gen Endo, Gordon Cheng, Stefan Schaal, Mitsuo Kawato, "Learning from demonstration and adaptation of biped locomotion," Robotics and Autonomous Systems, 47, 79-91 2004.

[66] Jun Morimoto, Gordon Cheng, C. G. Atkeson, G. Zeglin, "A Simple Reinforcement Learning for Biped Walking," Proc. IEEE International Conference on Robotics and Automation, April 2004.

[67] Jong-Hwan Kim, Dong-Han Kim Yong-Jae Kim, Kui-Hong Park, Jae-Ho Park, Choon-Kyoung Moon, and Kiam Tian Seow, "Humanoid Robot HanSaRam:

Recent Progress and Developments," Proc. International Conference on Computational Intelligence, Robotics and Autonomous Systems, 2002 .

[68] R. Zhang, P. Vadakkepat and C.M. Chew, "Motion Planning for Biped Robot Climbing Stairs," Proceeding of FIRA Robot World Congress, Vienna, Austria Oct 1-3, 2003 .

[69] K. Mitobe, G. Capi, Y. Nasu, "Control of walking robots based on manipulation of the zero moment point," Robotica Volume 18, Issue 06, Nov 2000, pp 651-657.

[70] Jong Hyeon Park, Hoam Chung, "ZMP compensation by online trajectory generation for biped robots," ICRA 1999 10-15 Oct Volume: 4, page(s): 960-965.

[71] Shimojo, M., Araki, T., Ming, A., and Ishikawa M., "A ZMP sensor for a biped robot," Proceedings. 2006 Conference on International Robotics and Automation (IEEE Cat. No. 06CH37729D), 2006, pages 1200-1205.

[72] Bauby, C. E., and Kuo, A. D., "Active control of lateral balance in human walking," Journal of Biomechanics, 33, 1433-1440, 2000.

[73] www.tekscan.com/pdfs/FlexiforceUserManual.pdf

[74] www.hitecrcd.com/homepage/product-fs.htm

[75] M. Spong and M. Vidyasagar, "Robot Dynamics and Control," Wiley, New York, 1991.

[76] E.R.Westervelt, J.W.Grizzle and D.E. Koditschek, "Hybrid zero dynamics of planar biped walkers," IEEE Transactions on Automatic Control, vol. 48, no. 1, pp. 42- 56, Jan 2003.

[77] A. Isidori, "Nonlinear Control Systems," Springer-Verlag New York, USA, 1995.

[78] S. Kajita, T. Nagasaki, K. Kaneko, K. Yokoi and K. Tanie, "A hop towards running humanoid biped," IEEE International Conference on Robotics and Automation, vol. 1, pp. 629-635, 2004.

[79] J. Nagasaka, K. Kuroki, Y. Suzuki, S. Itoh and Y. Yamaguchi, "Integrated motion control for walking, jumping and running on a small bipedal entertainment robot," IEEE International Conference on Robotics and Automation, vol. 4, pp. 3189-3194, Apr 26-May 1, 2004.

[80] *http://world.honda.com/HDTV/ASIMO/.*

[81] K. Arikawa and T. Mita, "Desing of Multi-DOF Jumping Robot," IEEE International Conference on Robotics and Automation, pp. 3992 - 32997, 2002.

[82] S. Sakka and K. Yokoi, "Humanoid Vertical Jumping based on Force Feedback and Inertial Forces Optimization," IEEE International Conference on Robotics and Automation, pp. 3752 - 3757, 18-22 April 2005.

[83] V. Nunez and N. Nadjar-Gauthier, "Control strategy for vertical jump of humanoid robots," International Conference on Intelligent Robots and Systems, pp. 2253 - 2258, 2-6 Aug. 2005.

[84] T. Hirano, T. Sueyoshi and A. Kawamura, "Development of ROCOS (Robot Control Simulator)-Jump of human-type biped robot by the adaptive impedance control," Proceedings of 6th International Workshop on 30 Advanced Motion Control, pp. 606 - 611, April 2000.

[85] T. Mita, Sang-Ho Hyon and T.K. Nam, "Analytical time optimal control solution for a two-link planar aerobot with initial angular momentum," IEEE Transactions on Robotics and Automation, vol. 17, no. 3, pp. 361 - 366, June 2001.

[86] M. Sobotka and M. Buss, "Locomotion studies for a 5DoF gymnastic robot," Proceedings of International Conference on Intelligent Robots and Systems, pp. 3275- 3280, August 2005.

[87] Mehdi Nikkhah, Hashem Ashrafiuon and Farbod Fahimi, "Robust control of underactuated bipeds using sliding modes," Robotica, vol. 25, no. 3, pp. 367-374, May 2007.

[88] T.F. Coleman and Y. Li, "An Interior, Trust Region Approach for Nonlinear Minimization Subject to Bounds," SIAM Journal on Optimization, vol. 6, pp. 418-445, 1996.

[89] T.F. Coleman and Y. Li, "On the Convergence of Reflective Newton Methods for Large-Scale Nonlinear Minimization Subject to Bounds," Mathematical Programming, vol. 67, pp. 189-224, 1994.

[90] A. Meghdari and M. Aryanpour, "Dynamic Modeling and Analysis of the Human Jumping Process," Journal of Intelligent and Robotic Systems, vol. 37, pp. 97-115, 2003.

[91] Yildirim Hurmuzlu and Dan B. Marghitu, "Periodic Motions of a Hopping Robot With Vertical and Forward Motion," The International Journal of Robotics Research, vol. 13, no. 1, pp. 82-92, 1994.

[92] K. Mirza, M.D. Hanes and D.E. Orin, "Dynamic simulation of enveloping power grasps ," International Conference on Robotics and Automoation, vol. 2, pp. 430-435, 2-6 May 1993.

[93] M.S. Branicky, "Multiple Lyapunov functions and other analysis tools for switched and hybrid systems," IEEE Transactions on Automatic Control, vol. 43, no. 4, pp. 475-482 Apr 1998.

[94] B. Morris, J.W. Grizzle, "A Restricted Poincar Map for Determining Exponentially Stable Periodic Orbits in Systems with Impulse Effects: Application to Bipedal Robots," CDC-ECC, pp. 4199- 4206, Dec. 2005.

[95] Kwang Won Sok, Manmyung Kim, Jehee Lee, "Simulating biped behaviors from human motion data," International Conference on Computer Graphics and Interactive Techniques, no. 107, 2007.

[96] Marko B. Popovic, Ambarish Goswami, "Ground Reference Points in Legged Locomotion: Definitions, Biological Trajectories and Control Implications," Int. Journal of Robotics Research, vol. 24, no. 12, pp. 1013-1032, 2005.

[97] Arakawa, T. Fukuda, T.,"Natural motion generation of biped locomotion robot using hierarchical trajectory generation method consisting of GA, EP layers," ICRA, pp. 211-216, vol.1, 1997.

[98] Hassan K. Khalil, "Nonlinear systems," Portland, OR, 2001.

[99] Prahlad Vadakkepat, Dip Goswami and Chia Meng Hwee, "Disturbance Rejection by Online ZMP Compensation," Robotica, vol. 26, pp. 9-17, 2007.

[100] M. Berkemeier and R. Fearing, "Tracking fast inverted trajectories of the underactuated acrobot," IEEE Transansaction Robotics and Automatation, vol. 15, pp. 740-750, 1999.

[101] Goswami Dip, Vadakkepat Prahlad and Phung Duc Kien, "Genetic algorithm-based optimal bipedal walking gait synthesis considering tradeoff between stability margin and speed," Robotica (2008).